RECRYSTALLIZATION OF $Cu(In,Ga)Se_2$ THIN FILMS BY METAL HALIDE VAPOR TREATMENTS

by

Elizabeth C. Palmiotti

© Copyright by Elizabeth C. Palmiotti, 2021

All Rights Reserved

A thesis submitted to the Faculty and the Board of Trustees of the Colorado School of Mines in partial fulfillment of the requirements for the degree of Doctor of Philosophy (Materials Science).

Golden, Colorado

Date ______________________

Signed: ______________________

Elizabeth C. Palmiotti

Signed: ______________________

Dr. Angus A. Rockett
Thesis Advisor

Golden, Colorado

Date ______________________

Signed: ______________________

Dr. Eric Toberer
Director of Materials Science Program
Department of Metallurgical & Materials Engineering

ABSTRACT

$CuIn_{1-x}Ga_xSe_2$ (CIGS) thin film photovoltaic module performance and manufacturing have shown significant successes; however, cost has limited a large-scale commercial presence. Significant reductions in absorber deposition time and temperature are necessary to minimize expenses to compete as a single junction technology. Due to a tunable band gap, an alternative future for CIGS is using a wide band gap alloy, $CuGaSe_2$ (CGS) as a top cell in a tandem structure with silicon. However, wide gap CIGS materials produce devices which are typically of poor quality due to kinetically-limited growth which results in secondary phases, small grains, and inhomogeneities. In this thesis these problems are addressed through novel metal halide vapor treatments to recrystallize CIGS thin films.

In this work, metal halide compounds used for treatment are selected such that the cation is already a species in the $(Cu,Ag)(In,Ga)Se_2$ alloy system and the anion is a halide. Metal halide vapor treatments to CIGS films deposited at 350°C result in large grain growth and improved crystallinity. Composition variation occurs depending on the metal halide used, though, gallium depletion is common for all. It is also demonstrated that the metal halide treatments catalyze and accelerate the crystallization kinetics for CIGS using in-situ high-temperature x-ray diffraction (HT-XRD). An evaluation of metal halide thermodynamic properties is presented and compared to experimental results. Based on bond dissociation energies, CuBr, CuI, AgBr, and AgI are recommended as metal halide source materials with a preference to AgBr and AgI due to the known benefits of Ag alloying. It is proposed that growth occurs by vapor phase transport induced by a halide transport agent. The halide anion forms volatile compounds with metal cations on the surface of one grain, which etch and re-deposit onto the surface of a neighboring grain. This causes the observed grain growth and defect passivation. For such volatile compounds with very high vapor pressures, such as the Ga-halide compounds, re-deposition to a neighboring grain surface is too slow and results in the preferential etching of such metallic species.

The beneficial treatments are applied to CGS films to replace a long, high-temperature deposition procedure necessary to fabricate uniform films. Instead, the deposition is interrupted and AgBr evaporated during growth, reducing deposition time by ~50%. This results in large grains, phase homogeneity, and device efficiency improvements due to open-circuit voltage and fill factor.

TABLE OF CONTENTS

ABSTRACT . . . iii

LIST OF FIGURES . . . viii

LIST OF TABLES . . . x

LIST OF SYMBOLS . . . xi

LIST OF ABBREVIATIONS . . . xiii

ACKNOWLEDGMENTS . . . xv

DEDICATION . . . xvi

CHAPTER 1 MOTIVATION AND OUTLINE OF THESIS . . . 1

1.1 Global Context . . . 1

1.2 Photovoltaics Market and Outlook . . . 2

1.3 Thesis Statement . . . 3

1.4 Thesis Outline . . . 4

1.5 References . . . 4

CHAPTER 2 GENERAL BACKGROUND INFORMATION . . . 6

2.1 Photovoltaic Cells . . . 6

2.1.1 Current-Voltage . . . 7

2.1.2 External Quantum Efficiency . . . 9

2.2 Tandem Photovoltaics . . . 9

2.3 Recrystallization and Grain Growth . . . 10

2.3.1 Recrystallization . . . 10

2.3.2 Grain Growth . . . 11

2.4 References . . . 12

CHAPTER 3 BACKGROUND: THIN FILM CIGS . . . 14

3.1 CIGS Overview . . . 14

3.1.1 Structure . . . 14

3.1.2 Gallium Alloying . . . 14

3.1.3 Silver Alloying . . . 16

3.1.4 Kinetic Aspects of CIGS . . . 17

3.2 CIGS Vapor Deposition Techniques and Implications . . . 18

3.2.1 Co-Evaporation . . . 18

3.2.2 Recrystallization and Grain Growth of CIGS during Deposition . . . 19

3.3 Alkali Treatments . . . 21

3.4 Recrystallization and Grain Growth of CdTe . . . 21

3.5 References . . . 22

CHAPTER 4 A THERMODYNAMIC EVALUATION OF METAL HALIDES FOR THE RECRYSTALLIZATION OF $Cu(In,Ga)Se_2$ . . . 29

4.1 Introduction . . . 29

4.2 Experimental Examples . . . 31

4.2.1 Metal Halide Treatments . . . 31

4.2.2 Metal Halide Treatment Examples . . . 31

4.3 Thermodynamic Evaluation . . . 34

4.3.1 Bond Dissociation Energies . . . 34

4.3.2 Standard Enthalpies of Formation . . . 35

4.3.3 Vapor Pressure Evaluation . . . 35

4.3.4 Melting Points . . . 36

4.4 Discussion . . . 39

4.5 Conclusion . . . 40

4.6 Acknowledgements . . . 41

4.7 Appendix A . . . 41

4.8 References . . . 41

4.9 Thesis Author Contributions . . . 46

CHAPTER 5 IN-SITU STUDY OF THE CRYSTALLIZATION OF AMORPHOUS $CuInSe_2$ THIN FILMS AND THE EFFECT OF $InCl_3$ TREATMENT . . . 47

5.1 Abstract . . . 47

5.2 Introduction . . . 47

5.3 Experimental Details . . . 48

5.4 Results and Discussion . . . 49

5.4.1 Ex-Situ Annealing Investigation . . . 49

5.4.2 In-Situ Kinetic Investigation . . . 51

5.5 Conclusions . . . 57

5.6 Acknowledgements . . . 58

5.7 References . . . 58

5.8 Thesis Author Contributions . . . 60

CHAPTER 6 HOMOGENEOUS $CuGaSe_2$ GROWTH BY THE CUPRO PROCESS WITH IN-SITU AgBr TREATMENT . . . 61

6.1 Introduction . . . 61

6.2 Experimental Details . . . 62

6.2.1 Film and Device Fabrication . . . 62

6.2.2 Characterization . . . 63

6.3 Results . . . 63

6.3.1 Scanning Electron Microscopy . . . 63

6.3.2 TOF-SIMS . . . 64

6.3.3 X-Ray Diffraction . . . 66

6.3.4 Device Characterization . . . 67

6.4 Discussion . . . 69

6.5 Conclusion . . . 70

6.6 Funding . . . 70

6.7 References . . . 70

6.8 Appendix A . . . 73

6.9 Thesis Author Contributions . . . 73

CHAPTER 7 CONCLUSION . . . 74

7.1 Supporting Work . . . 74

7.2 Discussion and Conclusions . . . 74

7.3 Future Applications . . . 75

7.4 References . . . 75

APPENDIX A ADDITIONAL PUBLICATIONS . . . 77

A.1 Identification and analysis of partial shading breakdown sites in $CuIn_xGa_{(1-x)}Se_2$ modules . . . 77

A.2 Post-Deposition Recrystallization of Chloride Treated $Cu(In,Ga)Se_2$ Thin-Film Solar Cells . . . 77

A.3 Post-Deposition Recrystallization of Co-Evaporated $Cu(In,Ga)Se_2$ Films by Bromide Vapor Treatments . . . 78

A.4 $CuIn_{(1-x)}Ga_xSe_2$ Recrystallization by Metal Halide Treatments . . . 78

APPENDIX B RELEVANT CO-AUTHORED PUBLICATIONS . . . 80

B.1 Impact of Post-Deposition Recrystallization by Alkali Fluorides on $Cu(In,Ga)Se_2$ Thin-Film Materials and Solar Cells . . . 80

B.2 In Situ Recrystallization of Co-Evaporated $Cu(In,Ga)Se_2$ Thin Films by Copper Chloride Vapor Treatment towards Solar Cell Applications . . . 80

B.3 Recrystallization of $Cu(In,Ga)Se_2$ Semiconductor Thin Films via $InCl_3$ Treatment . . . 81

APPENDIX C COPYRIGHT PERMISSIONS . . . 82

C.1 IRENA 2020 Figure Copyright . . . 82

C.2 ISE Photovoltaics Report Figure Copyright . . . 82

C.3 Chapter 4 Permission . . . 83

C.4 Chapter 5 Permission . . . 83

LIST OF FIGURES

Figure 1.1 Accelerated projection of electricity generation per technology through 2050. PES and TES (IRENA), 2017 values based on IEA (2019b). Figure from IRENA Global Renewables Outlook: Energy transformation 2050 [1]. 1

Figure 1.2 Market share distribution of CdTe, a-Si, and CIGS thin film technologies. Data: from 2000 to 2009: Navigant; from 2010: IHS Markit. Graph: PSE Projects GmbH 202. Figure from Fraunhofer ISE, 2021 [2]. 3

Figure 2.1 A diagram of (a) a pn-junction where free electrons (-) and holes (+) diffuse from their respective sides resulting in a build-up of charge thus electric field (E) across the depletion region (w). A diagram of (b) the photovoltaic effect resulting from the energy of incident photons ($h\nu$) to the pn-junction with an external load; based on Figure 1.1 in [1]. 7

Figure 2.2 Linear-scale illuminated J-V curve and some device parameters extracted from the curve. A ratio of the areas made by the blue lines and red lines is used to determine the fill factor. 8

Figure 2.3 Sigmoidal curve representing the extent, or fraction, of recrystallization with respect to time (t). 11

Figure 3.1 Schematic of a (Cu,Ag)(In,Ga)$(Se,S)_2$ chalcopyrite unit cell where $a = b \neq c$. Drawn using VESTA [4]. 15

Figure 3.2 Melting point (°C) and band gap (eV) values for the ternary chalcogenide compounds of interest in the (Ag,Cu)(In,Ga)Se_2 alloy system. Figure adapted from [18]. 17

Figure 3.3 Qualitative schematics are shown for typical CIGS co-evaporation depositions based on CuPRO and 3-stage processes. Both are conducted under a constant Se overpressure which is not drawn. 20

Figure 3.4 Schematic showing the growth and the phases present during Stage 2 of a multi-stage CIGS deposition. Phases drawn represent ordered vacancy compounds (OVC) and stoichiometry (1:1:2). This figure is adapted and re-drawn from [39]. 20

Figure 4.1 Top-view and cross-section SEM images of the CIGS film deposited at 350°C and after treatments with $InBr_3$, CuBr, and $InCl_3$ at 450°C each. 32

Figure 4.2 XRD results plotted on a logarithmic scale for the CIGS film deposited at 350°C and after treatments with $InBr_3$, CuBr, and $InCl_3$ at 450°C each. The characteristic peaks have been magnified and plotted separately. 33

Figure 4.3 Bond dissociation energy (eV) values for metal halide compounds being considered. Blue triangles represent the bond dissociation energy for $MH_3 \rightarrow MH_2+H$, red circles for $MH_2 \rightarrow MH+H$, and black squares for $MH \rightarrow M+H$. 34

Figure 4.4 Extrapolated vapor pressure versus temperature for metal halides of interest in the temperature range of interest. Chloride compounds are plotted with solid lines, bromide compounds with dashed lines, and iodide compounds with dot-dashed lines. 37

Figure 4.5 Schematic of the proposed halide-induced recrystallization and grain growth process and mechanism. A metal halide (MH) is evaporated and introduced in the vapor phase. In CIGS grain boundaries the metal halide with CIGS species (M'H) which desorb, move between grains, and re-adsorb resulting in grain growth. A schematic of vapor phase atomic transport resulting in grain growth follows. 38

Figure 5.1 Top-view SEM micrographs of (a) CIS/Si and (b) CIS/SLG after a five minute anneal at 250°C and of (c) CIS/Si and (d) CIS/SLG after a five minute anneal at 400°C. 49

Figure 5.2 Top-view SEM micrographs of CIS/Si and CIS/SLG films after the $InCl_3$ solution treatments conducted at 350, 400, and 450°C. 51

Figure 5.3 In-situ HT-XRD patterns collected from 150 to 450°C of 1 µm thick CIS films on SLG and Si substrates with and without $InCl_3$ solution treatments. Unidentified peaks are parts of the identified phases. 52

Figure 5.4 (a) Peak intensity, or height, in counts for the (112) orientation of $CuInSe_2$ versus temperature for all samples. (b) Five-point moving average of full-width at half maximum (FWHM) for the (112) orientation of $CuInSe_2$ versus temperature. 54

Figure 5.5 Five-point average of peak height data for the (112) orientation of $CuInSe_2$ normalized from zero to one (scatter points). Fitted sigmoid curves are overlain in solid lines. 55

Figure 5.6 Crystallization rate versus temperature as determined by the first derivative of the fitted sigmoid curves of the five-point average of the normalized peak height data. 56

Figure 6.1 Cross-section and top-view SEM images of CGS films deposited by CuPRO, CuPRO(M), and CuPRO+AgBr processes. 63

Figure 6.2 Positive ion TOF-SIMS scans collected for the CuPRO, CuPRO(M), and CuPRO+AgBr samples. The Cu signal is plotted in yellow, the Ga in green, and Se in blue. 65

Figure 6.3 XRD spectra of the CGS films deposited by CuPRO, CuPRO(M), and CuPRO+AgBr treatment. Peaks representing characteristic (112), (220)/(204), and (312)/(116) orientations were plotted over smaller 2θ ranges for interpretation. 67

Figure 6.4 Device parameters for the five highest efficiency (%) devices per deposition procedure. The fill factor (FF) (%) and V_{oc} (mV) were extracted from current density-voltage measurements and J_{sc} (mA/cm^2) values extracted from external quantum efficiency measurements. 68

Figure 6.5 External quantum efficiency (EQE) curves for CGS devices prepared by CuPRO, CuPRO(M), and CuPRO+AgBr. 69

Figure 6.6 Schematics of the deposition recipes followed to deposit CGS films by CuPRO, CuPRO+AgBr, and CUPRO(M). Note that the evaporation fluxes are relative and times are approximate. The stages are respectively labeled as I, II, and III. The "relaxation" steps in CuPRO(M) are labeled as R. 73

LIST OF TABLES

Table 3.1 Summary of reaction kinetics determined by high-temperature x-ray diffraction (HT-XRD) for CIS, CGS, and CIGS. 17

Table 4.1 Composition results collected by EDS for the CIGS film deposited at 350°C and after treatments with $InBr_3$, CuBr, and $InCl_3$ at 450°C each. 32

Table 4.2 Standard enthalpies of formation in eV for possible stable M'H compounds formed during the metal halide treatment [32]. 35

Table 4.3 Summary of metal halide compounds of interest, reported equations representing the vapor pressure dependence on temperature (in K, except $SeCl_4$ is in °C) in their original units, the temperature ranges the experiments were conducted over, and the respective sources. 36

Table 4.4 Melting (MP) points in °C at atmospheric pressure for the metal halide compounds under consideration [32]. 37

Table 5.1 Compositions (at%) of CIS samples after all treatment conditions with and without $InCl_3$. . . 50

Table 5.2 Maximum temperature values for each fitted sigmoid curves. 57

Table 6.1 Extracted XRD pattern parameters for CuPRO, CuPRO(M), and CuPRO+AgBr. Intensity ratios were calculated for peaks representing characteristic CGS orientations. . . . 66

LIST OF SYMBOLS

Activation energy . . . . E_a

Applied bias . . . . V_{app}

Atomic jump frequency . . . . w_0

Average grain diameter . . . . d

Average particle size . . . . $\langle R \rangle$

Avrami exponent . . . . a

Band gap . . . . E_g

Boltzmann's constant . . . . k_B

Built-in potential . . . . V_{bi}

Charge . . . . q

Chemical interdiffusivity . . . . $\tilde{D}$

Concentration of acceptor atoms . . . . N_a

Concentration of donor atoms . . . . N_d

Dark saturation current . . . . J_o

Depletion region . . . . w

Diffusion-limited coarsening rate constant . . . . K_D

Distance of each atomic jump . . . . Γ

Driving force . . . . P

Efficiency . . . . η

Electric field . . . . E

Energy barrier to jump . . . . ΔG^*

Fill-factor . . . . FF

Fraction Recrystallized X

Free energy difference across grain boundary . . . . ΔG

Grain boundary mobility . . . . M_B

Grain boundary velocity v

Growth rate . . . . . $\dot{G}$

Ideality factor . . . . . n

Initial grain diameter . . . . . d_0

Input power . . . . . P_{in}

Light-generated current density . . . . . J_L

Maximum power . . . . . P_m

Mean atomic volume of the particle . . . . . Ω

Nucleation rate . . . . . $\dot{N}$

Open circuit voltage . . . . . V_{oc}

Pre-factor . . . . . A

Short-circuit current density . . . . . J_{sc}

Solubility . . . . . c^{eq}

Temperature . . . . . T

Time . . . . . t

Total current density . . . . . $J(V)$

Vapor pressure . . . . . p

Volume fraction . . . . . Q

Wavelength . . . . . λ

LIST OF ABBREVIATIONS

$(Ag,Cu)(In,Ga)Se_2$ . . . . . ACIGS

Abnormal Grain Growth . . . . . AGG

Cadmium chloride . . . . . $CdCl_2$

Cheical bath deposition . . . . . CBD

Cu-poor/Cu-rich/Cu-off . . . . . CuPRO

$CuGaSe_2$ . . . . . CGS

$CuIn_{1-x}Ga_xSe_2$, $Cu(In,Ga)Se_2$ . . . . . CIGS

$CuInSe_2$ . . . . . CIS

Energy dispersive spectroscopy . . . . . EDS

External Quantum Efficiency . . . . . EQE

Face-centered cubic . . . . . FCC

Full width at half maximum . . . . . FWHM

High-temperature x-ray diffraction . . . . . HT-XRD

Intermediate metal halide compound . . . . . M'H

International Center for Diffraction Data . . . . . ICDD

Johnson-Mehl-Avrami-Kolmogorov . . . . . JMAK

Lifshitz, Slyozof, and Wagner . . . . . LSW

Melting point . . . . . MP

Metal Halide . . . . . MH

Modified CuPRO . . . . . CuPRO(M)

Normal Grain Growth . . . . . NGG

Ordered defect pair . . . . . ODP

Ordered vacancy compounds . . . . . OVC

Photovoltaic . . . . . PV

Polyether ether ketone . . . . . PEEK

Post-deposition treatment . . . . PDT

Scanning electron microscopy . . . . SEM

Soda-Lime Glass . . . . SLG

Standard Test Conditions . . . . STC

Time-of-flight secondary ion mass spectrometry . . . . TOF-SIMS

Transparent conductive oxide . . . . TCO

Vapor-liquid-solid . . . . VLS

X-Ray Diffraction . . . . XRD

ACKNOWLEDGMENTS

I would first and foremost like to acknowledge my advisor, Dr. Angus Rockett, for all of his guidance and support through my graduate experience. I greatly value all you have done to share your expertise and to help me develop my skills as a globally minded researcher and aspiring professor. I am so thankful for the opportunities and encouragement you have provided me.

Merci à ma deuxième maison de recherche à l'Université de Nantes et l'équipe du Bâtiment de Physique: Dr. Nicolas Barreau, Dr. Xenia Tsoulka, Eugene Bertin, Arthur Chadaigne, Dr. Sylvie Harel, Dr. Ludovic Arzel, Dr. Thomas Lepetit, Luna Postma, et Fabien Pineau. Merci de m'avoir accueilli dans votre laboratoire et de partager avec moi votre enthousiasme pour la recherche et le CIGS. Je penserai toujours avec émotion à mon séjour à Nantes. Je suis reconnaissant d'avoir été accueilli dans vos vies et j'ai hâte de retourner en France!

I would like to acknowledge all of the amazing friends I have made during my years in Colorado. I thank you for the long study nights, exciting discussions about research, and encouraging those much needed trips to the mountains. Thank you for that extra espresso to fuel a pre-work tour. For letting me study in the car so we could make a few extra turns. For sitting through practice talks. For brain-clearing bike rides. For being there. Liz loves you.

Thank you to Dr. Sylvain Marsillac's team at Old Dominion University for your help in developing our understanding of this exciting research. I would also like to acknowledge the faculty and staff the Colorado School of Mines who shared their knowledge and experience to help me interpret and guide my experiments.

Thank you to my thesis committee, Dr. Brian Gorman, Dr. Corinne Packard, and Dr. Colin Wolden, for helping me progress and stay on track.

Last, but certainly not least, thank you to my sister and parents who were the original supporters of my pursuit to try any challenge set in front of me. You encouraged me to test my creative, physical, and educational limits which led to you dropping me off in the middle of cowboy-country. I thank you for the opportunities you have provided me and continued support.

This thesis is dedicated to my parents, Pete and Claire Palmiotti,

whose support has brought me to where I am today.

CHAPTER 1
MOTIVATION AND OUTLINE OF THESIS

This chapter provides the motivation and global context of the work presented in this thesis. This is followed by a thesis statement with proposed solutions to challenges outlined and the structure of the thesis document.

1.1 Global Context

Due to the growing social, economic, and environmental impacts of climate change, governments and organizations have been committing resources to reduce greenhouse gas production and achieve net zero carbon emissions. The majority of anthropogenic emissions result from energy generation by fossil fuels, which has resulted in a rapid increase of the global temperature. This climate crisis will continue to result in more frequent and extreme natural disasters and risk to human life, particularly to vulnerable populations whom climate change disproportionately affects. The most dangerous effects of climate change can be avoided if emissions are largely reduced by transitioning to an infrastructure based on renewable energy sources. Currently, the transition towards a majority renewable energy sector falls short of the requirements to meet decarbonization goals necessary to prevent global temperatures exceeding a 1.5°C increase. In order to meet this goal, approximately two-thirds of energy generation must be from renewable sources by 2050. Figure 1.1 shows a breakdown of the accelerated electricity generation transition needed to combat climate change. Wind and solar PV (photovoltaic) technologies dominate the transition towards renewables and must both be optimized to combat the energy crisis [1]. Photovoltaic technologies are the focus of this dissertation.

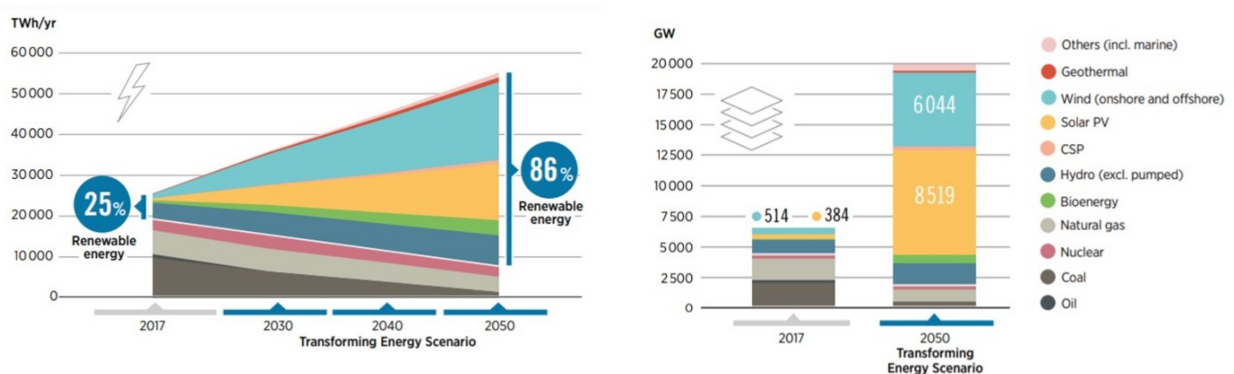

Figure 1.1 Accelerated projection of electricity generation per technology through 2050. PES and TES (IRENA), 2017 values based on IEA (2019b). Figure from IRENA Global Renewables Outlook: Energy transformation 2050 [1].

1.2 Photovoltaics Market and Outlook

Rooftop and utility-scale photovoltaic module installations continue to grow and dominate as new electricity generation sources, largely driven by rapidly decreasing costs. In 2020, 93 GW_{AC} of PV were deployed among the eight leading countries contributing to the nearly 723 GW_{AC} cumulative global installations [2]. However, it is expected that over 8,000 GW will be necessary for PV to account for ~25% of the electricity production by 2050 [1]. For this to become a reality, PV modules must be fabricated at lower costs and their efficiencies further improved.

Silicon modules are currently the best performing terrestrial single-junction technology under one-sun, non-concentrating conditions and dominate the market at approximately 95% [2]. The success of silicon is largely attributed to technological maturity due to its history in the microelectronics industry. Additionally it has a high abundance as a natural resource and a relatively simple growth procedure for electronic grade material. Though commercially successful, silicon is not an ideal material for photovoltaic applications due to its indirect band gap, thus thick absorber layer requirements. Moreover, single-junction silicon devices are rapidly nearing their maximum theoretical efficiency, motivating research in other technologies [3], [4]. Thin film photovoltaics are alternative PV absorber materials with direct band gaps, exceptionally high absorption coefficients, and are used to produce high efficiency devices and modules. Figure 1.2 shows the annual market share distribution of thin film CdTe, a-Si, and $CuIn_{1-x}Ga_xSe_2$ (CIGS) modules [2]. CdTe technologies dominate the thin film market due to low capital costs resulting from a high-throughput deposition procedure. Typically, polycrystalline CdTe is deposited at a high-rate and low temperature, producing films with a large amount of defects, poor crystallinity, and small grains. A solution or vapor $CdCl_2$ treatment is the standard to improve grain size, recrystallize, passivate defects, and improve device performance [5], [6], [7]. CIGS solar cell performance and module manufacturing have shown significant successes, however, the cost per module is currently not sufficiently competitive to warrant large scale manufacturing as shown in Figure 1.2. This is largely attributed to the slow, high-temperature deposition procedure necessary for high efficiencies resulting in high capital expenditures [8]. In spite of this, CIGS is still of interest because it has a higher efficiency than CdTe and greater tunability through alloy, thus band gap, engineering.

The relatively low cost of silicon module fabrication has made the single junction market difficult for thin film technology penetration. However, if the manufacturing process for a high-efficiency thin film should be modified to be cost-competitive this could change. There is interest in developing tandem cell technology for large-scale deployment with silicon as the bottom cell and a wide band gap thin film as the top cell. This could increase efficiencies of terrestrial photovoltaics with a nominal increase to cost.

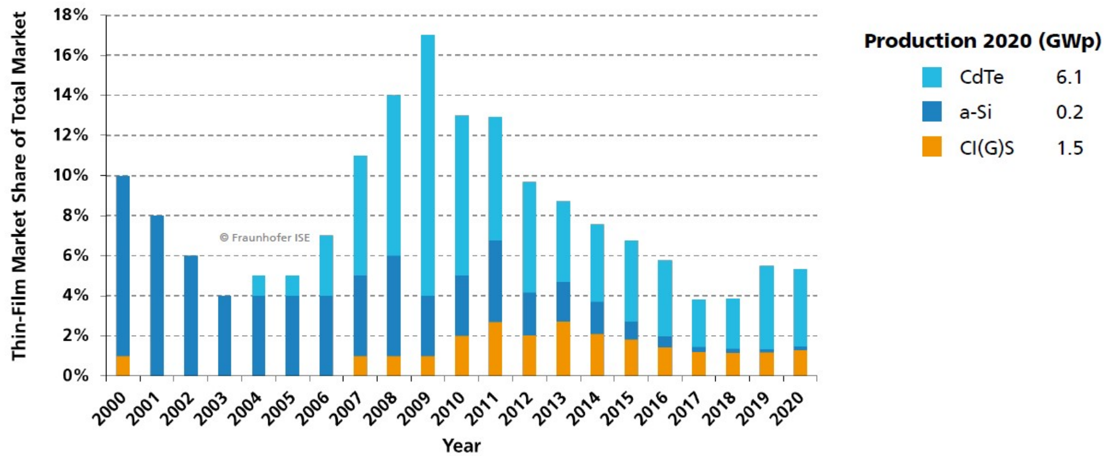

Figure 1.2 Market share distribution of CdTe, a-Si, and CIGS thin film technologies. Data: from 2000 to 2009: Navigant; from 2010: IHS Markit. Graph: PSE Projects GmbH 202. Figure from Fraunhofer ISE, 2021 [2].

However, wide band gap semiconductors usually have high defect densities, small grains, and make poor performing devices.

1.3 Thesis Statement

CIGS is used to produce high-efficiency thin film photovoltaic modules, however, an expensive deposition process has limited its profitability, thus commercial presence. In order for CIGS to be an economical option, fabrication time and temperature should be reduced while maintaining good material properties. For application as a wide band gap material for silicon tandem structures, improvements to the uniform deposition of high-Ga or pure-Ga CIGS are necessary. This thesis demonstrates some solutions with respect to the future of CIGS technologies:

1. Increasing manufacturing throughput to reduce capital expenses through novel metal halide induced recrystallization treatments

2. Developing an understanding and mechanism of such metal halide treatments to better optimize their selection and use by evaluating their thermodynamic properties

3. Investigating metal halide impacts on the reaction kinetics of CIGS crystallization

4. Applying metal halide treatments to fabricate improved wide band gap material for future integration into tandem devices

1.4 Thesis Outline

The remainder of this thesis is outlined as follows:

Chapter 2 provides general background information pertaining to photovoltaic cells, tandem cells, recrystallization, and grain growth.

Chapter 3 is a review of some material properties of CIGS and its alloys and deposition by co-evaporation. This is followed by summaries of CIGS recrystallization by growth then CIGS alkali halide post deposition treatments. Details about the recrystallization of CdTe films with $CdCl_2$ are provided, which the metal halide treatments of CIGS emulate.

Chapter 4 is the submitted manuscript *A Thermodynamic Evaluation of Metal Halides for the Recrystallization of Cu(In,Ga)Se_2*. This article is a review of metal halide properties with respect to a proposed mechanism for Cu(In,Ga)Se_2 recrystallization by metal halide treatments.

Chapter 5 is the submitted manuscript *In-Situ Study of the Crystallization of Amorphous $CuInSe_2$ Thin Films and the Effect of $InCl_3$ Treatment*. This work demonstrates how $InCl_3$ catalyzes Cu(In,Ga)Se_2 kinetics of crystallization and is necessary for grain growth.

Chapter 6 is the manuscript prepared for submission *Homogeneous $CuGaSe_2$ Growth by the CuPRO Process with In-Situ AgBr Treatment*. An in-situ AgBr treatment is used to decrease the time needed to form homogeneous $CuGaSe_2$ films by $\sim$50%. Grain size and device performance are also improved with this treatment.

Chapter 7 is a conclusion chapter to summarize the work presented and offers suggestions for further relevant work.

Appendix A is a compilation of additional first-author publications related to the work presented in this thesis.

Appendix B is a compilation of co-authored publications related to the work presented in this thesis.

Appendix C includes copyright related permissions for the content included in this thesis.

1.5 References

[1] (2020). Global Renewables Outlook: Energy transformation 2050, International Renewable Energy Agency [Web]. Available: www.irena.org/publications.

[2] S. Philipps and W. Warmuth, "Photovoltaics Report 2021. Fraunhofer Institute for Solar Energy Systems", Fraunhofer ISE [Report]. 2021.

[3] W. Shockley and H. Queisser, "Detailed Balance Limit of Efficiency of p-n Junction Solar Cells", Journal of Applied Physics, 32, 510, 1961. DOI: 10.1063/1.1736034.

[4] S. Bhattacharya and S. John, “Beyond 30% Conversion Efficiency in Silicon Solar Cells: A Numerical Demonstration”, Scientific Reports, 9, 1, 1-15, 2019. DOI: 10.1038/s41598-019-48981-w.

[5] B.E. McCandless and R.W. Birkmire, “Analysis of post deposition processing for CdTe/CdS thin film solar cells”, Solar Cells, 31, 527-535, 1991. DOI: 10.1016/0379-6787(91)90095-7.

[6] B. McCandless, I. Youm, and R. Birkmire, “Optimization of vapor post-deposition processing for evaporated CdS/CdTe solar cells”, Progress in Photovoltaics: Research and Applications, 7, 21-30, 1999. DOI: 10.1002/(SICI)1099-159X(199901/02)7:1<21::AID-PIP244>3.0.CO;2-D.

[7] T. Zhou, N. Reiter, R. Powell, R. Sasala, and P. Meyers, “Vapor chloride treatment of polycrystalline CdTe/CdS films”, Conference Record of the IEEE Photovoltaic Specialists Conference, 1994. DOI: 10.1109/wcpec.1994.519818.

[8] K. Horowitz, R. Fu, and M. Woodhouse, “An analysis of glass-glass CIGS manufacturing costs”, Solar Energy Materials and Solar Cells, 154, 1-10, 2016. DOI: 10.1016/j.solmat.2016.04.029.

CHAPTER 2

GENERAL BACKGROUND INFORMATION

This chapter provides background information for general topics discussed in this thesis. This includes the physics of photovoltaic cells, tandem photovoltaics, recrystallization, and grain growth.

2.1 Photovoltaic Cells

A photovoltaic cell is based on a pn-junction or Schottky diode (Figure 2.1(a)), which is formed by two semiconductor materials or a semiconductor and a metal, respectively. An n-type semiconductor is a material with excess electrons released into the conduction band from defect states referred to as donors. These states are due to impurities or point defects. The concentration of donor states is N_d. Electrons are the majority carriers and holes are the minority carriers in n-type materials. A p-type semiconductor has holes as majority carriers and electrons as minority carriers. Holes are produced by acceptor defects that, when ionized, accept an electron from the valence band, resulting in a mobile positively-charged hole. The concentration of acceptor states is N_a. When n-type and p-type materials are joined together, the respective majority carriers near this junction diffuse to the opposite side, resulting in a build-up of electrons on the p-type side and holes on the n-type side. This results in a region at the junction called the depletion region of width w from which the majority mobile carriers have been removed by this diffusion process. Majority carrier diffusion results in an electrostatic potential difference, or built-in potential (V_{bi}), which is equal to the amount of band bending across the depletion region and prevents further carrier diffusion. This build-up of charge results in a built-in electric field (E) from the n-type to p-type side. Minority carriers drift with the electric field. The opposing diffusion and drift of carriers eventually reaches a state of equilibrium such that there is no current flow across the junction at equilibrium [1], [2].

Upon applying an external forward bias to the diode (positive to p-type and negative to n-type), the potential barrier decreases and the diffusion current increases. In addition, the depletion width and junction resistance decrease. The drift current is unchanged in forward bias. The total current density ($J(V)$) is the sum of the diffusion and drift currents and can be determined by Equation 2.1 where J_o is the dark saturation current, q is charge, V_{app} is the applied bias, k_B is Boltzmann's constant, and T is temperature. This relationship is referred to as the diode equation [2].

$$J(V) = J_o \left(e^{\frac{qV_{app}}{k_B T}} - 1 \right) \tag{2.1}$$

The working mechanism of a photovoltaic cell is a pn-junction with an external load attached (Figure 2.1(b)). Incident photons from solar irradiation have sufficient energy to generate minority carriers

on one or both sides of the junction. These carriers drift across the depletion region resulting in a light-generated current density (J_L). If the load resistance is low, this results in a short-circuit current density (J_{sc}) with no voltage generated. If the load resistance is high the drift of the photogenerated carriers decreases the V_{bi} and allows forward current to flow in the diode. When the forward diffusion current equals the drift current of the photocarriers, they cancel out and no external current flows. The resulting voltage across the junction is the open circuit voltage (V_{oc}) of the device. The voltage-dependent current is the sum of the photocurrent, where $J_L = J_{sc}$, and the forward current in the pn-junction. The diode equation is thus modified by the photocurrent: Equation 2.2 [1].

$$J = J_o \left(e^{\frac{qV_{app}}{nk_BT}} - 1 \right) - J_{sc} \tag{2.2}$$

Equation 2.2 accounts for the possibility of recombination of photogenerated carriers as well as carriers diffusing through the depletion region. An ideality factor, n, is included to represent deviations from an ideal diode that result from recombination in the depletion region. For an ideal diode $n = 1$. If all recombination events occur in the depletion region then $n = 2$ and represents the worst case for a diode junction [3].

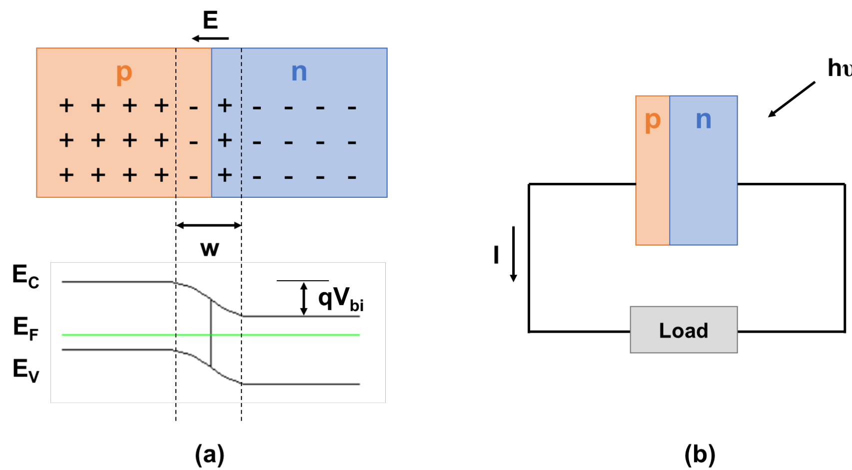

Figure 2.1 A diagram of (a) a pn-junction where free electrons (-) and holes (+) diffuse from their respective sides resulting in a build-up of charge thus electric field (E) across the depletion region (w). A diagram of (b) the photovoltaic effect resulting from the energy of incident photons ($h\nu$) to the pn-junction with an external load; based on Figure 1.1 in [1].

2.1.1 Current-Voltage

Many cell parameters can be determined by collecting illuminated current density-voltage (J-V) data. The Standard Test Conditions (STC) for collecting illuminated J-V curves are AM1.5 simulated solar spectrum light at an irradiance of $P = 100\frac{mW}{cm^2}$ and a temperature of 25°C. The typical shape and critical

parameters of an illuminated J-V curve is shown in Figure 2.2.

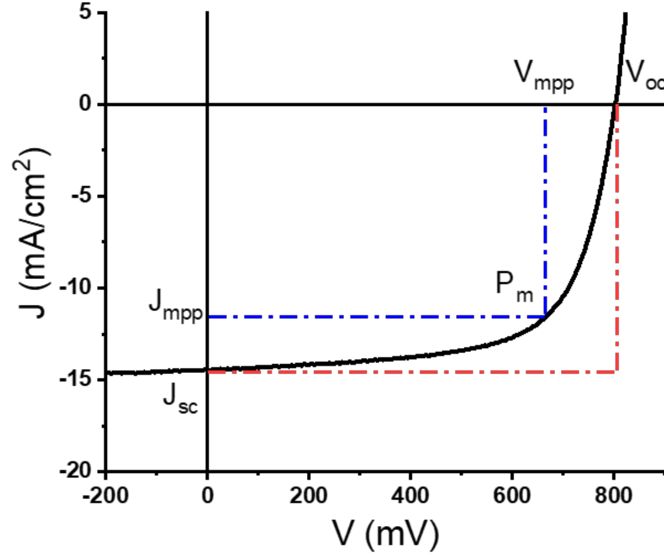

Figure 2.2 Linear-scale illuminated J-V curve and some device parameters extracted from the curve. A ratio of the areas made by the blue lines and red lines is used to determine the fill factor.

Illuminated J-V curves reveal how well the cell absorbs light to generate power by varying the load resistance. The open-circuit voltage (V_{oc}) is the maximum voltage and is identified by the x-intercept of the curve where current density is zero. J_{sc} is the maximum current and is found at the y-intercept where voltage is zero. A "good" solar cell should have high V_{oc} and J_{sc} parameters. V_{oc} is maximized by minimizing J_o (recombination). J_{sc} is maximized by maximizing photon collection efficiency and having good absorption [4].

$$V_{oc} = \frac{kT}{q} ln\left(\frac{J_{sc}}{J_o} + 1\right) \tag{2.3}$$

A cell generates power inside the voltage range zero to V_{oc} and is equal to the product of current and voltage. Maximum power (P_m) is produced where the product is maximized: (V_{mpp},J_{mpp}) [1]. This product appears as the area of an inscribed rectangle as highlighted by the blue lines in Figure 2.2. This area compared to the area made by the V_{oc} and J_{sc} (red region) is used to determine fill factor (FF) and is calculated using Equation 2.4. FF represents the "squareness" of the J-V plot and should be maximized to optimize a solar cell. The greatest value FF can have is unity. As seen in Equation 2.4, FF is maximized by maximizing photon absorption and minimizing recombination which both effect power generation [4].

$$FF = \frac{J_{mpp}V_{mpp}}{J_{sc}V_{oc}} \tag{2.4}$$

Efficiency (η) of photovoltaic energy conversion is determined by comparing the power input from incident photons to the power output of a cell using Equation 2.5. Input power (P_{in}) is $100\frac{mW}{cm^2}$ as per the previously stated STC [3].

$$\eta = \frac{P_m}{P_{in}} = \frac{V_{oc}J_{sc}FF}{P_{in}} \tag{2.5}$$

2.1.2 External Quantum Efficiency

External quantum efficiency (EQE) is another electrical characterization tool used to diagnose photovoltaic devices. At a constant voltage the device is illuminated using AM1.5 solar simulated light. The light is chopped to induce a change in light intensity, thus change in current. The change in current is measured at each change in intensity, or wavelength. In other words, the collected charge carriers per incident photon is measured. Each wavelength in a measurement corresponds to a different effective depth in the device resulting from the optical absorption coefficients of each layer. Optical losses that reduce the total EQE include inactive regions (grid shading) and reflection (with and without an anti-reflective coating). Shorter wavelengths show the collection efficiency of the buffer layer. At longer wavelengths the collection efficiency through the depth of the absorber is shown. Losses in this region are attributed to poor collection due to recombination.

By integrating the product of the EQE and the total number of photons at the corresponding wavelengths the total current, J_{sc} can be determined. It is useful to compare this J_{sc} value to the one determined by a J-V curve to confirm the calibration of the light used for the J-V curve. Furthermore, by collecting QE data at different voltages one can isolate collection differences through the depth of the device. The band gap, E_g, can also be extracted from an EQE plot for the absorber layer material. This is determined by extrapolating the downward slope in the long wavelength region, identifying the wavelength this intercepts, and inverting it such that $E[eV] = \frac{1240}{\lambda[nm]}$.

2.2 Tandem Photovoltaics

For single junction photovoltaics there exists a theoretical maximum efficiency [5] which is limited by the band gap of the absorber used. The most successful single junction absorber, Si, is rapidly approaching its theoretical maximum efficiency. Shockley and Queisser originally determined this value to be 30% for a 1.1 eV band gap (Si) where only radiative recombination is considered [6]. A more detailed calculation proposes a theoretical maximum efficiency of 29.43% for Si [7]. If a single junction thin film technology with a wider band gap closer to the ideal value for AM1.5 light (1.4-1.5 eV) were to be industrially competitive, it would face similar, though slightly higher, limits. Tandem photovoltaics offer a path to increase the theoretical efficiency limit to approximately 47% by allowing better absorption of the incident

spectrum's energy [5].

Tandems are constructed by stacking devices with different band gaps connected in series electrically. The top cell of the stack must have a wide band gap to allow shorter wavelength photons to pass through for absorption by the bottom, narrow-gap cell. This tandem device structure results in more energy being absorbed in the short wavelength region by the top cell, thus increasing efficiency. For the purpose of this dissertation, a Si (1.1 eV) bottom cell is considered. A Si tandem device is maximized to a theoretical efficiency of 42.4% with a top cell of E_g=1.72 eV [8]. Thin-film materials are of interest as the top cell due to appropriate band gap values and defect tolerance to compensate for non-ideal lattice matching.

2.3 Recrystallization and Grain Growth

This thesis focuses on inducing the recrystallization and grain growth of CIGS thin films by metal halide treatment. Initial thin film nucleation and growth during deposition is beyond the scope of this work, however, it will be noted that initial grain size and defect density are highly dependent upon the growth process (substrate temperature, elemental fluxes, composition, etc.). Recrystallization and grain growth are often necessary to passivate these defects and increase grain size such that columnar or equiaxed structures form which are desirable for high-efficiency photovoltaic absorbers. Generally, recrystallization is the nucleation and growth of a new, defect-free lattice followed by grain growth to reduce the total internal energy of the system.

2.3.1 Recrystallization

Recrystallization is the thermally activated formation then growth of new, defect-free grains at the expense of defective grains to reduce internal energy by decreasing defect density [9]. The fraction of material recrystallized, X, usually follows a sigmoidal relationship with time as drawn in Figure 2.3.

The progress of recrystallization versus time shown in Figure 2.3 is described by Johnson-Mehl-Avrami-Kolmogorov (JMAK), or Avrami, kinetics [10], [11], [12]. Below $t = t_0$ is called the incubation period where nucleation occurs at rate $\dot{N}$. Above t_0 growth occurs linearly at rate $\dot{G}$. At longer times, X approaches 1 as the driving force for further transformation is low enough that recrystallization is no longer favorable. Given a spherical grain assumption, Equation 2.6 can be used to model this recrystallization. The Avrami exponent, a, depends upon the dimensionality of growth. For $a \sim 0.5$ nucleation is instantaneous. As a increases towards 1.5, $\dot{N}$ becomes more constant. Note that this model relies on many assumptions (random nucleation, spherical grains, etc.) and is only valid for general recrystallization behaviors.

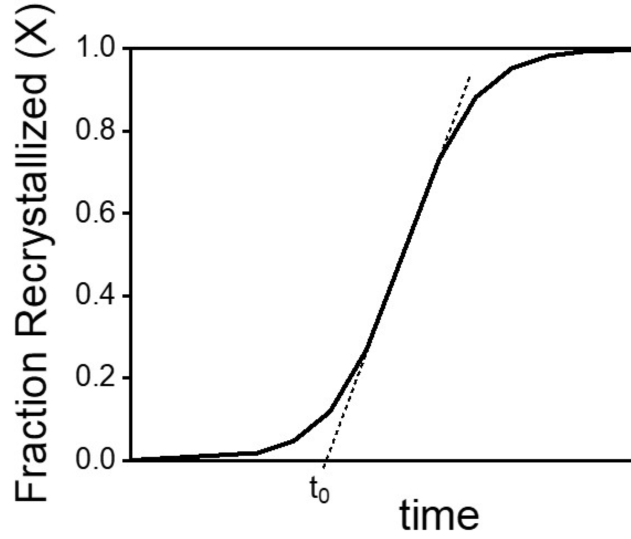

Figure 2.3 Sigmoidal curve representing the extent, or fraction, of recrystallization with respect to time (t).

$$X = 1 - exp\left(\frac{-\dot{N}\dot{G}^3\pi t^a}{3}\right) \tag{2.6}$$

2.3.2 Grain Growth

Once the initially small and defective grains have formed then recrystallized to replace regions of high defect density, grain growth may follow. Grain growth is driven by the reduction of surface energy, thus grain boundary area. This results in microstructure evolution where large grains grow at the expense of small grains. Normal grain growth (NGG) assumes continuous growth of all grains at a constant rate. It is represented by parabolic growth in Equation 2.7 where d is the average grain diameter, d_0 is the initial grain diameter, k is a kinetic coefficient, and t is time.

$$d^2 - d_0^2 = kt \tag{2.7}$$

Typically, abnormal grain growth (AGG) occurs in thin films. Anisotropy drives the growth of only some grains which will minimize surface and interface energies. In AGG grains grow discontinuously resulting in a bimodal distribution of grain sizes. The large grains impinge and consume the remaining small grains until a more uniform grain size distribution remains. This discontinuous AGG typically results in a thicker film [13].

Grain growth can be described in terms of grain boundary motion, which is related to the rate at which atoms move across the grain boundary. The velocity of this grain boundary motion can be generally defined by Equation 2.8 where v is the grain boundary velocity, M_B is grain boundary mobility, P is the

driving force, Γ is the distance of each atomic motion (jump), w_0 is atomic jump frequency, ΔG^* is the energy barrier for jumping, k_B is the Boltzmann's constant, T is temperature, and ΔG is the difference in free energy across the grain boundary [14], [15]. ΔG is the driving force of grain boundary motion and can be caused by curvature, defects, etc. By this equation, grain boundary motion may occur if the final state is energetically favorable and there is sufficient energy to overcome ΔG^*. M_B scales with self-diffusivity which can limit grain growth rates [16].

$$v = M_B P = \Gamma w_0 e^{-\frac{\Delta G^*}{k_B T}} \left(1 - e^{-\frac{\Delta G}{k_B T}}\right) \tag{2.8}$$

2.4 References

[1] J. Nelson, The Physics of Solar Cells, World Scientific Publishing Company, [Print], 2003.

[2] A. Rockett, The Materials Science of Semiconductors, Springer U.S., 2008.

[3] C.B. Honsberg and S.G. Bowden. (2019). Photovoltaics Education Website, [Web]. Available: https://www.pveducation.org/

[4] A. Luque and S. Hegedus, Handbook of Photovoltaic Science and Engineering, John Wiley & Sons, [Print], 2003.

[5] C. Henry, "Limiting efficiencies of ideal single and multiple energy gap terrestrial solar cells", Journal of Applied Physics, 51, 4494, 1980. DOI: 10.1063/1.328272.

[6] W. Shockley and H. Queisser, "Detailed Balance Limit of Efficiency of p-n Junction Solar Cells", Journal of Applied Physics, 32, 510, 1961. DOI: 10.1063/1.1736034.

[7] A. Richter, M. Hermle, and S. W. Glunz, "Reassessment of the Limiting Efficiency for Crystalline Silicon Solar Cells", IEEE Journal of Photovoltaics, 3, 4, 1184-1191, 2013. DOI: 10.1109/JPHOTOV.2013.2270351.

[8] M. Yamaguchi, K. Lee, K. Araki, and N. Kojima, "A review of recent progress in heterogeneous silicon tandem solar cells", Journal of Physics D: Applied Physics, 51, 13, 2018. DOI: 10.1088/1361-6463/aaaf08.

[9] P. Rios, F. Siciliano, H. Sandim, R. Plaut, and A. Padilha, "Nucleation and Growth During Recrystallization", Materials Research, 8, 3, 225-238, 2005.

[10] M. Avrami, "Kinetics of Phase Change. I General Theory", J. Chem. Phys., 7, 1103-1112, 1939. DOI: 10.1063/1.1750380.

[11] M. Avrami, "Kinetics of Phase Change. II Transformation-Time Relations for Random Distribution of Nuclei", J. Chem. Phys., 8, 212, 1940. DOI: 10.1063/1.1750631.

[12] M. Avrami, "Granulation, Phase Change, and Microstructure Kinetics of Phase Change", J. Chem. Phys., 9, 177, 1941. DOI: 10.1063/1.1750872.

[13] C. Thompson, “Grain Growth in Polycrystalline Thin Films of Semiconductors”, Interface Science, 6, 85-93, 1998. DOI: 10.1023/a:1008616620663.

[14] R. Balluffi, S. Allen, and W. Carter, Kinetics of Materials, Wiley, [Print], 2005.

[15] J. Hu, X. Wang, J. Zhang, J. Luo, Z. Zhang, and Z. Shen, “A general mechanism of grain growth -I. Theory”, Journal of Materiomics, 7, 1007-1013, 2021. DOI: 10.1016/j.jmat.2021.02.007.

[16] C. Thompson and R. Carel, “Texture development in polycrystalline thin films”, Materials Science and Engineering B, 32, 95, 211-219, 1995.

CHAPTER 3

BACKGROUND: THIN FILM CIGS

This chapter provides background information about the material properties, deposition processes, and post-deposition treatments of thin film CIGS used for photovoltaic applications. The $CdCl_2$ treatment of CdTe is also summarized.

3.1 CIGS Overview

CIGS has a high absorption coefficient of $\sim 10^5 cm^{-1}$ and a direct band gap [1] resulting in small thickness requirements. This makes it an excellent candidate for photovoltaic applications. Additionally, by varying the alloy composition, the band gap may be tuned to match the solar spectrum and optimize photon absorption. Some of its materials properties are discussed below.

3.1.1 Structure

Under typical vacuum-based growth conditions, CIGS is stable in the α-$CuInSe_2$ phase [2]. CIGS, a chalcogenide, and its alloys are stable in the chalcopyrite structure which belongs to the tetragonal crystal system and has a space group of $\mathrm{I}\bar{4}2\mathrm{d}$. The structure is drawn in Figure 3.1 with typical alloy elements where $a = b \neq c$. Chalcopyrite structures (ABC_2) are the ternary analog to the binary zinc-blende structure (AB). For zinc-blende structures, A atoms are tetrahedrally coordinated to B atoms in face-centered cubic (FCC) sites. Chalcopyrite structures are made by stacking zinc-blende unit cells and alternating the A and B atoms occupying FCC sites such that each C anion is tetrahedrally coordinated with two A and two B cations as shown in Figure 3.1. Changes to the structure in the z-direction are caused by electronegativity differences between the anion and the different cations causing differences in charge density along the bonds, thus different A-C and B-C bond lengths. This is referred to as tetragonal distortion [3]. Chalcopyrite structures typically have a c/a ratio of $\sim$2. Through alloying, the lattice constant and c/a ratio vary. Atom A is typically a Group I element, atom B from Group III, and atom C from Group VI: $A^I B^{III} C_2^{VI}$. The full alloy system commonly applied in photovoltaic applications is $(Ag,Cu)(In,Ga)(Se,S)_2$.

3.1.2 Gallium Alloying

$CuIn_{1-x}Ga_xSe_2$ is the most widely studied alloy system. The B sites in Figure 3.1 are randomly occupied by either In or Ga based on the composition. This is usually described using the metric GGI (Equation 3.1) which compares Ga content to the total Group III content. GGI represents the molar

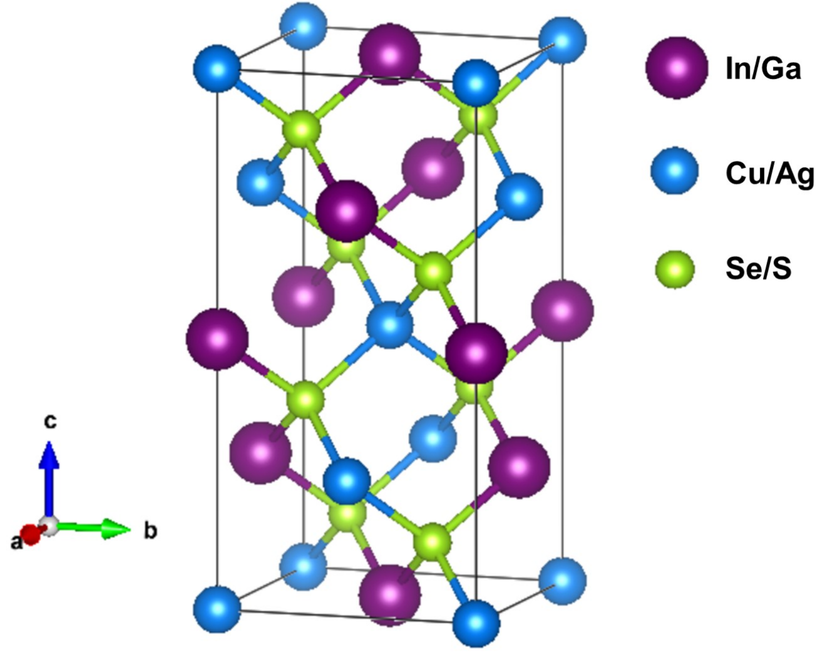

Figure 3.1 Schematic of a (Cu,Ag)(In,Ga)(Se,S)$_2$ chalcopyrite unit cell where $a = b \neq c$. Drawn using VESTA [4].

fraction x in $CuIn_{1-x}Ga_xSe_2$ and ranges from 0 ($CuInSe_2$) to 1 ($CuGaSe_2$). Some CIGS alloys are thought to have a miscibility gap at a maximum temperature of 127°C, which is well below typical deposition temperatures (500-600°C), though phase separation is not observed due to slow kinetics [5]. As x increases and more, smaller Ga atoms replace the larger In atoms, the lattice constant decreases. The c/a ratio decreases with greater GGI values due to the change in relative bond lengths.

$$GGI = \frac{Ga}{Ga + In} \tag{3.1}$$

Band gap (E_g) follows a parabolic trend with x. With increasing Ga-content the band gap widens from 1.03 eV for $CuInSe_2$ to 1.70 eV for $CuGaSe_2$. This relationship is shown in Equation 3.2 where x is the GGI, b is a bowing coefficient (~0.2 eV) [6], [7], [8], [9], $E_g(CIS)$ is the band gap of $CuInSe_2$, and $E_g(CGS)$ is the band gap of $CuGaSe_2$.

$$E_g(x)[eV] = (1 - x)E_g(CIS) + xE_g(CGS) - bx(1 - x) \tag{3.2}$$

This band gap variation across the alloy range is mainly due to a change in the conduction band minimum [9]. With increasing GGI the V_{oc} increases due to the widening band gap and the J_{sc} decreases due to a decrease in the total photons above the energy gap. Theoretically the conversion efficiency is maximized for GGI~0.7. Experimental results have shown that it is maximized for GGI~0.3 (E_g=1.15 eV)

[10]. Efficiency losses with increasing band gap are attributed to V_{oc} losses which increase recombination through deep-trap center defects [5].

$$CGI = \frac{Cu}{Ga + In} \tag{3.3}$$

Cu-content also has an effect on the band gap. Cu-content (molar fraction) is described with respect to the Group III metal content and is referred to as CGI (Equation 3.3). As Cu-content decreases the valence band maximum shifts down due to its strong dependence on defect composition (see Section 3.2.2). A more comprehensive band gap equation for CIGS was proposed by Stokes et al. to include this Cu-dependence (Equation 3.4) [11].

$$E_g^{total}(x)[eV] = (1-x)E_g(CIS) + xE_g(CGS) - bx(1-x) + 0.017(25 - X_{Cu}) \tag{3.4}$$

3.1.3 Silver Alloying

Recently, there has been increased interest in alloying CIGS with Ag. This system is often referred to as (Ag,Cu)(In,Ga)Se_2 or ACIGS. The introduction of Ag widens the band gap of the material by shifting the valence band maximum [12]. Ag alloying is thought to reduce the melting point of the compound by ~200°C [13] as shown in Figure 3.2. Note that the area formed by the four ternary compounds is the region of possible alloys and expected E_g and melting point (MP) values. It is commonly believed that reduced MP should improve mobility during deposition, thus enhancing structural order and crystallinity [14]. Additionally, large grain size enhancement results when even a small amount of Ag alloying is implemented compared to pure CIGS grown by the same process [15]. In fact, ACIGS deposited at 350°C (compared to standard 550°C) shows large grains and good crystalline quality [16]. Another benefit is the decrease in V_{oc} deficit for ACIGS compared to CIGS [17].

Although ACIGS is a promising alloy to improve device performance, widen the band gap, and reduce deposition temperature, its miscibility is still under debate. Furthermore the energy gap range accessible with low Ga alloys is not much greater than without Ag and desired wide gaps cannot be achieved with comparable results. Phase separation was seen for some compositions of polycrystalline ACIGS bulk ingots [19], however, complete miscibility was observed for ACIGS thin films [20] of varying Ag compositions [18] grown at typical high temperatures. ACIGS films grown at low temperature (350°C) showed Ag-content dependent inhomogeneities possibly due to limited Ag and Cu intermixing at this temperature [16]. Complete miscibility was calculated to occur at and above 482°C across the ACIGS alloy system. Decomposition is predicted at typical device operation temperatures (50°C) and typical post-deposition treatment temperatures (350°C) as determined by computational methods. This was confirmed experimentally where after a 25 hour anneal at 350°C Ag precipitates were found at Ga-rich regions [21].

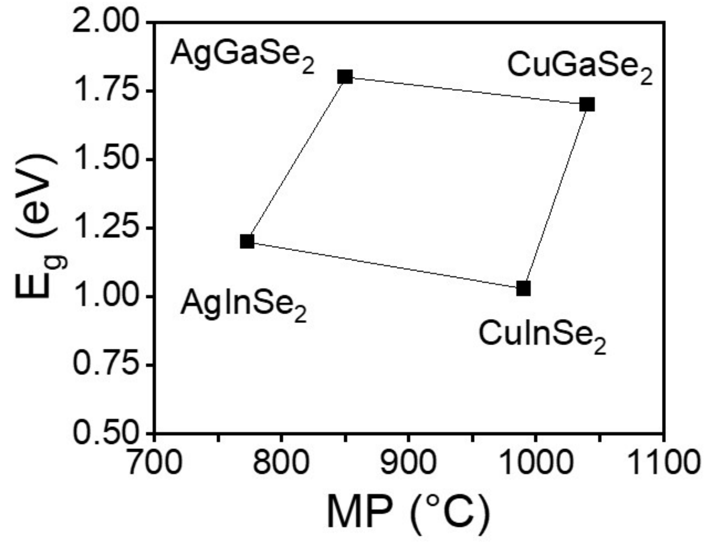

Figure 3.2 Melting point (°C) and band gap (eV) values for the ternary chalcogenide compounds of interest in the (Ag,Cu)(In,Ga)Se_2 alloy system. Figure adapted from [18].

Additionally, some ACIGS films have shown deep cavities and voids, which may result in shunting, and Ag_2Se phase segregation due to slow Ag diffusion [22], [23]. These limitations show that ACIGS, particularly during low-temperature growth, requires further optimization.

3.1.4 Kinetic Aspects of CIGS

A summary of reaction kinetic parameters for the formation of $CuInSe_2$ (CIS) and $CuGaSe_2$ (CGS) from different precursors are shown in Table 3.1 based on experiments using high-temperature x-ray diffraction (HT-XRD). Note that the pure metal stacks were annealed in a Se environment. The Avrami models suggested formation of all alloys to be diffusion-controlled and one-dimensional. The rates of formation for CIS and CIGS by selenization of metal precursors were similar to each other and both greater than that for CGS.

Table 3.1 Summary of reaction kinetics determined by high-temperature x-ray diffraction (HT-XRD) for CIS, CGS, and CIGS.

Stack	Alloy	Avrami exponent	Activation Energy (eV/molecule)	Source
glass/InSe/CuSe	CIS	0.5-0.8	0.68	[24]
glass/Mo/Cu/In	CIS	0.6-0.8	1.29	[25]
glass/GaSe/CuSe	CGS	0.68-0.73	1.29	[26]
glass/Mo/Cu/Ga	CGS	0.55-0.61	1.13	[27]
glass/Mo/Cu/In/Ga	CIGS	0.45-0.58	1.49	[28]

3.2 CIGS Vapor Deposition Techniques and Implications

Typically, CIGS lab-scale devices are grown on 1 mm thick soda-lime glass (SLG) substrates. A Mo back contact deposited by DC sputtering is the standard for CIGS devices because it is conductive, can withstand high temperatures during CIGS deposition, and does not react with any CIGS cations. A bilayer Mo-$MoSe_2$ back contact has been widely adopted because it reduces series resistance, improves adhesion, and is thought to produce a good ohmic or low Schottky barrier contact. Details about typical vacuum-based CIGS deposition techniques are summarized in the following section. A thin CdS buffer layer is grown by chemical bath deposition (CBD) and creates an optimized heterojunction. Alternative buffer layers are an active area of research to (i) remove the use of toxic Cd during fabrication, (ii) use a vapor deposited material to streamline module manufacturing, and (iii) optimize band alignment for varying alloy compositions [29]. The n-type window layer, or transparent conductive oxide (TCO), completes the pn-junction and is usually made up of a bilayer of ZnO/ZnO:Al deposited by rf sputtering. Research devices are completed with front contact metallic grids.

The rest of this section will describe co-evaporation processes commonly used for CIGS deposition. During CIGS growth, CGI (Equation 3.3) is used to describe a Cu-poor film (0<CGI<1.0) and a Cu-rich film (CGI>1.0).

3.2.1 Co-Evaporation

Co-evaporation is a physical vapor deposition technique typically used to deposit high efficiency CIGS films. The metal constituents are evaporated from four individual elemental sources under a constant Se flux. This technique allows for high control of composition during absorber deposition. Co-evaporation recipes commonly used are described below.

- *Single-Stage:* This is the simplest co-evaporation procedure where all elements are evaporated at a constant flux to obtain the desired composition at a constant substrate temperature (typically 550°C). These films do not produce optimized or high performance devices.

- *Boeing-type:* In the Boeing-type processes a two-stage growth is used. During growth elemental source fluxes are changed such that the layer is initially grown Cu-rich then Cu-poor. The first Cu-rich stage results large grains and the formation of CIGS and $Cu_{2-x}Se$ phases. During the second stage, the Cu flux is reduced to result in a Cu-poor film which is necessary for optimized device performance and the removal of detrimental $Cu_{2-x}Se$ phases [30]. However, this recipe is limited because the film quality is dependent on the quality of the first stage which likely has many defects [31].

- *Three-Stage:* The highest efficiency co-evaporated films are produced using a three-stage process. A schematic of the typical process is shown in Figure 3.3. This technique relies on end point detection to identify phase and composition changes based on relative emissivities. Under a constant, high Se flux the metal fluxes and substrate temperature are changed for high control of composition. During the first stage In, Ga, and Se are evaporated at a substrate temperature of 350°C resulting in the formation of $(InGa)_2Se_3$. Cu and Se are evaporated with a substrate temperature of 550°C during the second stage to convert the material to chalcopyrite CIGS and increase grain size. In, Ga, and Se are evaporated during the third stage to turn the film Cu-poor and smooth the surface [32], [33]. This results in a graded absorber with higher Ga contents at both interfaces; Ga grading aids electron transport toward the front interface, and thus improved carrier collection [34]. Variations to the time and relative fluxes are used to change the composition of the alloy throughout the film. Although this process results in high-efficiency CIGS absorbers, it is too expensive, long (~1 hour), and technologically involved to be industrially competitive.

- *CuPRO:* The CuPRO process (Cu-poor, Cu-rich, Cu-off) is a variation of the three-stage process where only the Cu flux is varied during deposition and a constant substrate temperature, often 500˚C, is used [35]. A schematic of the typical process is shown in Figure 3.3. This technique also relies on end point detection. During the first stage Cu, In, and Ga are evaporated under a Se overpressure such that a Cu-poor layer with small grains is deposited. The Cu flux is increased such that the film recrystallizes and passes from Cu-poor to stoichiometric. Growth of CIGS and secondary phase $Cu_\delta Se$ follows resulting in a Cu-rich film. The Cu flux is then turned off. The CIGS returns to stoichiometry and the $Cu_\delta Se$ is consumed. Deposition continues until the film is sufficiently Cu-poor.

3.2.2 Recrystallization and Grain Growth of CIGS during Deposition

During typical multi-stage co-evaporation deposition processes, a Cu-rich stage is necessary to induce recrystallization and grain growth.

During the first stage, a Cu-poor (CuPRO) or Cu-free (3-stage) layer is deposited and results in the nucleation and growth of small grains and depends on substrate temperature. During the second stage, an increase in the Cu flux (CuPRO) or only Cu deposition (3-stage) induces a transition to stoichiometry, then a Cu-rich composition. Recrystallization and grain growth of the CIGS layer is attributed to this second stage. Klenk et al. proposed a vapor-liquid-solid (VLS) grain growth mechanism by liquid Cu-Se phase which forms when the film is Cu-rich in the grain boundaries [36]. Enhanced Cu diffusion in grain boundaries during Stage 2 has been observed by atom probe tomography [37]. Cubic and tetragonal

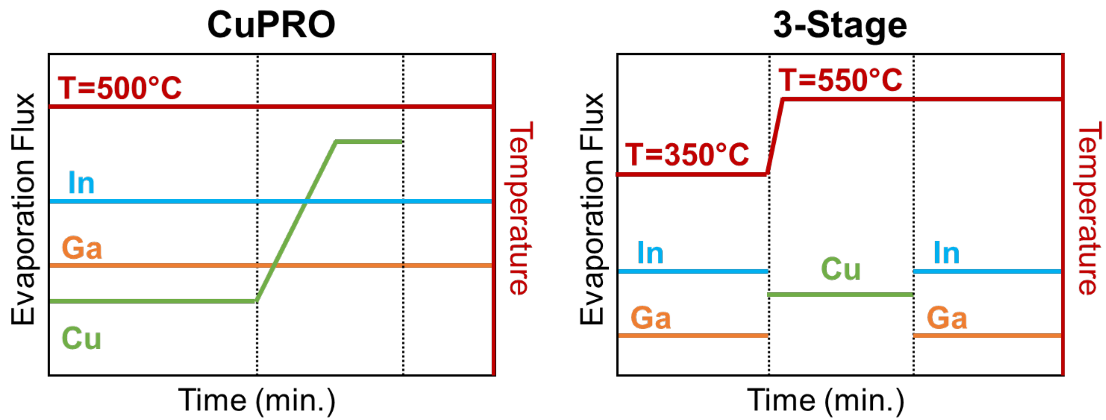

Figure 3.3 Qualitative schematics are shown for typical CIGS co-evaporation depositions based on CuPRO and 3-stage processes. Both are conducted under a constant Se overpressure which is not drawn.

$Cu_{2-x}Se$ phases have been identified on CIGS crystallites and along grain boundaries, respectively. It is thought that the tetragonal $Cu_{2-x}Se$ phase forms first and is where CIGS formation initiates [38]. The development of the absorber during Stage 2 is shown in Figure 3.4 as adapted from [39]. The ordered vacancy compounds (OVC) are attributed to the ordered defect pair (ODP), $2V_{Cu}^{-} + In_{Cu}^{+}$, which has a very low formation energy [40]. The ODP results in OVCs such as the 1:3:5 ($CuIn_3Se_5$) and 1:5:8 ($CuIn_5Se_8$). Initially, Cu-poor OVCs form. As more Cu is introduced, stoichiometric CIGS and larger grains form. Eventually the OVC phases disappear and the excess Cu forms a $Cu_{2-x}Se$ phase, which eventually segregates to the surface, and large grains result [39].

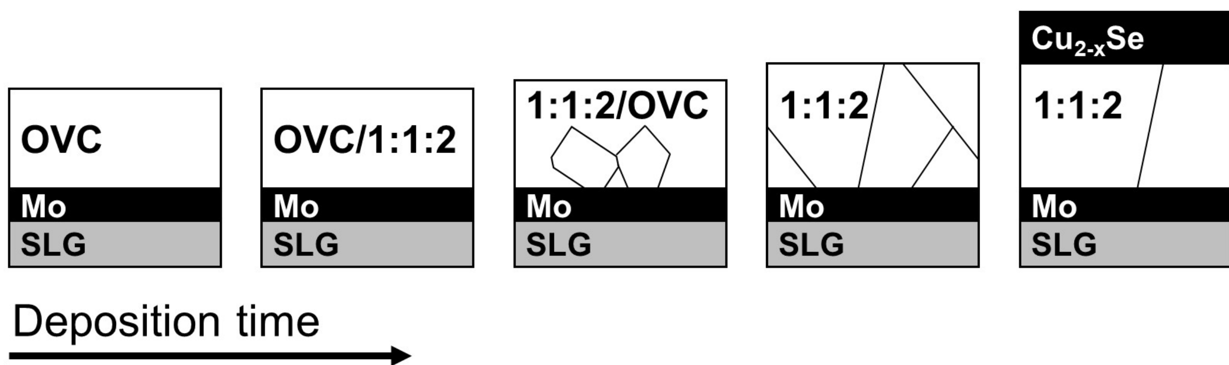

Figure 3.4 Schematic showing the growth and the phases present during Stage 2 of a multi-stage CIGS deposition. Phases drawn represent ordered vacancy compounds (OVC) and stoichiometry (1:1:2). This figure is adapted and re-drawn from [39].

A grain boundary migration mechanism has since been proposed arguing that a $Cu_{2-x}Se$ phase only enhances but does not activate recrystallization [31]. In this mechanism the high defect density at grain

boundaries pins the Fermi energy level higher than that of the grain resulting in downward band bending. This results in higher Cu mobility into the grain.

3.3 Alkali Treatments

Record performing CIGS devices rely on alkali halide post-deposition treatments (PDTs) which typically are conducted in Se and/or S atmospheres. Original alkali incorporation was of Na which originated by diffusion from the SLG substrate, through the Mo back contact, and into the CIGS during the high-temperature deposition process. The benefits of Na incorporation were fully realized by introducing a controlled flux of NaF by PDT. Na incorporation from SLG and PDT result in passivated grain boundaries which improves device performance by V_{oc} and FF gains due to higher net p-type doping levels [41], [42]. NaF-PDT benefits are largely attributed to enhanced hole concentration and conductivity [14], though, too high of Na content can lead to device performance losses [43]. Na has been shown to diffuse through grain boundaries by atom probe tomography [44], [37].

Recent CIGS efficiency improvements have resulted from heavy alkali PDTs using KF [45], CsF, and RbF [46] and various combinations. These treatments result in the formation of surface compounds and improve the device heterojunction. Treatments using heavy alkali metals mostly benefit bulk versus surface electronic properties and accumulate at grain boundaries. They result in reduced bulk recombination and band bending at grain boundaries [47].

Alkali treatments are thought to mainly impact the electrical properties of the CIGS because they mainly segregate to surfaces and grain boundaries. It has been demonstrated that alkali fluoride treatments can be used to passivate electronically active defects in low-temperature deposited CIGS. However, grain growth does not occur [48]. Similar results were noted for alkali chloride and bromide compounds [49]. Additionally, Na has been shown to have no effect on $CuInSe_2$ nucleation and growth, supporting this result [50]. Fluoride compounds are the standard for PDTs to minimize halide contamination. It is assumed that the alkali halide decomposes on the surface as enabled by the presence of Se. A reaction occurs to form volatile SeF_6 which has sufficient vapor pressure to remove F from the system, leaving only trace amounts of F on the surface [51].

3.4 Recrystallization and Grain Growth of CdTe

Inspiration for work presented in this thesis stems from the $CdCl_2$ treatments of CdTe. CdTe is a II-VI direct band gap p-type semiconductor used as a thin-film photovoltaic absorber material. CdTe represents the majority of the thin film photovoltaic market due to its high-rate, low-temperature deposition process followed by a cadmium chloride ($CdCl_2$) activation treatment to passivate grain boundaries.

Early thin-film CdTe processing used $CdCl_2$ as a sintering agent [52] which was found to improve device parameters and grain size [53], [54]. Upon transitioning to thin-film CdTe deposited by close space vapor transport, where a $CdCl_2$ sintering agent is not used, it was determined that $CdCl_2$ incorporation was necessary to produce high-efficiency cells. A post-deposition $CdCl_2$ solution treatment was introduced and resulted in large grain growth [55] and reduced surface and interfacial energies [56]. A vapor phase $CdCl_2$ treatment was developed resulting in more uniform recrystallization, more densely-packed grains, and enhanced CdTe/CdS interdiffusion [57], [58]. The treatment results in grain growth and recrystallization for low-temperature deposited CdTe and shows little to no change to high-temperature deposited CdTe [59]. In fact, the treatment does not always induce recrystallization and grain growth. It is still important as it improves device performance by altering the defect structure [60].

It has been shown that Cl segregates into grain boundaries and increases current collection. By Avrami kinetics it has been suggested that Cl grain boundary diffusion dominates and the resulting recrystallization is diffusion-controlled [61]. The Cl replaces Cd, forming Te-Cl compounds that are liquid or vapor phases and promote grain growth and recrystallization [62], [63], [64]. Replacement of Te has also been reported [64], [65]. The eutectic point of the CdTe-$CdCl_2$ system is 505°C for a $CdCl_2$ molar concentration of 74% which is below the melting point of CdTe [66]. Considering the Te- and Cl-rich grain boundaries, the formation of $TeCl_4$ is possible. $TeCl_4$ has a melting point of 224°C, well within typical treatment temperatures, and can enhance grain boundary mobility [67]. $CdCl_2$ thus acts as a transport agent to activate grain growth as annealing temperature approaches the eutectic and intermediate phases form [68].

3.5 References

[1] T. Kawashima, S. Adachi, H. Miyake, and K. Sugiyama, "Optical constants of $CuGaSe_2$ and $CuInSe_2$", J. Appl. Phys., 84, 9, 5202-5209, 1998. DOI: 10.1063/1.368772.

[2] A. Rockett and R. Birkmire, "$CuInSe_2$ for photovoltaic applications", J. Appl. Phys., 70, 7, 81-97, 1991.

[3] J. Jaffe and A. Zunger, "Electronic structures of the ternary chalcopyrite semiconductors $CuAlS_2$, $CuGaS_2$, $CuInS_2$, $CuAlSe_2$, $CuGaSe_2$, and $CuInSe_2$", Physical Review B, 28, 10, 5822-5847, 1983. DOI: 10.1103/PhysRevB.28.5822.

[4] K. Momma and F. Izumi, "VESTA 3 for three-dimensional visualization of crystal, volumetric, and morphology data", J. Appl. Crystallogr., 44, 1272-1276, 2011.

[5] B. Huang, S. Chen, H. Deng, L. Wang, M. Contreras, R. Noufi, and S. Wei, "Origin of Reduced Efficiency in Cu(In,Ga)Se_2 Solar Cells with High Ga Concentration: Alloy Solubility Versus Intrinsic Defect", IEEE Journal of Photovoltaics, 4, 1, 477-482, 2014. DOI: 10.1109/JPHOTOV.2013.2285617.

[6] T. Tinoco, C. Rincón, M. Quintero, and G. Sánchez Pérez, "Phase Diagram and Optical Energy Gaps for $CuIn_yGa_{1-y}Se_2$ Alloys", Physica Status Solidi (a), 124, 427-434, 1991. DOI: 10.1002/pssa.2211240206.

[7] S. Chichibu, T. Mizutani, K. Murakami, T. Shioda, T. Kurafuji, H. Nakanishi, S. Niki, P. Fons, and A. Yamada, "Band gap energies of bulk, thin-film, and epitaxial layers of $CuInSe_2$ and $CuGaSe_2$", J. Appl. Phys., 83, 7, 1998. DOI: 10.1063/1.366588.

[8] D. Albin, J. Carapella, J. Tuttle, and R. Noufi, "The Effect of Copper Vacancies on the Optical Bowing of Chalcopyrite $Cu(In,Ga)Se_2$ Alloys", MRS Proceedings, 228, 13, 267-272, 1991. DOI: 10.1557/proc-228-267.

[9] S. Wei, S. Zhang, and A. Zunger, "Effects of Ga addition to $CuInSe_2$ on its electronic, structural, and defect properties", Applied Physics Letters, 72, 24, 3199-3201, 1998. DOI: 10.1063/1.121548.

[10] C. Huang, "Effect of Ga content on $Cu(In,Ga)Se_2$ solar cells studied by numerical modeling", Journal of Physics and Chemistry of Solids, 69, 330-334, 2008. DOI: 10.1016/j.jpcs.2007.07.093.

[11] A. Stokes, M. Al-Jassim, A. Norman, D. Diercks, and B. Gorman, "Nano-scale Insight into the P-N Junction of Alkali Incorporated $Cu(In,Ga)Se_2$ Solar Cells", Progress in Photovoltaics: Research and Applications, 25, 9, 764-772, 2017. DOI: 10.1002/pip.2883.

[12] J. Boyle, B. McCandless, W. Shafarman, and R. Birkmire, "Structural and optical properies of $(Ag,Cu)(In,Ga)Se_2$ polycrystalline thin film alloys", J. Appl. Phys. 115, 223504, 2014. DOI: 10.1063/1.4880243.

[13] J.L. Shay and J.H. Wernick, Ternary Chalcopyrite Semiconductors: Growth, Electronic Properties, and Applications, Pergamon Press, 1975.

[14] P.T. Erslev, J. Lee, G.M. Hanket, W.N. Shafarman, and J.D. Cohen, "The electronic structure of $Cu(In_{1-x}Ga_x)Se_2$ alloyed with silver", Thin Solid Films, 519, 7296-7299, 2011. DOI: 10.1016/j.tsf.2011.01.368.

[15] L. Chen, J. Lee, and W. Shafarman, "The Comparison of $(Ag,Cu)(In,Ga)Se_2$ and $Cu(In,Ga)Se_2$ Thin Films Deposited by Three-Stage Coevaporation", IEEE Journal of Photovoltaics, 4, 1, 2014.

[16] K. Kim, J. Park, J. Yoo, J. Cho, H. Lee, and J. Yun, "Ag incorporation in low-temperature grown $Cu(In,Ga)Se_2$ solar cells using Ag precursor layers", Solar Energy Materials & Solar Cells, 146, 114-120, 2016. DOI: 10.1016/j.solmat.2015.11.028.

[17] M. Edoff, T. Jarmar, N. Nilsson, E. Wallin, D. Högström, O. Stolt, O. Lundberg, W. Shafarman, and L. Stolt, "High V_{oc} in $(Cu,Ag)(In,Ga)Se_2$ Solar Cells", IEEE Journal of Photovoltaics, 7, 6, 1789-1794, 2017. DOI: 10.1109/JPHOTOV.2017.2756058.

[18] G. Hanket, J. Boyle, and W. Shafarman, “Characterization and device performance of $(Ag,Cu)(In,Ga)Se_2$ absorber layers”, Conference Record of the IEEE Photovoltaic Specialists Conference, 2009. DOI: 10.1109/PVSC.2009.5411241.

[19] J. Avon, K. Yoodee, and J. Woolley, “Solid solution, lattice parameter values, and effects of electronegativity in the $(Cu_{1-x}Ag_x)(Ga_{1-y}In_y)(Se_{1-z}Te_z)_2$ alloys”, J. Appl. Phys., 55, 524-535, 1984. DOI: 10.1063/1.333058.

[20] J. Boyle, B. McCandless, G. Hanket, and W. Shafarman, “Structural characterization of the $(AgCu)(InGa)Se_2$ thin film alloy system for solar cells”, Thin Solid Films, 519, 7292-7295, 2011. DOI: 10.1016/j.tsf.2011.01.138.

[21] K. Sopiha, J. Larsen, O. Donzel-Gargand, F. Khavari, J. Keller, M. Edoff, C. Platzer-Björkman, C. Persson, and J. Scragg, “Thermodynamic stability, phase separation and Ag grading in $(Ag,Cu)(In,Ga)Se_2$ solar absorbers”, Journal of Materials Chemistry A, 8, 8740-8751, 2020. DOI: 10.1039/d0ta00363h.

[22] S. Essig, S. Paetel, T. Friedlmeier, and M. Powalla, “Challenges in the deposition of $(Ag,Cu)(In,Ga)Se_2$ absorber layers for thin-film solar cells”, J. Phys. Mater., 4, 2021. DOI: 10.1088/2515-7639/abd73d.

[23] X. Zhang, A. Yamada, and M. Kobayashi, “High-temperature fabrication of $Ag(In,Ga)Se_2$ thin films for applications in solar cells”, Phys. Status Solidi A, 214, 10, 2017. DOI: 10.1002/pssa.201700042.

[24] S. Kim, W. Kim, R. Kaczynski, R. Acher, S. Yoon, T. Anderson, O. Crisalle, E. Payant, and S. Li, “Reaction kinetics of $CuInSe_2$ thin films grown from bilayer InSe/CuSe precursors”, Journal of Vacuum Science & Technology A: Vacuum, Surfaces, and Films, 23, 2, 310-315, 2005. DOI: 10.1116/1.1861051.

[25] W. Kim, E. Payzant, S. Yoon, and T. Anderson, “In situ investigation on selenization kinetics of Cu-In precursor using time-resolved, high temperature X-ray diffraction”, Journal of Crystal Growth, 294, 231-235, 2006. DOI: 10.1016/j.jcrysgro.2006.05.066.

[26] W. Kim, E. Payzant, S. Kim, S. Speakman, O. Crisalle, and T. Anderson, “Reaction kinetics of $CuGaSe_2$ formation from a GaSe/CuSe bilayer precursor film”, Journal of Crystal Growth, 310, 2987-2994, 2008. DOI: 10.1016/j.jcrysgro.2008.01.034.

[27] W. Kim, E. Payzant, T. Anderson, and O. Crisalle, “In situ investigation of the selenization kinetics of Cu-Ga precursors using time-resolved high-temperature X-ray diffraction”, Thin Solid Films, 515, 5837-5842, 2007. DOI: 10.1016/j.tsf.2006.12.173.

[28] W. Kim, “Study of Reaction Pathways and Kinetics in $Cu(In_xGa_{1-x})Se_2$ Thin Film Growth”, 2006, [Thesis].

[29] W. Witte, S. Spiering, and D. Hariskos, “Substitution of the CdS buffer layer in CIGS thin-film solar cells: Status of current research and record cell efficiencies”, Vakuum in Forschung und Praxis, 26, 1,

23-27, 2014. DOI: 10.1002/vipr.201400546.

[30] W. Devaney and R. Mickelsen, "Vacuum deposition processes for $CuInSe_2$ and $CuInGaSe_2$ based solar cells", Solar Cells, 24, 19-26, 1988. DOI: 10.1016/0379-6787(88)90032-4.

[31] N. Barreau, T. Painchaud, F. Couzinié-Devy, L. Arzel, and J. Kessler, "Recrystallization of CIGSe layers grown by three-step processes: A model based on grain boundary migration", Acta Materialia, 58, 5572-5577, 2010. DOI: 10.1016/j.actamat.2010.06.025.

[32] A. Gabor, J. Tuttle, D. Albin, M. Contreras, R. Noufi, and A. Hermann, "High-efficiency $CuIn_xGa_{1-x}Se_2$ solar cells made from $(In_x, Ga_{1-x})_2Se_3$ precursor films", Appl. Phys. Lett., 198, 1994. DOI: 10.1063/1.112670.

[33] C. Huang, W. Chuang, C. Lin, Y. Jan, and Y. Shih, "Deposition technologies of high-efficiency CIGS solar cells: Development of two-step and co-evaporation processes", Crystals, 8, 2018. DOI: 10.3390/cryst8070296.

[34] T. Dullweber, G. Hanna, U. Rau, and H. Schock, "A new approach to high-efficiency solar cells by band gap grading in $Cu(In,Ga)Se_2$ chalcopyrite semiconductors", Solar Energy Materials & Solar Cells, 67, 145-150, 2001.

[35] J. Kessler, C. Chityuttakan, J. Lu, J. Schöldström, and L. Stolt, "$Cu(In,Ga)Se_2$ Thin Films Grown with a Cu-Poor/Rich/Poor Sequence: Growth Model and Structural Considerations", Progress in Photovoltaics: Research and Applications, 11, 319-331, 2003. DOI: 10.1002/pip.495.

[36] R. Klenk, T. Walter, H. Schock, and D. Cahen, "A Model for the Successful Growth of Polycrystalline Films of $CuInSe_2$ by Multisource Physical Vacuum Evaporation", Advanced Materials, 5, 2, 114-119, 1993.

[37] F. Couzinie-Devy, E. Cadel, N. Barreau, L. Arzel, and P. Pareige, "Atom probe study of Cu-poor to Cu-rich transition during $Cu(In,Ga)Se_2$ growth", Applied Physics Letters, 99, 2011. DOI: 10.1063/1.3665948.

[38] R. Noufi, Y. Yan, J. Abu-Shama, K. Jones, M. Al-Jassim, B. Keyes, J. Alleman, and K. Ramanathan, "Investigation of the microstructure of $Cu(In,Ga)Se_2$ thin films used in high-efficiency devices", Conference Record of the IEEE Photovoltaic Specialists Conference, 2002. DOI: 10.1109/pvsc.2002.1190613.

[39] R. Caballero, C. Kaufmann, V. Efimova, T. Rissom, V. Hoffmann, and H. Schock, "Investigation of $Cu(In,Ga)Se_2$ thin-film formation during the multi-stage co-evaporation process", Progress in Photovoltaics, 21, 30-46, 2013. DOI: 10.1002/pip.1233.

[40] S. Zhang, S. Wei, and A. Zunger, "Stabilization of ternary compounds via ordered arrays of defect pairs", Physical Review Letters, 78, 4059-4062, 1997. DOI: 10.1103/PhysRevLett.78.4059.

[41] D. Rudmann, A. da Cunha, M. Kaelin, F. Kurdesau, H. Zogg, A. Tiwari, and G. Bilger, "Efficiency enhancement of Cu(In,Ga)Se_2 solar cells due to post-deposition Na incorporation", Appl. Phys. Lett., 84, 7, 1129-1131, 2004. DOI: 10.1063/1.1646758.

[42] F. Pianezzi, P. Reinhard, A. Chirilă, B. Bissig, S. Nishiwaki, S. Buecheler, and A. Tiwari, "Unveiling the effects of post-deposition treatment with different alkaline elements on the electronic properties of CIGS thin film solar cells", Phys. Chem. Chem. Phys., 16, 8843-8851, 2014. DOI: 10.1039/c4cp00614c.

[43] D. Rudmann, D. Brémaud, A. da Cunha, G. Bilger, A. Strohm, M. Kaelin, H. Zogg, and A. Tiwari, "Sodium incorporation strategies for CIGS growth at different temperatures", Thin Solid Films, 480-481, 55-60, 2005. DOI: 10.1016/j.tsf.2004.11.071.

[44] A. Stokes, M. Al-Jassim, D. Diercks, A. Clarke, and B. Gorman, "Impact of Wide-Ranging Nanoscale Chemistry on Band Structure at Cu(In,Ga)Se_2 Grain Boundaries", Scientific Reports, 7, 1, 1-11, 2017. DOI: 10.1038/s41598-017-14215-0.

[45] A. Chirilă, P. Reinhard, F. Pianezzi, P. Bloesch, A. Uhl, C. Fella, L. Kranz, D. Keller, C. Gretener, H. Hagendorfer, D. Jaeger, R. Erni, S. Nishiwaki, S. Buecheler, and A. Tiwari, "Potassium-induced surface modification of Cu(In,Ga)Se_2 thin films for high-efficiency solar cells", Nature Materials, 12, 1107-1111, 2013. DOI: 10.1038/nmat3789.

[46] P. Jackson, R. Wuerz, D. Hariskos, E. Lotter, W. Witte, and M. Powalla, "Effects of heavy alkali elements in Cu(In,Ga)Se_2 solar cells with efficiencies up to 22.6%", Phys. Status Solidi RRL, 10, 8, 583-586, DOI: 10.1002/pssr.201600199.

[47] S. Siebentritt, E. Avancini, M. Bär, J. Bombsch, E. Bourgeois, S. Buecheler, R. Carron, C. Castro, S. Duguay, R. Félix, E. Handick, D. Hariskos, V. Havu, P. Jackson, H. Komsa, T. Kunze, M. Malitckaya, R. Menozzi, M. Nesladek, N. Nicoara, M. Puska, M. Raghuwanshi, P. Pareige, S. Sadewasser, G. Sozzi, A. Tiwari, S. Ueda, A. Vilalta-Clemente, T. Weiss, F. Werner, R. Wilks, W. Witte, and M. Wolter, "Heavy Alkali Treatment of Cu(In,Ga)Se_2 Solar Cells: Surface versus Bulk Effects", Advanced Energy Materials, 10, 2020. DOI: 10.1002/aenm.201903752.

[48] G. Rajan, B. Belfore, S. Karki, D. Poudel, H. Kahoui, N. Lanham, E. Palmiotti, S. Soltanmohammad, A. Rockett, and S. Marsillac, "Impact of Post-Deposition Recrystallization by Alkali Fluorides on Cu(In,Ga)Se_2 Thin-Film Materials and Solar Cells", Thin Solid Films, 690, 2019. DOI: 10.1016/j.tsf.2019.137526.

[49] E. Palmiotti, S. Soltanmohammad, A. Rockett, G. Rajan, S. Karki, B. Belfore, and S. Marsillac, "Post-Deposition Recrystallization of Chloride Treated Cu(In,Ga) Se_2 Thin-Film Solar Cells", 2018 IEEE 7th World Conference on Photovoltaic Energy Conversion (WCPEC) (A Joint Conference of 45th IEEE

PVSC, 28th PVSEC & 34th EU PVSEC), 163-166, 2018, DOI: 10.1109/PVSC.2018.8547595.

[50] S. Kim, H. Park, E. Lee, J. Han, S. Lee, C. Jeon, D. Jung, J. Jeong, and W. Kim, "Role of Na in reaction pathways and kinetics of $CuInSe_2$ formation from stacked binary precursors", Thin Solid Films, 519, 7250-7253, 2011. DOI: 10.1016/j.tsf.2010.12.222.

[51] A. Laemmle, R. Wuerz, T. Schwarz, O. Cojocaru-Mirédin, P. Choi, and M. Powalla, "Investigation of the diffusion behavior of sodium in $Cu(In,Ga)Se_2$ layers", J. Appl. Phys., 115, 2014. DOI: 10.1063/1.4871457.

[52] N. Nakayama, H. Matsumoto, K. Yamaguchi, S. Ikegami, and Y. Hioki, "Ceramic Thin Film CdTe Cell", Japan Journal of Applied Physics, 15, 2281-2282, 1976. DOI: 10.1143/JJAP.15.2281.

[53] J.T. Moon, K.C. Park, and H.B. Im, "Photovoltaic Properties of CdS/CdTe Solar Cells Sintered with $CdCl_2$", Solar Energy Materials, 18, 53-60, 1988. DOI: 10.1016/0165-1633(88)90044-5.

[54] J.S. Roh and H.B. Im, "Effects of $CdCl_2$ in CdTe on the properties of sintered CdS/CdTe solar cells", Journal of Materials Science, 23, 2267-2272, 1988. DOI: 10.1007/BF01115799.

[55] B.E. McCandless and R.W. Birkmire, "Analysis of post deposition processing for CdTe/CdS thin film solar cells", Solar Cells, 31, 527-535, 1991. DOI: 10.1016/0379-6787(91)90095-7.

[56] B. McCandless, L. Moulton, and R. Birkmire, "Recrystallization and sulfur diffusion in $CdCl_2$-treated CdTe/CdS thin films", Progress in Photovoltaics: Research and Applications, 5, 249-260, 1997. DOI: 10.1002/(SICI)1099-159X(199707/08)5:4<249::AID-PIP178>3.0.CO;2-S.

[57] B. McCandless, I. Youm, and R. Birkmire, "Optimization of vapor post-deposition processing for evaporated CdS/CdTe solar cells", Progress in Photovoltaics: Research and Applications, 7, 21-30, 1999. DOI: 10.1002/(SICI)1099-159X(199901/02)7:1<21::AID-PIP244>3.0.CO;2-D.

[58] T. Zhou, N. Reiter, R. Powell, R. Sasala, and P. Meyers, "Vapor chloride treatment of polycrystalline CdTe/CdS films", Conference Record of the IEEE Photovoltaic Specialists Conference, 1994. DOI: 10.1109/wcpec.1994.519818.

[59] J. Quadros, A. Pinto, and H. Moutinho, "Microtexture of chloride treated CdTe thin films deposited by CSS technique", J. Mater. Sci., 43, 573-579, 2009. DOI: 10.1007/s10853-007-1708-5.

[60] H. Moutinho, R. Dhere, M. Al-Jassim, D. Levi, and L. Kazmerski, "Investigation of induced recrystallization and stress in close-spaced sublimated and radio-frequency magnetron sputtered CdTe thin films", Journal of Vacuum Science & Technology A, 17, 1793-1798, 1999. DOI: 10.1116/1.581892.

[61] M. Kim, S. Sohn, and S. Lee, "Reaction kinetics study of CdTe thin films during $CdCl_2$ heat treatment", Solar Energy Materials and Solar Cells, 95, 8, 2295-2301, 2011. DOI: 10.1016/j.solmat.2011.03.044.

[62] M. Terheggen, H. Heinrich, G. Kostorz, A. Romeo, D. Baetzner, A.N. Tiwari, A. Bosio, and N. Romeo, "Structural and chemical interface characterization of CdTe solar cells by transmission electron microscopy", Thin Solid Films, 431, 262-266, 2003. DOI: 10.1016/S0040-6090(03)00268-2.

[63] M. Terheggen, H. Heinrich, G. Kostrorz, D. Baetzner, A. Romeo, and A.N. Tiwari, "Analysis of Bulk and Interface Phenomena in CdTe/CdS Thin-Film Solar Cells", Interface Science, 12, 259-266, 2004. DOI: 10.1023/B:INTS.0000028655.11608.c7.

[64] C. Li, Y. Wu, J. Poplawsky, T. Pennycook, N. Paudel, W. Yin, S. Haigh, M. Oxley, A. Lupini, M. Al-Jassim, S. Pennycook, and Y. Yan, "Grain-Boundary-Enhanced Carrier Collection in CdTe Solar Cells", Physical Review Letters, 112, 2014. DOI: 10.1103/PhysRevLett.112.156103.

[65] C. Li, J. Poplawsky, N. Paudel, T. Pennycook, S. Haigh, M. Al-Jassim, Y. Yan, and S. Pennycook, "S–Te Interdiffusion within Grains and Grain Boundaries in CdTe Solar Cells", IEEE Journal of Photovoltaics, 4, 6, 2014.

[66] H. Tai and S. Hori, "Equilibrium Phase Diagrams of the CdTe-$CdCl_2$ and CdTe-$CdBr_2$ Systems", J. Japan Inst. Metals, 40, 722-725, 1976.

[67] J. Winger and M. Scarpulla, "Grain Growth in CdTe Films During $CdCl_2$ Treatment : $TeCl_4$ Theory", 2019 IEEE 46th Photovoltaic Specialists Conference, 2019. DOI: 10.1109/PVSC40753.2019.8980923.

[68] D. Albin, M. Amarasinghe, M. Reese, J. Mosely, H. Moutinho, and W. Metzger, "Colossal grain growth in Cd(Se,Te) thin films and their subsequent use in CdTe epitaxy by close-spaced sublimation", J. Phys. Energy, 3, 2021. DOI: 10.1088/2515-7655/abd297.

CHAPTER 4

A THERMODYNAMIC EVALUATION OF METAL HALIDES FOR THE RECRYSTALLIZATION OF $Cu(In,Ga)Se_2$

Paper submitted to *Progress in Photovoltaics: Research and Applications*

Elizabeth Palmiotti[a*], Sylvain Marsillac[b], and Angus Rockett[a]

[a] Colorado School of Mines, Golden, CO 80401 U.S.A.

[b] Old Dominion University, Norfolk, VA 23529 U.S.A.

Abstract

CdTe films are deposited at low temperatures and recrystallized to photovoltaic device quality using $CdCl_2$ treatments, leading to competitive manufacturing costs. $Cu(In,Ga)Se_2$ (CIGS) typically requires high-temperature, low-rate depositions to produce high-efficiency devices, resulting in higher costs. A similar metal halide treatment of CIGS has been demonstrated by us previously for some metal halide sources. To understand and optimize the process, a thermodynamic evaluation of candidate metal halides for such treatments is presented as a guide for their selection. By comparing bond dissociation energies, mono- and di-halide compounds are proposed to be ideal compounds to act as transport agents. Known recrystallization and temperature reduction benefits by Ag alloying suggests that Ag-halides be used to aid transport of all species. The high vapor pressure and mobility of Ga compounds still poses a problem for metal halide treatment resulting in Ga etching and removal of intentional Ga gradients. Less severe but similar issues with In compounds may occur. Cu compounds have low vapor pressures which may limit transport, however, Cu is highly mobile in CIGS and recrystallization still occurs.

4.1 Introduction

CdTe thin film photovoltaics have a large market presence primarily attributed to a high-rate, low-temperature deposition procedure followed by a rapid $CdCl_2$ annealing treatment. This results in recrystallization [1], absorber activation, and improved device efficiency [2], [3]. Thin-film CdTe-based

photovoltaic processing uses $CdCl_2$ as a sintering agent [4]. It was found that $CdCl_2$ enhances CdTe grain formation and growth and device performance [5], [6]. For CdTe vapor deposition techniques, where a sintering agent is not used, the inclusion of $CdCl_2$ via a solution post-deposition treatment was deemed necessary to produce high-efficiency devices [2]. The treatment improved the CdTe material with demonstration of surface and interfacial energy reductions, CdS/CdTe interdiffusion and interface alloy formation, and CdTe orientation randomization [7]. To improve uniformity and scalability a vapor phase $CdCl_2$ post-deposition treatment by evaporation was developed [8]. This resulted in more uniform recrystallization, smoother and more compact grains, and less residual chlorine in the film [9]. Although there is no consensus about the mechanism for the $CdCl_2$ treatment, it has been shown that Cl diffusion into grain boundaries is a key mechanism for diffusion-limited $CdCl_2$ recrystallization [1]. It has been proposed that upon annealing $CdCl_2$ dissociates to produce Cl ions, which form compounds with Te. These compounds are in the liquid or vapor phase under treatment conditions, encouraging species mobility and recrystallization [10], [11], [12].

By comparison, high-efficiency $Cu(In,Ga)Se_2$ (CIGS) is typically deposited by slow (often hour-long), high-temperature (>500°C), and consequently expensive co-evaporation procedures with capital expenses that challenge profitable manufacturing. High-performing CIGS deposited by co-evaporation typically follows a three-stage [13] or CuPRO [14] sequence. These processes use a Cu-poor/Cu-rich/Cu-poor recipe and rely on the Cu-rich second stage to improve crystallinity of the material and form large grains following grain boundary migration theory [15]. The procedures require substrate temperatures between 500°C and 600°C for high-performance devices. A similar recrystallization treatment to that of CdTe during or after CIGS deposition may reduce the processing time and temperature, either of which would reduce manufacturing expenses. Alkali halide post-deposition treatments have been shown to passivate defects and improve low-temperature (350°C) deposited CIGS films; however, large grains did not form [16]. We have shown that the use of a metal halide transport agent can both recrystallize and improve the grain size of low-temperature, high-rate deposited CIGS with varying changes to composition [17], [18], [19], [20], [21]. By studying the thermodynamic behaviors of various metal halides with respect to experimental conditions and results, the treatments can be better optimized, understood, and interpreted.

In this work a thermodynamic evaluation of various metal halides is presented and compared to experimental CIGS metal halide treatment results to determine which properties of the compounds are most important to effective recrystallization.

4.2 Experimental Examples

A brief review and examples of metal halide treatments are provided for comparison to thermodynamic properties. To induce low-temperature recrystallization and grain growth, metal halides were tested as transport agents. Metal halide selection was based on two requirements: (1) a cation present in the chalcogenide alloy (Cu,Ag)(In,Ga)Se_2 and (2) a halide anion. The cation requirement helps to avoid the introduction of additional elements and minimizes the energetic barrier of exchange during recrystallization. The anion requirement is to introduce a halide transport agent to the system. The resulting list includes Ag, Cu, In, Ga, and Se compounds with F, Cl, Br, and I.

4.2.1 Metal Halide Treatments

Metal halide treatments have been studied for post-deposition [17], [18], [20] and in-situ [19], [21] treatments. Grain growth and recrystallization resulted from treatments with the following: AgBr, CuCl, $CuCl_2$, CuBr, $InCl_3$, and $InBr_3$. Post-deposition treatments were conducted at atmospheric pressure and under vacuum conditions to rapidly test the morphological, structural, and compositional changes by each metal halide. Treatments conducted with $GaCl_3$, $GaBr_3$, and $SeCl_4$ resulted in the decomposition of the CIGS films and formation of various secondary phases. Composition changes were highly sensitive to the metal halide source used and treatment variable (time and temperature). It was found that increased Ga mobility and etching occurred during all treatments. For treatments conducted without excess Se in the system, large amounts of Se depletion resulted. Halide content in the recrystallized films was greater for chloride compounds than for bromides and decreased for treatments held for longer times. In-situ treatments ($InCl_3$ and AgBr) were investigated to have better control over the changing composition during treatment. During growth by a three-stage [13] or CuPRO [14] process, metal evaporation is interrupted after the Cu-rich second stage to introduce the metal halide by flash evaporation. During the third stage the composition is corrected to account for the treatment and to finish with a Cu-poor film. For metal halides tested thus far, Ga mobility is increased and little of the Ga concentration gradient typical of the three-stage process remains after the metal halide treatment. Se content was not impacted by the treatments due to the Se overpressure during deposition.

4.2.2 Metal Halide Treatment Examples

Examples of typical post-deposition treatments that “worked” are as follows. Experimental details are available in Appendix A. SEM micrographs of the CIGS surface and cross-section are shown in Figure 4.1. EDS composition results for all samples are compiled in Figure 4.1. The starting film was Cu-rich and had very small grains. All treatments resulted in large grain size enhancement through the depth of the film.

The CuBr treatment produced the largest and most uniform grains through the film thickness. The $InBr_3$ treatment resulted in comparatively less grain growth and an uneven surface. The $InCl_3$ treatment shows a bimodal distribution of grain sizes. The larger grains show faceting typical of preferential growth along the characteristic (112) planes. All treatments had a significant decrease in Ga-content. The film started with 8.38 at% Ga and all ended with <1 at% Ga showing preferential etching and removal of Ga from the film by the treatments. Halide inclusion in the film occurred for all samples, with the highest from the $InCl_3$ treatment. The smallest variation to overall composition occurred with the CuBr treatment and the most by the $InCl_3$ which notably has a large increase in In-content.

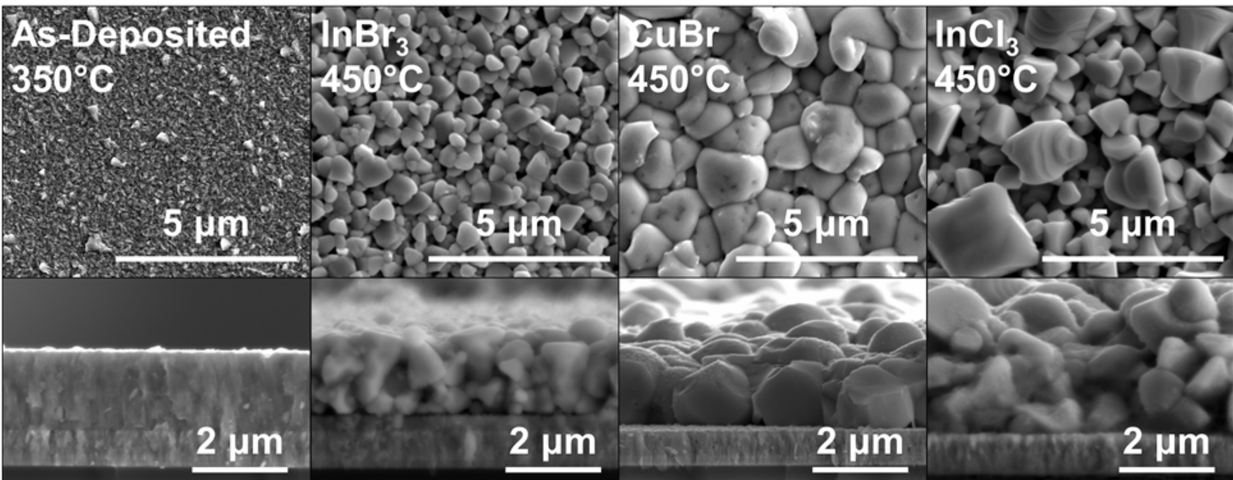

Figure 4.1 Top-view and cross-section SEM images of the CIGS film deposited at 350°C and after treatments with $InBr_3$, CuBr, and $InCl_3$ at 450°C each.

Table 4.1 Composition results collected by EDS for the CIGS film deposited at 350°C and after treatments with $InBr_3$, CuBr, and $InCl_3$ at 450°C each.

	As-dep. (at%)	$InBr_3$ (at%)	CuBr (at%)	$InCl_3$ (at%)
Cu	25.8	27.2	26.6	22.5
In	15.3	22.5	21.7	22.7
Ga	8.4	0.4	1.0	0.11
Se	50.5	48.0	50.1	53.4
Br	-	0.37	0.51	-
Cl	-	-	-	1.27
Cu/III	1.09	1.18	1.17	0.99
Ga/III	0.35	0.017	0.043	0.005

XRD patterns collected for all samples are plotted on a logarithmic scale in Figure 4.2 with peak identifications. For interpretation, the peaks corresponding to the characteristic (112), (220)/(204), and

(312)/(116) planes are shown over smaller 2θ ranges. The as-deposited pattern shows low-intensity broad peaks identified as $CuIn_{0.7}Ga_{0.3}Se_2$ (ICDD Ref. 00-035-1102 [22]). The asymmetry on the lower-angle side of the (112) is typical of low-temperature deposited Cu-rich films and is usually due to a secondary phase ($Cu_{2-x}Se$) [23] that disappears with annealing. All samples show a preferred orientation of (112) parallel to the substrate surface. With all treatments, the CIGS peak intensities increase and the peaks become sharper, indicating improved crystalline quality, recrystallization, and grain growth. The full width at half maximum (FWHM) of the characteristic (112) peak is 0.55° for the as-deposited film, 0.09° with $InBr_3$ recrystallization, 0.06° with CuBr, and 0.09° for $InCl_3$. The loss of Ga after the treatments indicated by EDS (Table 4.1) is reflected in the XRD results. The peaks shift to lower angles as Ga is replaced by larger-radius In. Additionally, peak splitting of the (220)/(204) and (312)/(116) reflections result from all treatments, as expected for the tetragonal chalcopyrite structure as Ga-content changes [24], [25].

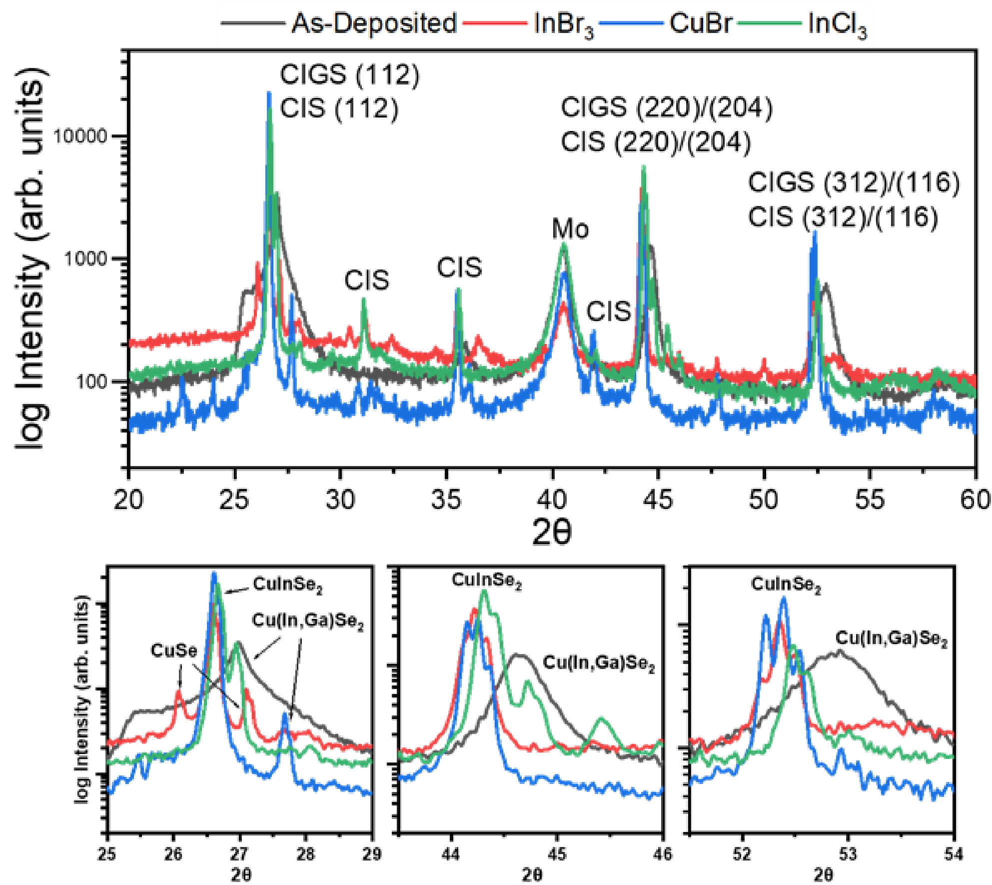

Figure 4.2 XRD results plotted on a logarithmic scale for the CIGS film deposited at 350°C and after treatments with $InBr_3$, CuBr, and $InCl_3$ at 450°C each. The characteristic peaks have been magnified and plotted separately.

4.3 Thermodynamic Evaluation

In this section a review of metal halide properties that, we conclude in this work, contribute to atomic transport during recrystallization is provided. A discussion relating these properties and experimental results to a proposed mechanism is presented in Section 4.4. Note that compounds formed with F have high melting points, high bond energies, and low vapor pressures for the given experimental conditions and therefore are not considered here. Their properties suggest why alkali fluoride post-deposition treatments passivate defects but do not result in grain growth [16].

4.3.1 Bond Dissociation Energies

The bond dissociation energies for all metal halides under consideration are plotted in Figure 3 using values from [26] for all except $CuCl_2$ and $CuBr_2$ which are from [27].

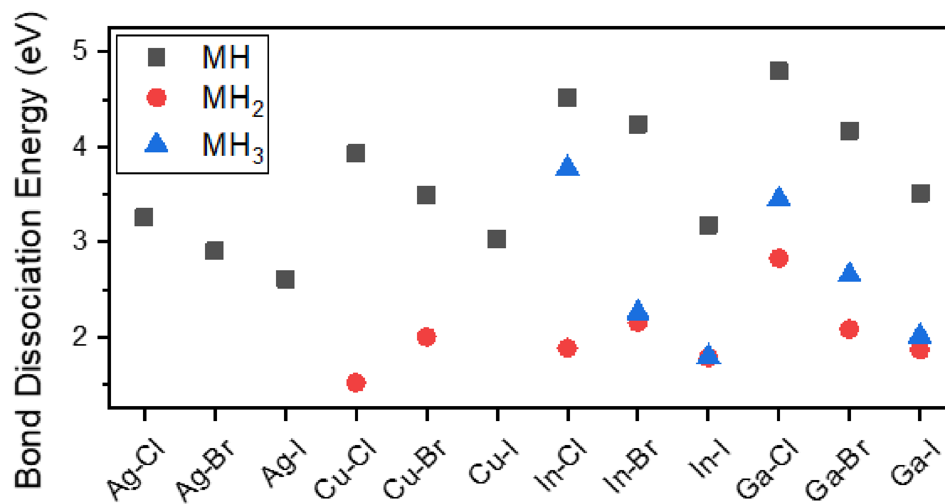

Figure 4.3 Bond dissociation energy (eV) values for metal halide compounds being considered. Blue triangles represent the bond dissociation energy for $MH_3 \rightarrow MH_2 + H$, red circles for $MH_2 \rightarrow MH + H$, and black squares for $MH \rightarrow M + H$.

With respect to the tri-halide compounds ($InCl_3$, $InBr_3$, InI_3, $GaCl_3$, $GaBr_3$, and GaI_3), the bond dissociation energies of the MH_3 (blue triangles), MH_2 (red circles), and MH (black squares) halides follow similar trends: MH >> MH_3 > MH_2. This difference in bond dissociation energies, particularly for MH, suggests full dissociation may not be likely. Some un-dissociated secondary phases (i.e. MH) may remain and result in composition changes and halide incorporation. This could also result in reduced mobility for the M element if it remains bonded to one of the halide atoms.

The di-halides ($CuCl_2$ and $CuBr_2$) also have a large difference between the first and second bond dissociation energies. The mono-halides (AgCl, AgBr, AgI, CuCl, CuBr, and CuI), have relatively low

bond dissociation energy values suggesting they will contribute halides sufficiently during species transport events. Note that the MH values for the di-halides are comparable to the values for the mono-halides, as expected.

There is a consistent progression to lower energies per cation as the halide becomes larger such that M-Cl > M-Br > M-I for MH and MH_3 dissociation. The bond dissociation energies of the M-I compounds are comparable to the group I element mono-halides suggesting that these may decompose more readily than the M-Cl or M-Br compounds. Finally, larger atoms are found to segregate most strongly to crystal surfaces. Therefore, there is expected to be a driving force reducing incorporation of the halide into the CIGS for larger halide elements.

4.3.2 Standard Enthalpies of Formation

The standard enthalpies of formation for potentially stable compounds for the species under consideration are shown in Table 4.2. Note that some In(II), Ga(I), and Ga(II) compounds are known to be unstable and unlikely to form, thus are not considered [28], [29], [30], [31]. All enthalpy of formation values are exothermic meaning compound formation is favorable to some degree. Compound stability per metal generally trends M-Cl > M-Br > M-I as per the magnitude of the enthalpy of formation. The tri-halide Group III compounds have greater stability than the mono- and di-halide compounds. This high stability aids the drive for tri-halides to form.

Table 4.2 Standard enthalpies of formation in eV for possible stable M'H compounds formed during the metal halide treatment [32].

	$\Delta H_f{}^\circ$(s) [eV]		
	Cl	Br	I
Ag(I)	-1.32	-1.04	-0.640
Cu(I)	-1.42	-1.08	-0.703
Cu(II)	-2.28	-1.47	-
In(I)	-1.93	-1.82	-1.21
In(III)	-5.57	-4.45	-2.47
Ga(III)	-5.44	-4.01	-2.48

4.3.3 Vapor Pressure Evaluation

Vapor phase transport, and thus vapor pressure, may be critical to the recrystallization process. Vapor pressure dependence on temperature equations are summarized in Table 4.3 for the metal halides under consideration.

Table 4.3 Summary of metal halide compounds of interest, reported equations representing the vapor pressure dependence on temperature (in K, except $SeCl_4$ is in ˚C) in their original units, the temperature ranges the experiments were conducted over, and the respective sources.

	Reference	Equation	T_{start} / K	T_{end} / K
AgBr	[33]	ln(p/Pa) = 23.72 – 21653 / T	830	930
AgCl	[34]	log(p/mmHg) = 8.5974 - 10385.6 / T	1028	1260
AgI	[35]	log(p/bar) = 4.0634 - (6697.512 / (T - 127.973))	1093	1779
CuBr	[36]	ln(p/Pa) = 23.73 -14936 / T	529	658
CuCl	[37]	log(p/Pa) = 7.662 - 20311.1 / T	750	-
$CuCl_2$	[38]	log(p/mmHg) = 10.06 - 10119 / T	645	800
CuI	[39]	log(p/mmHg) = 8.677 – 7853 / T	-	-
InBr	[40]	ln(p/Pa) = -14521/T - 4.032ln(T) + 54.437	569	950
$InBr_3$	[41]	log(p/kPa) = 14.13 - 8230 / T	456	547
InCl	[40]	ln(p/Pa) = -13559/T - 3.953ln(T) + 53.207	528	914
$InCl_3$	[42]	log(p/kPa) = 11.49 - 7940 / T	500	650
InI	[40]	ln(p/Pa) = -15549/T - 4.052ln(T) + 54.985	646	958
InI_3	[43]	log(p/kPa) = 12.3 – 6520 / T	399	479
$GaCl_3$	[44]	log(p/Pa) = 13.80 - 3800 / T	298	308
$GaBr_3$	[45]	log(p/Pa) = 16.1 - 5250 / T	300	357
GaI_3	[44]	log (p/Pa) = -5130 / T + 14	345	401
$SeCl_4$	[46]	log(p/mmHg) = 11.204 - 3.865 / T	420	450

Equations from Table 4.3 are extrapolated to the temperature range of interest (300-550˚C) in Figure 4.4. Although some extrapolations may be somewhat inaccurate due to the large difference from the experimental temperature range we expect the general trends to hold. The vapor pressure for CuCl is very low and would require excessive temperatures to evaporate, thus, it is not shown. The vapor pressure for $SeCl_4$ is very high, implying rapid vapor phase transport, and is not shown. The Ga halide compounds have the highest vapor pressures of the compounds shown in Figure 4.4. The vapor pressures of the In halide compounds are slightly lower. They are all within approximately one order of magnitude, except for $InBr_3$ which is slightly higher. The Ag halide compounds and $CuCl_2$ have the lowest vapor pressures in this temperature range with the exceptions.

4.3.4 Melting Points

To evaluate if a liquid phase can be expected, the melting (MP) points at atmospheric pressure of compounds under consideration are shown in Table 4.4 [32]. All metal species form at least one compound with a halide that has a melting point well within treatment temperatures (under 550˚C). Many of the In, Ga, and Se halide compounds have melting points under 300˚C.

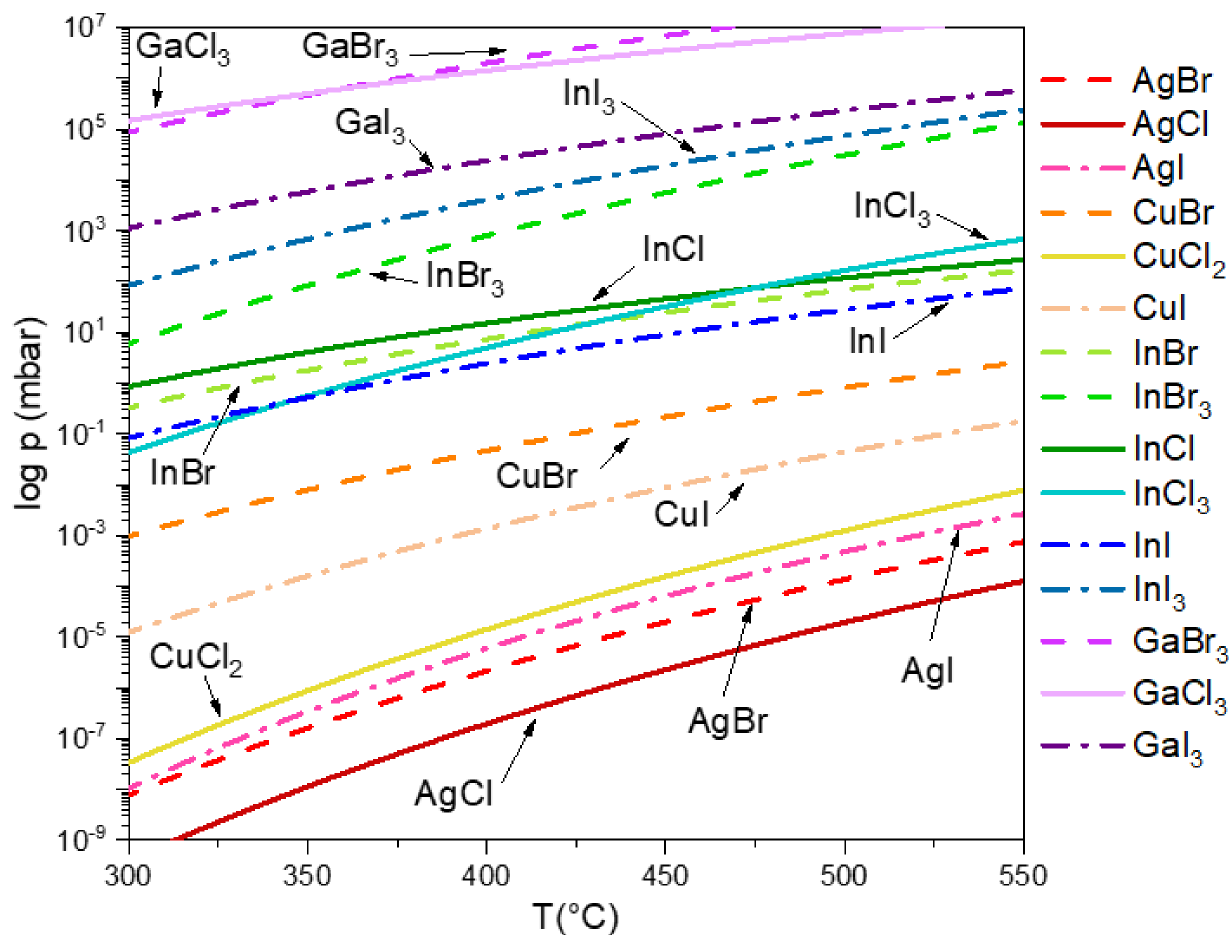

Figure 4.4 Extrapolated vapor pressure versus temperature for metal halides of interest in the temperature range of interest. Chloride compounds are plotted with solid lines, bromide compounds with dashed lines, and iodide compounds with dot-dashed lines.

Table 4.4 Melting (MP) points in ˚C at atmospheric pressure for the metal halide compounds under consideration [32].

	MP (˚C)		
	Cl	Br	I
Ag(I)	455	430	558
Cu(I)	430	497	591
Cu(II)	630	498	-
In(I)	225	285	364.4
In(III)	583	420	-
Ga(III)	77.9	123	212
Se(IV)	305	123	-

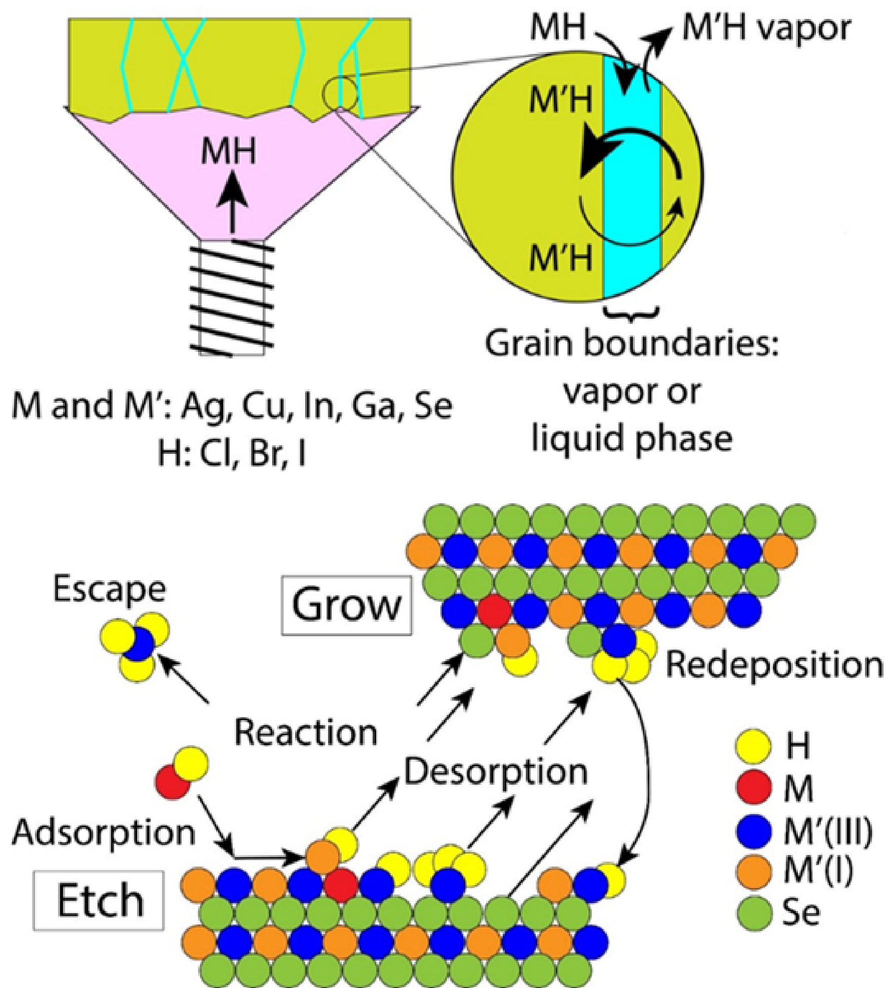

Figure 4.5 Schematic of the proposed halide-induced recrystallization and grain growth process and mechanism. A metal halide (MH) is evaporated and introduced in the vapor phase. In CIGS grain boundaries the metal halide with CIGS species (M'H) which desorb, move between grains, and re-adsorb resulting in grain growth. A schematic of vapor phase atomic transport resulting in grain growth follows.

4.4 Discussion

Figure 4.5 shows a general schematic of a proposed mechanism for metal halide induced recrystallization of CIGS. An evaporated metal halide (MH) adsorbs to a CIGS grain surface and reacts to form secondary M'H compounds. The new compounds then transport through grain boundaries in the liquid or vapor phase. These compounds must rapidly re-deposit onto another grain surface resulting in Ostwald ripening-like grain growth or else they escape from the material.

First, we consider the adsorbed MH. The MH must dissociate to free the halide for further reaction. Williams et al. investigated non-toxic halide compound replacements to $CdCl_2$ for CdTe recrystallization. They showed that compounds with lower bond dissociation energies resulted in more effectively recrystallized and higher performing CdTe, suggesting that dissociation of the transport agent may be a key property [47]. The Group I mono- and di-halides have low bond dissociation energies, suggesting that they should provide an effective halide source. The Group III mono-halides have larger bond energies, suggesting they are less suitable sources. Moreover, the bond dissociation energies also provide some insight into if the metal halide would be likely to decompose. The relative magnitudes of the bond dissociation energies of the MH_3, MH_2, and MH for the Group III tri-halides indicate the possibility of incomplete dissociation. Furthermore, the stability of the tri-halide compounds based on enthalpy of formation data (Table 4.2) suggests that complete dissociation may not be favorable. The experimental results in Section 2 show that $InBr_3$ and, more so, $InCl_3$ results in more composition variation than the CuBr. $InCl_3$ also resulted in more halide incorporation, which we generally see with M-Cl treatments, and has shown to enrich In content [21]. Each chloride compound has a higher bond dissociation energy and stability than the respective bromide and iodide compounds. This suggests the bromide and iodide compounds may be better MH sources. Additionally, for considering an in-situ treatment low-vapor pressure source materials are typically used. By this metric AgBr, AgI, CuBr, and CuI should be considered as metal halide sources. Ag alloying has been shown to result in high-efficiency devices [48], [49] and helps to recrystallize low-temperature deposited CIGS [50], proposed to be due to the lower melting temperatures of $Ag(In,Ga)Se_2$ alloys compared to $Cu(In,Ga)Se_2$ alloys [51]. With respect to the cation, a Ag-halide source may aid transport during recrystallization. Experimental results have shown that AgBr results in the best material and device quality of the metal halides tested so far [52].

Following MH dissociation, new M'H compounds may form. The exothermic enthalpy of formation data in Table 4.2 shows there is some drive for all compounds being considered to form. However, these values do not consider formation from a surface which requires cation removal from the CIGS matrix. In general, bond exchange from the CIGS to form a M'H compound is likely to have a low activation energy barrier.

For example, it is known that Cl_2 and Br_2 can be used as spontaneous etches to produce ultra-thin CIGS [53], [54], [55]. Our demonstrations of large grain size enhancement with Cl and Br compounds supports the expectation of rapid reaction with the elemental components of CIGS.

The newly formed M'H compounds may desorb from the grain surface and quickly redeposit on another grain. Atomic transport through grain boundaries requires the compounds to form a liquid or vapor phase to have sufficient mobilities. It is expected that transport occurs most commonly across (or along) grain boundaries. It has been shown that Cl diffuses through grain boundaries for the $CdCl_2$ treatment of CdTe [10], [11]. It is unlikely that a liquid M'H phase is forming to catalyze transport. Based on the MP data presented in Table 4.4, only In(I) and Ga(III) compounds are expected to form liquid phases during low-temperature (<500°C) recrystallization treatments. However, these compounds have sufficient vapor pressures (Figure 4.4) to provide gas phase transport. This is supported by the behavior of Ga. Significant Ga depletion (Table 4.1) or the smoothing of any Ga gradient [21] results from all metal halide treatments. Based on the data presented, the Ga compounds are expected to form very stable compounds, limiting re-deposition as the corresponding reaction should be slow. Additionally, Ga tri-halide volatility prevents rapid re-deposition, resulting in an etch and escape process in the vapor phase. The In compounds also have sufficient stability and lower vapor pressures to transport in the vapor phase with sufficient time to allow re-condensation on surrounding grains.

The Cu halide compounds have high MPs, low vapor pressures, and low enthalpies of formation. Compounds with low enthalpies of formation may be less likely to form or be present only as transient intermediates. We have shown low-temperature (400°C) metal halide induced recrystallization [17], [18], which is below the MPs of the Cu halide compounds. Thus, transport is likely in the vapor phase but aided by some behaviors of Cu in CIGS. Cu is known to be highly mobile in CIGS and induce recrystallization during growth by enhancing grain boundary mobility [15]. A Cu-rich growth stage induces recrystallization and grain growth even at low deposition temperatures (420°C) by diffusion-induced grain boundary migration [56]. Additionally, a liquid $Cu_{2-x}Se$ phase is proposed to form in grain boundaries for high temperature deposition processes and enhance transport [57], [58]. Note that $SeCl_4$ may form and escape from the film due to its very high vapor pressure. A Se overpressure during treatment has been shown to compensate for this.

4.5 Conclusion

Based on a bond dissociation energies evaluation, AgBr, AgI, CuBr, and CuI metal halide sources are recommended. Known benefits of Ag alloying of CIGS particularly for recrystallization suggests that AgBr and AgI are optimal metal halide sources. Atomic transport in the vapor phase resulting in grain growth

and recrystallization is most likely. Vapor pressure appears to be a useful tool to predict how well CIGS constituents transport during treatment. Ga tri-halides have very high vapor pressures and stability resulting in slow re-deposition thus etching and removal from the film. Although the I-based compounds have not been tested this evaluation suggests they may be sufficient transport agents for CIGS recrystallization and grain growth. The vapor pressure of GaI_3 is lower than that of $GaBr_3$ and $GaCl_3$ which may further reduce Ga etching. The vapor pressures of the Cu halide compounds are low, however, Cu is very mobile in CIGS and has been shown not to be limiting in this treatment.

4.6 Acknowledgements

This material is based upon work supported by the U.S. Department of Energy's Office of Energy Efficiency and Renewable Energy (EERE) under Solar Energy Technologies Office (SETO) Award Number DE-EE0007551.

4.7 Appendix A

CIGS films were deposited by single-stage co-evaporation onto molybdenum-coated soda-lime glass at a substrate temperature of 350°C and tested in the presence of $InBr_3$, CuBr, and $InCl_3$. High-throughput annealing chambers were fabricated to contain the metal halide and a CIGS sample. In a N_2-purged glovebox the CIGS sample and metal halide were loaded into a MACOR crucible with a press-fit lid then sealed between two stainless steel flanges. The annealing chamber was placed into a box furnace and annealed at 450°C for one hour then removed to cool in air. Changes to film morphology were studied by scanning electron microscopy (SEM) using a FEI Helios Nanolab 600i FIB-SEM. Energy dispersive spectroscopy (EDS) was used to analyze film compositions with a 10 kV electron beam using an EDAX Octane Super SDD detector in the FIB-SEM system. X-ray diffraction (XRD) patterns were collected using a PANalytical PW3040 X-Ray Diffractometer and phases were identified using the International Center for Diffraction Data (ICDD) Database [22].

4.8 References

[1] M. Kim, S. Sohn, and S. Lee, "Reaction kinetics of CdTe thin films during $CdCl_2$ heat treatments", Solar Energy Materials and Solar Cells, 95, 2295-2301, 2011. DOI: 10.1016/j.solmat.2011.03.044.

[2] B.E. McCandless and R.W. Birkmire, "Analysis of post deposition processing for CdTe/CdS thin film solar cells", Solar Cells, 31, 527-535, 1991. DOI: 10.1016/0379-6787(91)90095-7.

[3] B.E. McCandless, H. Hichri, G. Hanket, and R.W. Birkmire, "Vapor phase treatment of CdTe/CdS thin films with $CdCl_2$:O_2", Conference Record of the IEEE Photovoltaic Specialists Conference, 1996. DOI: 10.1109/PVSC.1996.564244.

[4] N. Nakayama, H. Matsumoto, K. Yamaguchi, S. Ikegami, and Y. Hioki, “Ceramic Thin Film CdTe Cell”, Japan Journal of Applied Physics, 15, 2281-2282, 1976. DOI: 10.1143/JJAP.15.2281.

[5] J.T. Moon, K.C. Park, and H.B. Im, “Photovoltaic Properties of CdS/CdTe Solar Cells Sintered with $CdCl_2$”, Solar Energy Materials, 18, 53-60, 1988. DOI: 10.1016/0165-1633(88)90044-5.

[6] J.S. Roh and H.B. Im, “Effects of $CdCl_2$ in CdTe on the properties of sintered CdS/CdTe solar cells”, Journal of Materials Science, 23, 2267-2272, 1988. DOI: 10.1007/BF01115799.

[7] B. McCandless, L. Moulton, and R. Birkmire, “Recrystallization and sulfur diffusion in $CdCl_2$-treated CdTe/CdS thin films”, Progress in Photovoltaics: Research and Applications, 5, 249-260, 1997. DOI: 10.1002/(SICI)1099-159X(199707/08)5:4<249::AID-PIP178>3.0.CO;2-S.

[8] B. McCandless, I. Youm, and R. Birkmire, “Optimization of vapor post-deposition processing for evaporated CdS/CdTe solar cells”, Progress in Photovoltaics: Research and Applications, 7, 21-30, 1999. DOI: 10.1002/(SICI)1099-159X(199901/02)7:1<21::AID-PIP244>3.0.CO;2-D.

[9] T. Zhou, N. Reiter, R. Powell, R. Sasala, and P. Meyers, “Vapor chloride treatment of polycrystalline CdTe/CdS films”, Conference Record of the IEEE Photovoltaic Specialists Conference, 1994. DOI: 10.1109/wcpec.1994.519818.

[10] M. Terheggen, H. Heinrich, G. Kostorz, A. Romeo, D. Baetzner, A.N. Tiwari, A. Bosio, and N. Romeo, “Structural and chemical interface characterization of CdTe solar cells by transmission electron microscopy”, Thin Solid Films, 431, 262-266, 2003. DOI: 10.1016/S0040-6090(03)00268-2.

[11] M. Terheggen, H. Heinrich, G. Kostrorz, D. Baetzner, A. Romeo, and A.N. Tiwari, “Analysis of Bulk and Interface Phenomena in CdTe/CdS Thin-Film Solar Cells”, Interface Science, 12, 259-266, 2004. DOI: 10.1023/B:INTS.0000028655.11608.c7.

[12] J. R. Winger and M. A. Scarpulla, “Grain Growth in CdTe Films During $CdCl_2$ Treatment: $TeCl_4$ Theory”, 2019 IEEE 46th Photovoltaic Specialists Conference (PVSC), 1834-1838, 2019. DOI: 10.1109/PVSC40753.2019.8980923.

[13] A.M. Gabor, J.R. Tuttle, D.S. Albin, M.A. Contreras, R. Noufi, and A.M. Hermann, “High-efficiency $CuIn_xGa_{1-x}Se_2$ solar cells made from $(In_xGa_{1-x})_2Se_3$ precursor films”, Appl. Phys. Lett., 65, 198, 1994. DOI: 10.1063/1.112670.

[14] J. Kessler, C. Chityuttakan, J. Lu, J. Schöldström, and L. Stolt, “$Cu(In,Ga)Se_2$ Thin Films Grown with a Cu-Poor/Rich/Poor Sequence: Growth Model and Structural Considerations”, Progress in Photovoltaics: Research and Applications, 11, 319-331, 2003. DOI: 10.1002/pip.495.

[15] N. Barreau, T. Panchaud, F. Couzinié-Devy, L. Arzel, and J. Kessler, “Recrystallization of CIGSe layers grown by three-step processes: A model based on grain boundary migration”, Acta Materialia, 58, 5572-5577, 2010. DOI: 10.1016/j.actamat.2010.06.025.

[16] G. Rajan, B. Belfore, S. Karki, D. Poudel, H. Kahoui, N. Lanham, E. Palmiotti, S. Soltanmohammad, A. Rockett, and S. Marsillac, “Impact of Post-Deposition Recrystallization by Alkali Fluorides on Cu(In,Ga)Se_2 Thin-Film Materials and Solar Cells”, Thin Solid Films, 690, 2019. DOI: 10.1016/j.tsf.2019.137526.

[17] E. Palmiotti, S. Soltanmohammad, A. Rockett, G. Rajan, S. Karki, B. Belfore, and S. Marsillac, “Post-Deposition Recrystallization of Chloride Treated Cu(In,Ga) Se_2 Thin-Film Solar Cells”, 2018 IEEE 7th World Conference on Photovoltaic Energy Conversion (WCPEC) (A Joint Conference of 45th IEEE PVSC, 28th PVSEC & 34th EU PVSEC), 163-166, 2018, DOI: 10.1109/PVSC.2018.8547595.

[18] E. Palmiotti, S. Karki, B. Belfore, S. Soltanmohammad, G. Rajan, S. Marsillac, and A. Rockett, “Post-Deposition Recrystallization of Co-Evaporated Cu(In,Ga)Se_2 Films by Bromide Vapor Treatments”, 2019 IEEE 46th Photovoltaic Specialists Conference (PVSC), 1863-1866, 2019, DOI: 10.1109/PVSC40753.2019.8980803.

[19] D. Poudel, B. Belfore, T. Ashrafee, E. Palmiotti, S. Karki, G. Rajan, T. Lepetit, A. Rockett, and S. Marsillac, “In Situ Recrystallization of Co-Evaporated Cu(In,Ga)Se_2 Thin Films by Copper Chloride Vapor Treatment towards Solar Cell Applications”, Energies, 14, 3938, 2021, DOI: 10.3390/en14133938.

[20] D. Poudel, B. Belfore, T. Ashrafee, S. Karki, G. Rajan, A. Rockett, and S. Marsillac, “Analysis of Post-Deposition Recrystallization Processing via Indium Bromide of Cu(In,Ga)Se_2 Thin Films”, Materials, 14, 3596, 2021, DOI: 10.3390/ma14133596.

[21] B. Belfore, D. Poudel, S. Karki, S. Soltanmohammad, E. Palmiotti, T. Lepetit, A. Rockett, and S. Marsillac, “Recrystallization of Cu(In,Ga)Se_2 Semiconductor Thin Films via $InCl_3$ Treatment”, Thin Solid Films, 735, 2021. DOI: 10.1016/j.tsf.2021.138897.

[22] S. Gates-Rector and T. Blanton. The Powder Diffraction File: A Quality Materials Characterization Database. Powder Diffr., (2019).

[23] E. Don, R. Hill, and G. Russell, “The structure of $CuInSe_2$ films formed by co-evaporation of the elements”, Solar Cells, 16, 131-142, 1986. DOI: 10.1016/0379-6787(86)90079-7.

[24] T. Yamaguchi, J. Matsufusa, and A. Yoshida, “Structural properties of $CuIn_xGa_{1-x}Se_2$ thin films prepared by rf sputtering”, Journal of Applied Physics, 72, 5657-5662, 1992. DOI: 10.1063/1.351966.

[25] K. Ramakrishna Reddy and R. Chalapathy, “Structural properties of $CuGa_xIn_{1-x}Se_2$ thin films deposited by spray pyrolysis”, Crystal Research and Technology, 34, 127-132, 1999. DOI: 10.1002/(SICI)1521-4079(199901)34:1<127::AID-CRAT127>3.0.CO;2-5.

[26] Y. Luo. Comprehensive Handbook of Chemical Bond Energies, [Print], 2007. DOI: 10.1201/9781420007282.

[27] N. Sadeghi, I. Hikmet, I. Colomb, and D.W. Setser, "State-to state dynamics for the reactions of metastable Cu atoms with F_2, Cl_2, and Br_2", Gas-Phase Metal Reactions, Elsevier Science Publishers B.V., 1992. DOI: 10.1016/B978-0-444-89070-2.50021-9.

[28] F. Defoort, C. Chatillon, and C. Bernard, "Mass-spectrometric study of (indium+chlorine)(g) Enthalpies of formation of InCl(g), In_2Cl_2(g), In_2Cl_4(g), $InCl_3$(g), and In_2Cl_6(g)", J. Chem. Thermodynamics, 20, 1443-1456. 1988. DOI: 10.1016/0021-9614(88)90039-0.

[29] Y. Kuniya, S. Hosoda, and M. Hosaka, "Studies on the Vapor Phase Reaction in the System In-Cl_2", Denki Kagaku, 74, 20-25, 1982.

[30] Y. Kuniya and M. Hosaka, "Vapor Phase Equilibria in the Systems In-$InCl_3$ and Ga-$GaCl_3$", Journal of Crystal Growth, 28, 385-391, 1975. DOI: 10.1016/0022-0248(75)90077-9.

[31] Y. Kuniya, M. Hosaka, and I. Shindo, "Studies on the Vapor Phase Reaction in the System Ga-Cl_2", Denki Kagaku, 7, 372-378, 1975.

[32] CRC Handbook of Chemistry and Physics [Online]. Electronic ed. Boca Raton, Fla: CRC Press, 1978. Print.

[33] T. Nagata, A. Iizuka, and E. Shibata, "Vapor pressure measurements of AgBr by the Knudsen effusion method", Thermochimica Acta, 671, 32-35, 2019. DOI: 10.1016/j.tca.2018.10.027.

[34] H. Bloom, J.O'M. Bockris, N.E. Richards, and R.G. Taylor, "Vapor Pressure and Heat of Vaporization of Some Simple Molten Electrolytes", Journal of the American Chemical Society, 80, 2044-2046, 1958. DOI: 10.1021/ja01542a004.

[35] D. Stull, "Vapor Pressure of Pure Substances. Organic and Inorganic Compounds", Ind. Eng. Chem., 39, 517-540, 1947. DOI: 10.1021/ie50448a022.

[36] A. Iizuka, E. Shibata, M. Sato, N. Onodera, and T. Nakamura, "Vapor pressure measurements of CuBr and $ZnBr_2$ by the Knudsen effusion method and their vapor species identification", Thermochimica Acta, 593, 1-6, 2014. DOI: 10.1016/j.tca.2014.08.003.

[37] D.F. Brestanovsky, B.N. Baron, R.E. Rocheleau, and T.W.F. Russell, "Analysis of the rate of vaporization of CuCl for solar cell fabrication", Journal of Vacuum Science & Technology A, 28, 28-33, 1982. https:// doi.org/10.1116/1.4986944.

[38] T. Kekesi, K. Mimura, and M. Isshiki, "Copper Extraction from Chloride Solutions by Evaporation and Reduction with Hydrogen", Materials Transactions, JIM, 36, 649-658, 1995.

[39] R. Shelton, "Vapour pressures of the solid copper (i) halides", Trans. Faraday Soc., 57, 2113-2118, 1961. DOI: 10.1039/TF9615702113.

[40] T. Brumleve, S. Mucklejohn, and N. O'Brien, "The preparation and vapour pressures of the indium(I) halides and the standard molar Gibbs free energy change for formation of InX from In(g) and

X_2(g), (X = Cl, Br, or I)", The Journal of Chemical Thermodynamics, 21, 11, 1193-1206, 1989. DOI: 10.1016/0021-9614(89)90106-7.

[41] B. Brunetti, C. Palchetti, and V. Piacente, "Sublimation enthalpy of indium tri-bromide", Journal of Materials Science Letters, 6, 1395-1397, 1997.

[42] B. Brunetti, V. Piacente, and P. Scardala, "Torsion Study on the Sublimation Process of $InCl_3$", Journal of Chemical and Engineering Data, 43, 101-104, 1998. DOI: 10.1021/je970188a.

[43] B. Brunetti, A. Giustini, and V. Piacente, "Vapour pressures and sublimation enthalpy of solid indium(III) iodide", Journal of Chemical Thermodynamics, 29, 2, 239-246, 1997. DOI: 10.1006/jcht.1996.0156.

[44] B. Brunetti, V. Piacente, and P. Scardala, "Vapor Pressures of Gallium Trifluoride, Trichloride, and Triiodide and Their Standard Sublimation Enthalpies", Journal of Chemical and Engineering Data, 55, 98-102, 2010. DOI: 10.1021/je900276q.

[45] B. Brunetti, V. Piacente, and P. Scardala, "A Study on the Sublimation of Gallium Tribromide", Journal of Chemical and Engineering Data, 54, 2273-2276, 2009. DOI: 10.1021/je900182h.

[46] D.M. Yost and C.E. Kircher. The Vapor Pressures of Selenium Tetrachloride. The Existence of Selenium Dichloride, J. Am. Chem. Soc., 52, 4680-4685, 1930.

[47] B.L. Williams, J.D. Major, L. Bowen, W. Keuning, M. Creatore, and K. Durose, "A Comparative Study of the Effects of Nontoxic Chloride Treatments on CdTe Solar Cell Microstructure and Stoichiometry", Advanced Energy Materials, 5, 2015. DOI: 10.1002/aenm.201500554.

[48] M. Edoff, T. Jamar, N. Nilsson, E. Wallin, D. Högström, O. Stolt, O. Lundberg, W. Shafarman, and L. Stolt, "High V_{oc} in (Cu,Ag)(In,Ga)Se_2 Solar Cells", IEEE Journal of Photovoltaics, 7, 6, 2017. DOI: 10.1109/JPHOTOV.2017.2756058.

[49] M. Green, N. Kopidakis, E. Dunlop, and A. Baillie, "Solar cell efficiency tables (Version 55)", Progress in Photovoltaics, 2, 3-15, 2020. DOI: 10.1002/pip.3228.

[50] K. Kim, J.W. Park, J.S. Yoo, J. Cho, H. Lee, and J.H. Yun, "Ag incorporation in low-temperature grown Cu(In,Ga)Se_2 solar cells using Ag precursor layers", Solar Energy Materials & Solar Cells, 146, 114-120, 2016. DOI: 10.1016/j.solmat.2015.11.028.

[51] J.L. Shay and J.H. Wernick, Ternary Chalcopyrite Semiconductors: Growth, Electronic Properties, and Applications, Pergamon Press, [Print], 1975.

[52] B. Belfore, D. Poudel, T. Lepetit, E. Palmiotti, T. Ashrafee, A. Rockett, N. Barreau, and S. Marsillac, "Low-temperature, high-rate deposition of Cu(In,Ga)Se_2 by recrystallization catalyzed by AgBr". (Unpublished results).

[53] R. Birkmire and B. McCandless, “Specular $CuInSe_2$ films for solar cells”, Appl. Phys. Lett., 53, 28-30, 1988.

[54] M. Bouttemy, P. Tran-Van, I. Gerard, T. Hildebrandt, A. Causier, J.L. Pelouard, G. Dagher, Z. Jehl, N. Naghavi, G. Voorwinden, B. Dimmler, M. Powalla, J.F. Guillemoles, D. Lincot, and A. Etcheberry, “Thinning of CIGS solar cells: Part I: Chemical processing in acidic bromine solutions”, Thin Solid Films, 519, 7207-7211, 2011. DOI: 10.1016/j.tsf.2010.12.219.

[55] K. Miyazaki, O. Matsushima, M. Moriwake, H. Takasu, S. Ishizuka, K. Sakurai, A. Yamada, and S. Niki, “High sensitivity and wide bandwidth image sensor using $CuIn_{1-x}Ga_xSe_2$ thin films”, Thin Solid Films, 517, 2392-2394, 2009. DOI: 10.1016/j.tsf.2008.11.029.

[56] H. Stange, S. Brunken, D. Greiner, M. Heinemann, C.A. Kaufmann, S.S. Schmidt, J. Backer, M. Klaus, C. Genzel, and R. Mainz, “Diffusion-induced grain boundary migration as mechanism for grain growth and defect annihilation in chalcopyrite thin films”, Acta Materialia, 111, 377-384, 2016. DOI: 10.1016/j.actamat.2016.03.073.

[57] R. Klenk, T. Walter, H. Schock, and D. Cahen, “A Model for the Successful Growth of Polycrystalline Films of $CuInSe_2$by Multisource Physical Vacuum Evaporation”, Advanced Materials, 5, 114-119, 1993.

[58] R. Noufi, Y. Yan, J. Abu-Shama, K. Jones, M. Al-Jassim, B. Keyes, J. Alleman, and K. Ramanathan, “Investigation of the microstructure of $Cu(In,Ga)Se_2$ thin films used in high-efficiency devices”, Conference Record of the IEEE Photovoltaic Specialists Conference, 508-510, 2002. DOI: 10.1109/pvsc.2002.1190613.

4.9 Thesis Author Contributions

The thesis author was responsible for the following in this study: conceptualization, data collection, formal analysis, visualization, and writing. Co-authors assisted by supplying as-deposited CIGS films (Section 4.2.2) and helping with writing and editing.

CHAPTER 5

IN-SITU STUDY OF THE CRYSTALLIZATION OF AMORPHOUS $CuInSe_2$ THIN FILMS AND THE EFFECT OF $InCl_3$ TREATMENT

Paper submitted to *Thin Solid Films*

Elizabeth Palmiotti[a*], Benjamin Belfore[b], Deewakar Poudel[b], Sylvain Marsillac[b], Angus Rockett[a]

[a] Colorado School of Mines, Golden, CO 80401 U.S.A.

[b] Old Dominion University, Norfolk, VA 23529 U.S.A.

5.1 Abstract

Amorphous $CuInSe_2$ films were deposited by rf-magnetron sputtering onto soda-lime glass and silicon substrates. Some were treated with an $InCl_3$ solution. The films were annealed in a nitrogen environment and studied using in-situ high-temperature x-ray diffraction. $CuInSe_2$ recrystallization began at ∼270°C and all samples showed increasing crystallinity up to ∼380°C. The onset and completion temperatures for crystallization varied minimally between samples. The as-deposited films (no $InCl_3$) showed CuSe phase formation at intermediate temperatures (180-250°C). Na_2O from the soda-lime glass increased net rate of crystallization. $InCl_3$ resulted in an even greater increase to crystallization rate and largely improved the final crystalline quality.

5.2 Introduction

Thin-film photovoltaics offer promise as a low-cost, high-efficiency technology. However, some have a limited commercial presence due to higher manufacturing costs, especially due to expensive, low-throughput capital equipment. Cadmium telluride (CdTe) has the largest market presence of any thin-film due to a high-rate deposition process followed by a rapid $CdCl_2$ activation treatment, resulting in improved grain size, crystallization, defect passivation, and enhanced device performance [1], [2], [3], [4]. Combined, this results in a very fast process that keeps down the capital equipment cost per module, and

has allowed CdTe modules to drive the overall cost of photovoltaics down dramatically. Though efficient [5], $CuIn_{(1-x)}Ga_xSe_2$ (CIGS) devices are commercially limited due to typically slow, high-temperature deposition processes. In our previous work we showed that CIGS films co-evaporated at 350°C and 400°C were recrystallized using metal chloride and bromide post-deposition vapor treatments [6], [7]. Although the treatments resulted in large grains and improved crystallinity, notable variations to composition and, in most conditions, elimination of the Ga gradient through the film or almost complete loss of Ga resulted. In the results reported here, $CuInSe_2$ (CIS) films were studied to simplify interpretation by avoiding Ga removal by the halide. We present a study of the kinetics of as-deposited and $InCl_3$-enhanced crystallization of amorphous $CuInSe_2$ (CIS) films using high-temperature x-ray diffraction (HT-XRD).

5.3 Experimental Details

1 µm thick amorphous CIS films were deposited at room temperature by radio-frequency (rf)-magnetron sputtering from a single, 76 mm diameter 99.9% purity CIS target onto soda-lime glass (SLG) and silicon substrates 16.5 cm away. The system was brought to a base pressure of 3.2 mPa and sputtering was conducted in ultra-high purity Ar at 0.25 Pa and 70 W rf power. The as-deposited film composition was 26.9 at% Cu, 22.0 at% In, and 51.1 at% Se.

An Anton Paar DHS-1100 heater stage was installed onto a Malvern Panalytical Empyrean x-ray diffractometer with a Mo x-ray source ($\lambda_{K\alpha} = 0.0711nm$). A polyether ether ketone (PEEK) dome continuously purged with flowing high-purity nitrogen contained the sample on the heater stage. For each heating profile, the temperature was initially increased to 150°C, stabilized, then a scan was collected. The stage temperature was increased by 10°C at a rate of 60°C per minute, held for one minute, and another scan collected. This was repeated until the stage temperature reached 450°C. Each scan typically took 4.5 minutes.

$InCl_3$ solution treated samples were also studied. A 0.1 M $InCl_3$ solution was prepared in methanol. Similar to what is done for the solution $CdCl_2$ treatment of CdTe [8], two drops were placed on the film surfaces, covering the entire surface, and then annealed in an ultra-high purity Ar-purged tube furnace at 55°C for ten minutes to evaporate the methanol. Samples were removed from the tube furnace into laboratory air, immediately transported in a press-fit sample holder, and mounted on the HT-XRD stage. The PEEK dome was immediately installed over the sample and purged with high purity N_2. For surface morphology characterization, after the $InCl_3$ solution was placed on the film surface, the sample was annealed at 55°C for ten minutes then the furnace temperature increased to the desired annealing temperature and held for 10 minutes.

XRD patterns were analyzed and peak parameters extracted using the HighScore Plus software and phases were identified using the International Center for Diffraction Data (ICDD) database [9]. Scanning electron microscopy (SEM) and energy dispersive spectroscopy (EDS) were conducted using a FEI Helios Nanolab 600i FIB-SEM at an accelerating voltage of 10 kV.

5.4 Results and Discussion

5.4.1 Ex-Situ Annealing Investigation

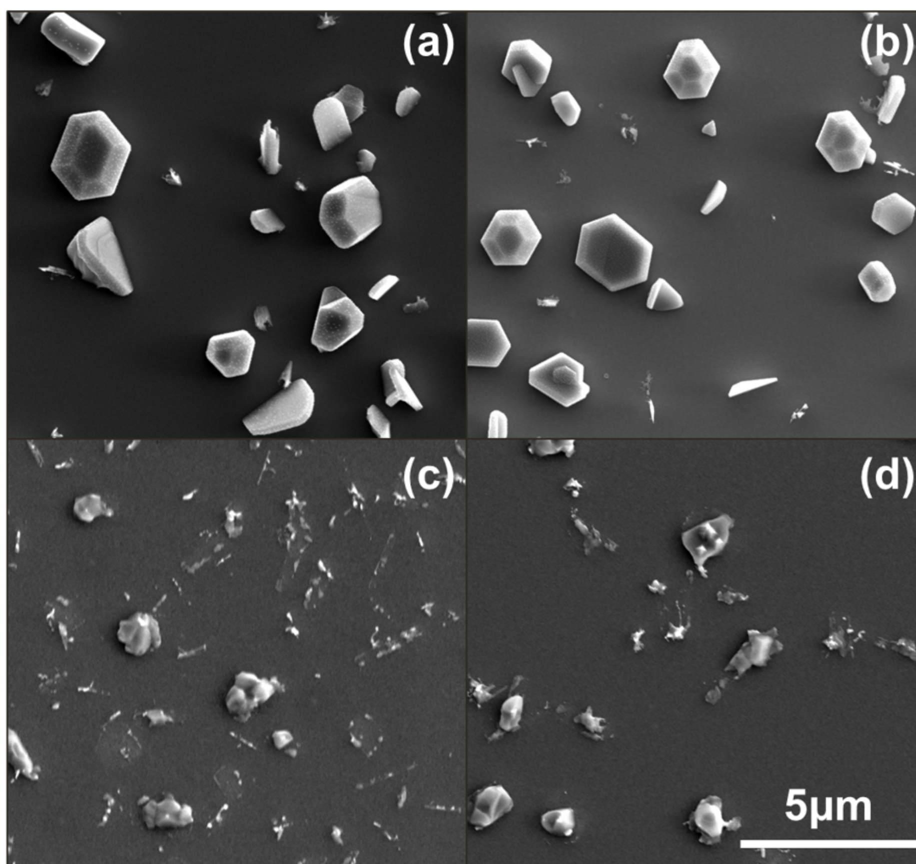

Figure 5.1 Top-view SEM micrographs of (a) CIS/Si and (b) CIS/SLG after a five minute anneal at 250°C and of (c) CIS/Si and (d) CIS/SLG after a five minute anneal at 400°C.

Figure 5.1 shows top-view SEM micrographs of (a) CIS/Si and (b) CIS/SLG annealed at 250°C for 5 minutes each, and (c) CIS/Si and (d) CIS/SLG annealed at 400°C for 5 minutes each in an Ar-purged tube furnace. The samples annealed at 250°C show large hexagonal platelets, identified as CuSe by EDS, on the surface. CuSe platelets have been previously seen in this temperature range during the annealing of electrodeposited [10] and sputtered [11] CIS films. The samples annealed at 400°C show small particles on the surface that have identical compositions to the CIS film. The compositions of the film before and after

annealing were analyzed by EDS and are compiled in Table 5.1.

Table 5.1 Compositions (at%) of CIS samples after all treatment conditions with and without $InCl_3$.

At (%)	RT		250°C		400°C	
	As-Deposited		CIS/SLG	CIS/Si	CIS/SLG	CIS/Si
Cu	26.9		21.3	22.2	28.9	32.2
In	22.0		27.0	26.8	27.5	25.6
Se	51.1		50.0	49.4	40.5	39.2
O			1.8	1.6	3.1	3.0
$InCl_3$ Solution Treatments						
	350°C		400°C		450°C	
	CIS/SLG	CIS/Si	CIS/SLG	CIS/Si	CIS/SLG	CIS/Si
Cu	27.1	26.3	27.7	26.2	22.4	28.6
In	18.7	18.4	22.6	25.3	20.8	21.5
Se	37.6	21.9	36.9	37.6	36.3	31.2
O	16.2	21.7	10.8	6.7	19.7	15.6
Cl	0.2	11.7	2.1	4.2	0.8	3.0

TOF-SIMS analysis was conducted and revealed Na diffusion from the substrate into the films after annealing. Na is commonly observed in our SIMS measurements of CIS on soda-lime glass at levels that typically scale with grain boundary volume. It is important to note that Na in soda-lime glass is present as Na_2O and some oxygen is typically found in the films as a result, although the two concentrations do not strongly correlate indicating that oxygen mostly escapes from the sample surface.

To demonstrate the morphological evolution resulting from the $InCl_3$ solution treatments, an InCl3 solution treatment was conducted on CIS/Si and CIS/SLG samples then annealed at 350, 400, and 450°C for 10 minutes each in an Ar-purged tube furnace. The resulting SEM micrographs are shown in Figure 5.2 and composition results in Table 5.1. Large (>0.5 micron) grains formed after $InCl_3$ treatments at all three temperatures. With increasing annealing temperature, the grains are less closely packed. These results differ greatly from the films annealed without $InCl_3$, as shown in Figure 5.1, which do not show observable grains at similar temperatures even though the films in Figure 5.2 began as identical amorphous, featureless films. The $InCl_3$ apparently acts as a transport agent to promote accelerated crystallization and grain growth of the material. Cl and O were detected by EDS in all films after treatment as noted in Table I and are discussed in the following section.

The composition of the film changed with increasing temperature, with and without $InCl_3$ solution treatment. Loss of Se was due to the high vapor pressure of Se in the given experimental conditions. An in-situ treatment procedure has been developed to better control and rectify composition after the introduction of $InCl_3$ [12].

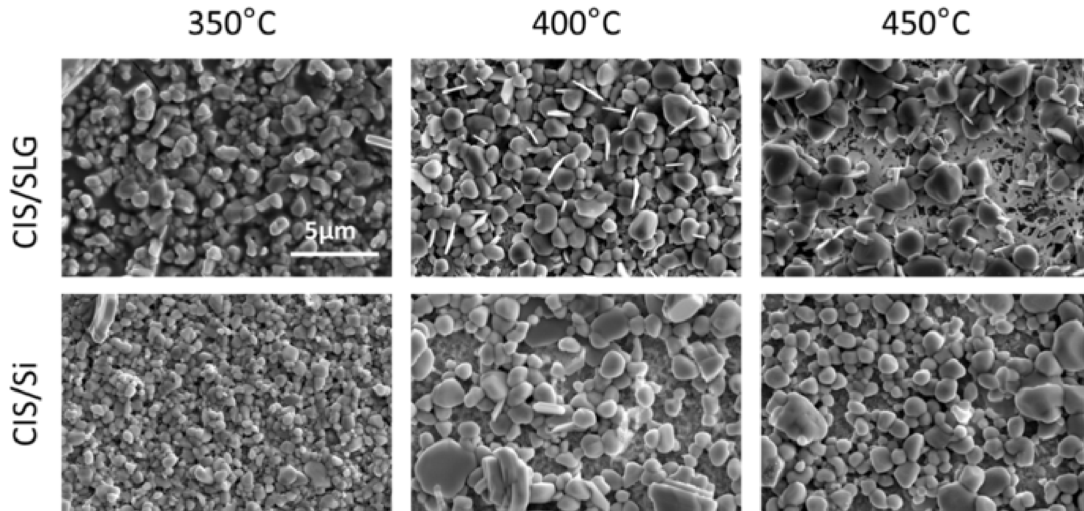

Figure 5.2 Top-view SEM micrographs of CIS/Si and CIS/SLG films after the $InCl_3$ solution treatments conducted at 350, 400, and 450°C.

5.4.2 In-Situ Kinetic Investigation

Figure 5.3 shows the HT-XRD patterns collected for (a) CIS/Si, (b) CIS/SLG, (c) $InCl_3$ treated CIS/Si, and (d) $InCl_3$ treated CIS/SLG from 150 to 450°C. All samples are amorphous at 150°C, as shown by the broad peak between 10 and 15° for the films on Si, corresponding to the average nearest neighbor spacing of CIS. The films on glass also show a broad peak between 9 and 19° due to the glass substrate, which obscures the amorphous CIS peak. With increasing temperature, the peaks corresponding to the (112), (220/204), and (312/116) plane spacings of $CuInSe_2$ (ICDD Ref. 01-081-1936) at 2θ values 12.19, 19.97, and 23.46°, respectively, appear, sharpen, and increase in intensity. The characteristic peak intensities settle at a near constant value above 380°C for all samples.

As seen in Figure 5.3(a) and Figure 5.3(b) for the as-deposited films (no $InCl_3$ treatment), an intermediate CuSe (ICDD Ref. 00-049-1456) phase causes a peak at a 2θ value of 14.2°. The CuSe phase separated and formed the platelets on the film surfaces in Figure 5.1(a) and Figure 5.1(b). This phase begins to form at approximately 180°C for both CIS/SLG and CIS/Si, and rapidly grows to a maximum intensity at 240°C. CuSe crystallizes nearly twice as quickly for CIS/SLG compared to CIS/Si based on a comparison of the rate of peak intensity increase over the temperature range of crystallization. Above 240°C the phase is unstable and fully redissolves into the film by 300°C for both samples and only the CIS phase remains. Ouyang et al. showed that a similar phase formation then decomposition occurs for sputtered CIGS films [11]. For CIS/SLG and CIS/Si the increase and sharpening of the characteristic CIS peaks shows that the material is crystallizing and forming small grains not visible by SEM (Figure 5.1).

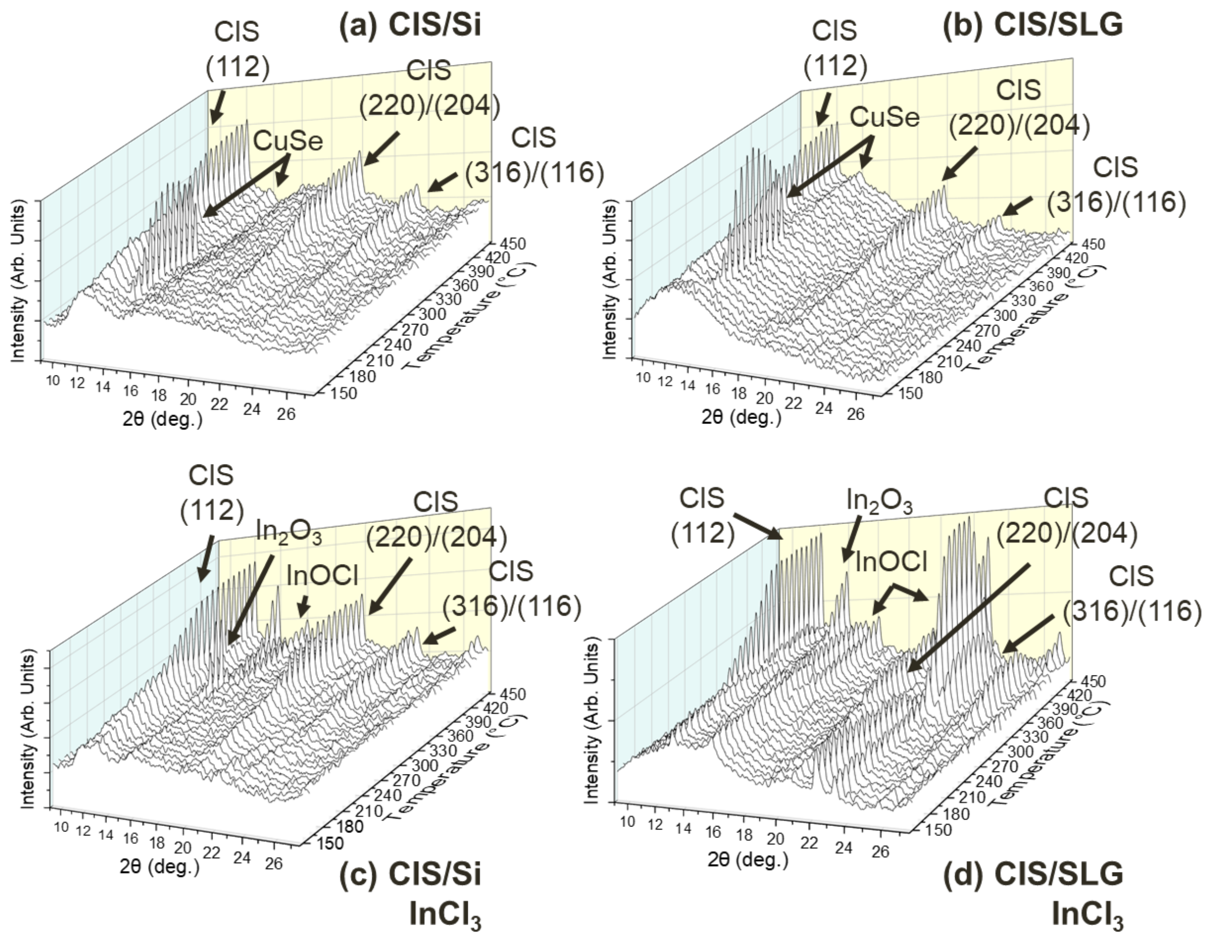

Figure 5.3 In-situ HT-XRD patterns collected from 150 to 450°C of 1 μm thick CIS films on SLG and Si substrates with and without $InCl_3$ solution treatments. Unidentified peaks are parts of the identified phases.

The $InCl_3$ solution-treated samples showed similar amorphous CIS peaks until crystallization began at approximately 270°C. Above this temperature the CIS peak intensities rapidly increased due to crystallization until 380°C, then stopped increasing. Note that no intermediate CuSe phase formed with the $InCl_3$ treatment. Probably due to the hygroscopic nature of $InCl_3$ some indium oxide and indium oxy-chloride peaks also appeared. This accounts for the relative increase of In and presence of O and Cl in the EDS results (Table 5.1). These oxide phases were not observed for the samples without $InCl_3$ treatment. Although all annealing procedures were conducted in inert environments, the samples were exposed to air during loading into the HT-XRD system and the $InCl_3$ on the surface likely absorbed oxygen. However, the CIS crystallization trends for these samples behaved as expected and the oxide was concluded not to have impacted the crystallization kinetic data, described below.

Raw peak height values, in counts, and a five-point moving average of full-width at half maximum (FWHM) values for the (112) orientation were plotted versus temperature for CIS/Si (black squares), CIS/SLG (blue triangles), $InCl_3$ treated CIS/Si (red circles), and $InCl_3$ treated CIS/SLG (green downward triangles) (Figure 5.4(a) and Figure 5.4(b), respectively). Although data was collected starting at 150°C, data was plotted and analyzed starting at 230°C, which was the first temperature where a reliable (112) peak could be distinguished due to the amorphous nature of the low-temperature range. Diffraction of the amorphous phase is not relevant to the crystallization analysis.

All curves show a minimal change in the CIS peaks up to approximately 270°C. From approximately 270°C to 380°C peak height increases rapidly for all samples and represents when crystallization is occurring. Above 380°C, no further increase in intensity was observed, suggesting that crystallization was complete, although grains may have continued to evolve without further changes in crystallinity observable by XRD (cf. Figure 5.2). Peak height and FWHM indicate the regularity of composition and structure in the film, including any crystalline defects. A sharp, high-intensity peak indicates a highly uniform and well organized crystal free of most defects while a broad, low-intensity peak indicates poor order. Peak height and sharpening were increased for the samples deposited onto SLG and even greater for both $InCl_3$ treated samples suggesting the treatment results in higher crystalline quality. It appears that these samples reach the better crystalline state at a higher rate as well, which shows that both act to accelerate the crystallization process.

The improved crystallinity for samples deposited on SLG is possibly due to the influence of Na_2O diffusing from the SLG during annealing, which is known to influence the crystallinity of CIS [13], [14]. At temperatures as low as 157°C, Na is known to diffuse through CIGS by Type C grain boundary diffusion and then by Type C grain boundary and bulk diffusion approaching 323°C [15]. This explains that with greater annealing temperatures, more Na diffuses from the SLG substrate into the CIS. Improved

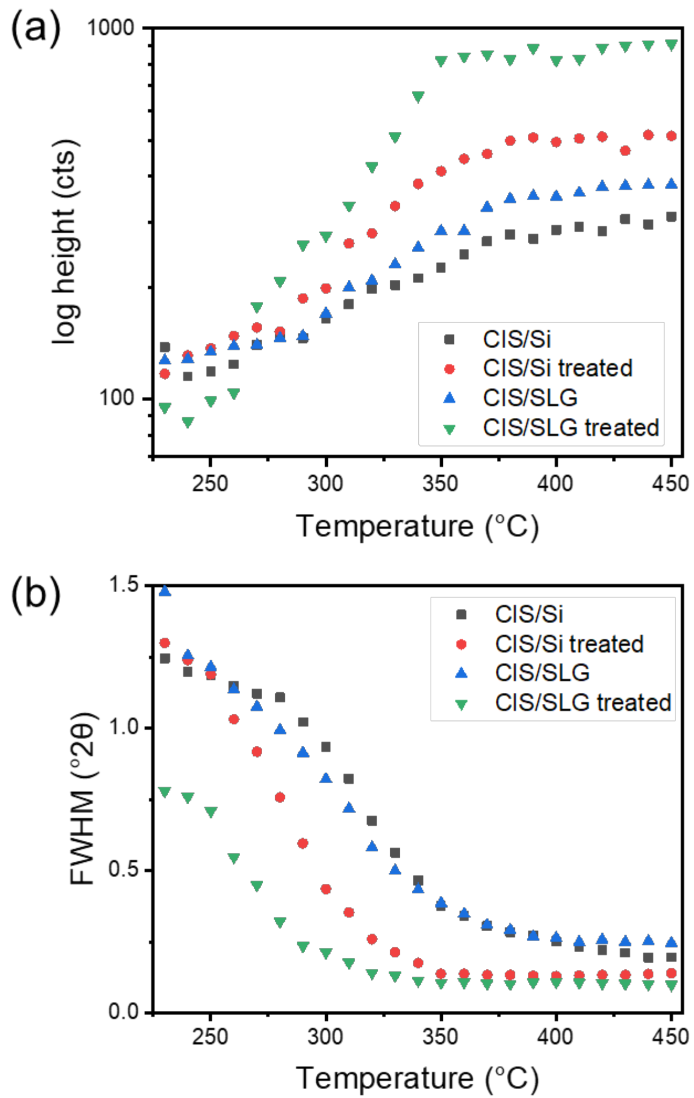

Figure 5.4 (a) Peak intensity, or height, in counts for the (112) orientation of $CuInSe_2$ versus temperature for all samples. (b) Five-point moving average of full-width at half maximum (FWHM) for the (112) orientation of $CuInSe_2$ versus temperature.

crystallinity and grain growth appear to be enhanced in the presence of $InCl_3$. As noted above, the ultimate grain size was much larger when $InCl_3$ was present (Figure 5.2), see further discussion below.

All samples begin to show crystallinity at approximately the same temperature, 270˚C, and all completed their crystallization by 380˚C. This indicates that the crystallization onset is not due to the Na_2O or $InCl_3$ but may be influenced by some other process. As the temperature at which crystallization was complete marks a point where atomic diffusion in CIS is sufficient to complete the formation of the crystalline structure to the extent detectable by XRD. The greater overall XRD peak intensities with Na_2O and $InCl_3$ indicate that the crystals were better organized by 380˚C in the presence of those species.

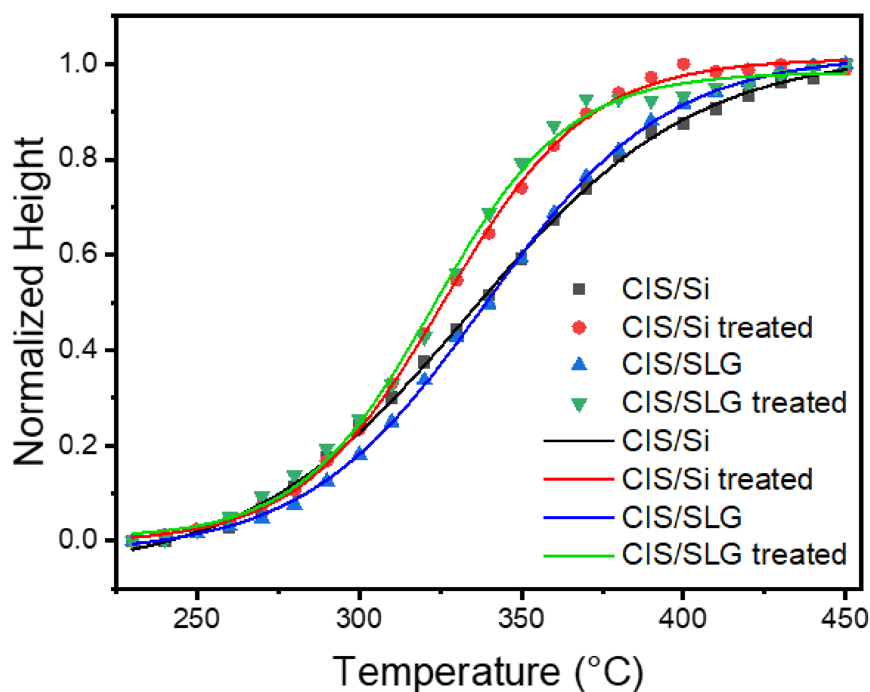

Figure 5.5 Five-point average of peak height data for the (112) orientation of $CuInSe_2$ normalized from zero to one (scatter points). Fitted sigmoid curves are overlain in solid lines.

A five-point moving average of the (112) peak height data was normalized from zero to one and plotted in Figure 5.5 per sample. Sigmoidal curve fits of this data were conducted and are overlayed in Figure 5.5 (solid lines). The first derivative was taken of the sigmoidal fits to determine the crystallization rate. This is shown in Figure 5.6.

The fitted crystallization rate curves shown in Figure 5.6 can be used to determine a relative activation energy based on the temperature of each peak maximum [16]. These maximum temperature values are compiled in Table 5.2. Some differences in the curve positions are noted. Both samples treated with $InCl_3$

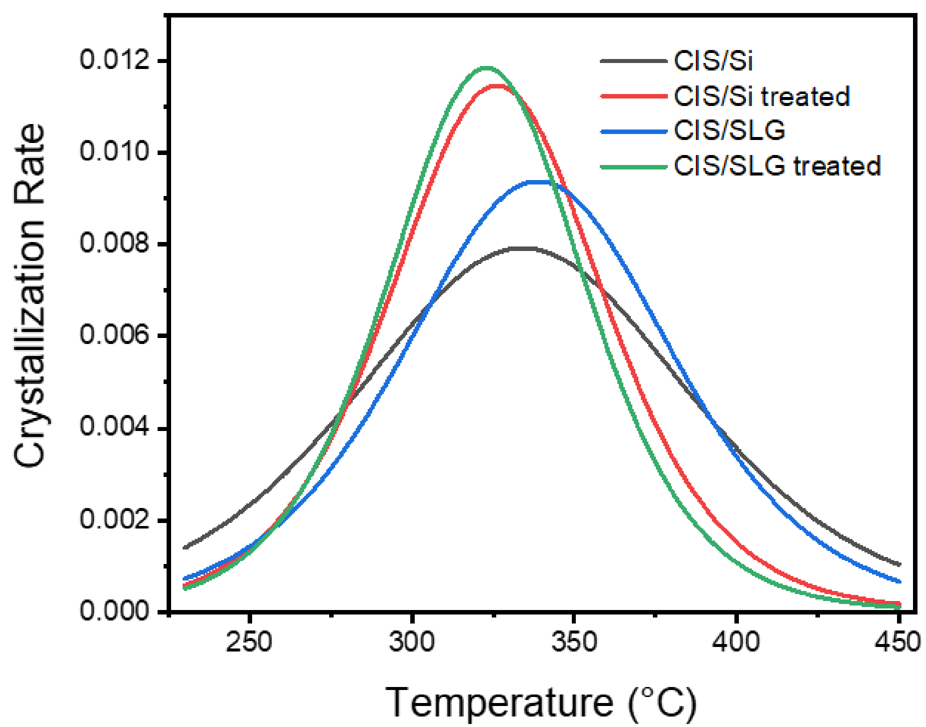

Figure 5.6 Crystallization rate versus temperature as determined by the first derivative of the fitted sigmoid curves of the five-point average of the normalized peak height data.

shifted towards lower temperatures which corresponds to a lower activation energy of crystallization. However, such differences may not be significant. Based on the quality of the curve fits and the fluctuations in the data we estimate that the peak temperatures have an error of approximately ±5°C. Therefore, nearly all values obtained are within the estimated error of each other.

Table 5.2 Maximum temperature values for each fitted sigmoid curves.

	T_{max} (°C)
CIS/Si	337 ± 5
CIS/Si+$InCl_3$	327 ± 5
CIS/SLG	340 ± 5
CIS/SLG+$InCl_3$	323 ± 5

The absence of a significant difference in activation energy for crystallization suggests that the rate-limiting step of the reaction is unchanged, which is consistent with the similar onset and termination temperatures for crystallization of each sample. However, the absolute intensity of the peaks above ~400°C increase and the FWHM decrease for both samples deposited on SLG and more so for the samples treated with $InCl_3$, indicating better crystallinity. Furthermore, the rate of crystallization as determined from the slope of the curves in Figure 5.5 increased for the samples treated with $InCl_3$. We conclude that the $InCl_3$ had a significant impact on the rate of crystallization and the final crystalline quality, although the rate limiting step in the process appears to be unchanged in the activation energy of the key step. Therefore, other factors must have increased the process rate exclusive of the activation energy.

Although the Na_2O and $InCl_3$ both enhance material transport during the crystallization, the $InCl_3$ further accelerates atomic transport resulting in the larger grain sizes (Figure 5.2). We anticipate that this is due to the Cl^- ions dissociating from the $InCl_3$ and then by etching and re-depositing atoms, resulting in larger grains growing at a faster rate and better crystalline quality.

5.5 Conclusions

Substrate and $InCl_3$ effects on amorphous $CuInSe_2$ crystallization were studied using in-situ HT-XRD and ex-situ characterization techniques. Crystallinity improved with temperature for all films between ~270°C and 380°C, with and without $InCl_3$, on silicon and glass substrates. This reveals that crystallization temperature is independent of the Na_2O and $InCl_3$. In the absence of $InCl_3$, very little grain growth was observed, although XRD showed that CIS crystals had formed. The reaction rate was accelerated in the presence of $InCl_3$ and large grains were observed for films annealed at 350°C or higher. We note that for post-deposition treatments, NaF is a preferred Na source but does not appear to produce the scale of grain growth observed here [17]. NaCl has also been considered but shows no effect on grain

size. Likewise, films with excess In do not exhibit large grain growth. Rather, In deficiency promotes grain growth [18]. Therefore, it appears that neither In nor the Cl alone are key factors in increasing grain size. It is the combination that is critical. $InCl_3$ also inhibits formation of CuSe on the film surface, presumably due to reaction of In with the CuSe to contribute to formation of CIS.

5.6 Acknowledgements

This material is based upon work supported by the U.S. Department of Energy's Office of Energy Efficiency and Renewable Energy (EERE) under Solar Energy Technologies Office (SETO) Award Number DE-EE0007551.

5.7 References

[1] B. E. McCandless, I. Youm, and R.W. Birkmire, "Optimization of vapor post-deposition processing for evaporated CdS/CdTe solar cells", Progress in Photovoltaics: Research and Applications, 7, 21-30, 1999. DOI: 10.1002/(SICI)1099-159X(199901/02)7:1<21::AID-PIP244>3.0.CO2-D.

[2] T. X. Zhou, N. Reiter, R. C. Powell, R. Sasala, and P. V. Meyers, "Vapor chloride treatment of polycrystalline CdTe/CdS films", Conference Record of the IEEE Photovoltaic Specialists Conference, 1, 103-106, 1994. DOI: 10.1109/WCPEC.1994.519818.

[3] B. E. McCandless, H. Hichri, G. Hanket, and R. W. Birkmire, "Vapor phase treatment of CdTe/CdS thin films with $CdCl_2$:O_2, Conference Record of the Twenty-Fifth IEEE Photovoltaic Specialists Conference", 781-784, 1996. DOI: 10.1109/PVSC.1996.564244.

[4] C. S. Ferekides, U. Balasubramanian, R. Mamazza, V. Viswanathan, H. Zhao, and D. L. Morel, "CdTe thin film solar cells: Device and technology issues", Solar Energy, 77, 823-830 ,2004. DOI: 10.1016/j.solener.2004.05.023.

[5] M. Nakamura, K. Yamaguchi, Y. Kimoto, Y. Yasaki, T. Kato, and H. Sugimoto, "Cd-free Cu(In,Ga)$(Se,S)_2$ thin-film solar cell with a new world record efficiency of 23.35%", IEEE Journal of Photovoltaics, 9, 1863-1867, 2019 . DOI: 10.1109/JPHOTOV.2019.2937218.

[6] E. Palmiotti, S. Soltanmohammad, A. Rockett, G. Rajan, S. Karki, B. Belfore, and S. Marsillac, "Post-Deposition Recrystallization of Chloride Treated Cu(In,Ga) Se_2 Thin-Film Solar Cells", 2018 IEEE 7th World Conference on Photovoltaic Energy Conversion (WCPEC) (A Joint Conference of 45th IEEE PVSC, 28th PVSEC & 34th EU PVSEC), 163-166, 2018. DOI: 10.1109/PVSC.2018.8547595.

[7] E. Palmiotti, S. Karki, B. Belfore, S. Soltanmohammad, G. Rajan, S. Marsillac, and A. Rockett, "Post-Deposition Recrystallization of Co-Evaporated Cu(In,Ga)Se_2 Films by Bromide Vapor Treatments", 2019 IEEE 46th Photovoltaic Specialists Conference (PVSC), 1863-1866, 2019. DOI:

10.1109/PVSC40753.2019.8980803.

[8] H.R. Moutinho, R.G. Dhere, M.J. Romero, C.S. Jiang, B. To, and M.M. Al-Jassim, "Recrystallization of PVD CdTe Thin Films Induced by $CdCl_2$ Treatment – A Comparison Between Vapor and Solution Processes", 2008 IEEE 33rd Photovoltaic Specialists Conference, 2008. GOVDOC: E 9.17:NREL/CP-520-42512.

[9] S. Gates-Rector and T. Blanton. The Powder Diffraction File: A Quality Materials Characterization Database. Powder Diffr., (2019).

[10] A. Gobeaut, L. Laffont, J.-M. Tarascon, L. Parissi, and O. Kerrec, "Influence of secondary phases during annealing on re-crystallization of $CuInSe_2$ electrodeposited films", Thin Solid Films, 517, 4436-4442, 2009. DOI: 10.1016/j.tsf.2009.01.043.

[11] L. Ouyang, M. Zhao, D. Zhuang, J. Han, Z. Gao, L. Guo, X. Li, R. Sun, and M. Cao, "Annealing treatment of $Cu(In,Ga)Se_2$ absorbers prepared by sputtering a quaternary target for 13.5% conversion efficiency device", Solar Energy, 118, 375-383, 2015. DOI: 10.1016/j.solener.2015.05.019.

[12] B. Belfore, D. Poudel, S. Karki, S. Soltanmohammad, E. Palmiotti, T. Lepetit, A. Rockett, and S. Marsillac, "Recrystallization of $Cu(In,Ga)Se_2$ Semiconductor Thin Films via $InCl_3$ Treatment", Thin Solid Films, 735, 2021.

[13] S. Ishizuka, A. Yamada, M. Islam, H. Shibata, P. Fons, T. Sakurai, K. Akimoto, and S. Niki, "Na-induced variations in the structural, optical, and electrical properties of $Cu(In,Ga)Se_2$ thin films", Journal of Applied Physics, 106, 2009. DOI: 10.1063/1.3190528.

[14] A. Rockett, K. Granath, S. Asher, M.M. Al-Jassim, F. Hanson, R. Matson, B. Basol, V. Kapur, J.S. Britt, T. Gillespie, and C. Marshall, "Na incorporation in Mo and $CuInSe_2$ from production processes", Solar Energy Materials and Solar Cells, 59, 255-264, 1999. DOI: 10.1016/S0927-0248(99)00026-4.

[15] A. Laemmle, R. Wuerz, T. Schwarz, O. Cojocaru-Mirédin, P. Choi, and M. Powalla, "Investigation of the diffusion behavior of sodium in $Cu(In,Ga)Se_2$ layers", Journal of Applied Physics, 115, 2014. DOI: 10.1063/1.4871457.

[16] P. Redhead, "Thermal Desorption of Gases", Vacuum, 12, 1962, DOI: 10.1016/0042-207X(62)90978-8.

[17] G. Rajan, B. Belfore, S. Karki, D. Poudel, H. Kahoui, N. Lanham, E. Palmiotti, S. Soltanmohammad, A. Rockett, and S. Marsillac, "Impact of Post-Deposition Recrystallization by Alkali Fluorides on $Cu(In,Ga)Se_2$ Thin-Film Materials and Solar Cells", Thin Solid Films, 690, 2019. DOI: 10.1016/j.tsf.2019.137526.

[18] L.-C. Yang, C.Y. Cheng, and J.S. Fang, "Characterization of polycrystalline $CuInSe_2$ thin films deposited by sputtering and evaporation as a function of composition", Journal of Physics and Chemistry

of Solids, 69, 2008. DOI: 10.1016/j.jpcs.2007.07.027.

5.8 Thesis Author Contributions

The thesis author was responsible for the following in this study: conceptualization, sample fabrication, data collection, formal analysis, and writing. Co-authors assisted with the formal analysis, writing, and editing.

CHAPTER 6

HOMOGENEOUS $CuGaSe_2$ GROWTH BY THE CUPRO PROCESS WITH IN-SITU AgBr TREATMENT

Paper will be submitted to *Journal of Crystal Growth*

Elizabeth Palmiotti[a*], Polyxeni Tsoulka[b], Deewakar Poudel[c], Sylvain Marsillac[c], Nicolas Barreau[b], Angus Rockett[a], Thomas Lepetit[b]

[a] Colorado School of Mines, Department of Metallurgical and Materials Engineering, Golden, CO, U.S.A.

[b] Université de Nantes, CNRS, Institut des Matériaux Jean Rouxel, IMN, F-44000, Nantes, France

[c] Old Dominion University, Virginia Institute of Photovoltaics, Norfolk, VA, U.S.A.

Abstract

Homogeneous $CuGaSe_2$ (CGS) thin film growth is limited by slow kinetics of formation. A modified growth process, named CuPRO(M), was previously developed to address this issue but requires long, high temperature anneals. Here, we demonstrate that a short AgBr treatment can replace this modified growth process. The AgBr works as a transport agent to catalyze $CuGaSe_2$ formation and atomic mobility. This treatment results in large grains with homogeneous composition through the bulk. Solar cells made with this material show better performance.

6.1 Introduction

The photovoltaics market is dominated by silicon technologies. However, further cost reductions and efficiency improvements are limited due to Auger recombination [1] and the theoretical maximum efficiency [2]. Developing a tandem structure based on a silicon bottom cell and a wide band gap (∼1.7 eV) top cell is of interest to overcome these challenges. $CuIn_{1-x}Ga_xSe_2$ (CIGS) is a top cell material candidate due to its tunable band gap. $CuGaSe_2$ (CGS) is of particular interest because it has a well-matched wide band gap of ∼1.7 eV [3]. However, CGS solar cells have limited efficiencies largely due to the formation of $Cu_\delta Se$ phases [4], [5] likely due to kinetic limitations [6]. In addition, it is found that interface recombination caused by

low band bending in the bulk limits efficiency [7]. The activation energy of reaction to form $CuGaSe_2$ is greater than that of $CuInSe_2$, suggesting that it may form at a slower rate [8], [9], [6]. Finally, typical deposition procedures used for CGS were optimized for CIGS and thus do not address this difference.

A modified co-evaporation growth procedure was developed by Tsoulka et al. to compensate for the slow kinetics of formation, resulting in larger grains with a more uniform composition and phase distribution [5]. This procedure, CuPRO(M), requires two thirty-minute "relaxation" steps. This long, high-temperature process is not economical for industrial applications. We have shown that metal halides act as transport agents in CIGS and catalyze its crystallization [10], [11], [12], [13], [14], [15]. Here, AgBr is used to catalyze the recrystallization, grain growth, and phase homogenization of CGS grown by the CuPRO procedure without the long relaxation annealing steps.

6.2 Experimental Details

6.2.1 Film and Device Fabrication

CGS films were deposited onto molybdenum-coated soda-lime glass (SLG) substrates by co-evaporation from elemental sources. All depositions were conducted in a Se overpressure and the substrate temperature was held constant at 575°C. Reference samples followed a typical 3-stage CuPRO [16] deposition procedure. During the deposition, Ga and Se were held constant while the Cu flux was adjusted such that the composition transitioned from Cu-poor (Stage 1) to Cu-rich (Stage 2) to Cu-poor (Stage 3). The other films were deposited based on two modified CuPRO procedures. The first followed the CuPRO(M) procedure [4] which includes two thirty-minute relaxation periods in Se overpressure. These relaxation steps took place (1) after the Cu-rich Stage 2 and (2) after the Cu-poor Stage 3. The second modified procedure, CuPRO+AgBr, included only the CuPRO process with an evaporation of ~20 mg of AgBr after Stage 2 over a 12-minute period in a Se overpressure. Schematic summaries of the deposition processes are provided in Appendix A.

Some films were used to complete devices with the following architecture: SLG/Mo/CGS/CdS/ZnO/ZnO:Al, where SLG refers to soda-lime glass. After CGS deposition, films were dipped in a 0.05M KCN solution for two minutes to remove any copper selenide phases from the surface [17]. Chemical bath deposition was used to grow a CdS buffer layer. Details about the optimization of the recipe followed are found in [18] and [19]. A ZnO/ZnO:Al window bi-layer was deposited by rf-sputtering. Ni-Al-Ni metallic grids were deposited using a shadow mask to form 0.5 cm^2 devices which were separated by mechanical scribing.

6.2.2 Characterization

Film morphologies were studied from SEM images taken using a JEOL JSM 7600F. Time-of-flight secondary ion mass spectroscopy (TOF-SIMS) depth profiling was conducted using an Ion TOF 5 SIMS. A 1 kV Cs^+ ion beam was used for depth profiling and the analysis beam was 30 kV Bi_3. X-ray diffraction (XRD) patterns were collected on a D8 Bruker diffractometer. Peak parameters were extracted and identified using the International Center for Diffraction Data (ICDD) Database [20].

Device parameters were determined from current density voltage (J-V) data collected under standard testing conditions (STC). The temperature of the metal plate under the sample was held at 25°C by a thermoelectric cooler. The sample was illuminated with an AM1.5 simulated solar spectrum at a power of 1000 W/m^2. External quantum efficiency (EQE) data was collected using a homemade system. Calibrations were conducted from 300 to 980 nm using Si and InGaAs monocrystals, respectively, supplied by Hamamatsu.

6.3 Results

6.3.1 Scanning Electron Microscopy

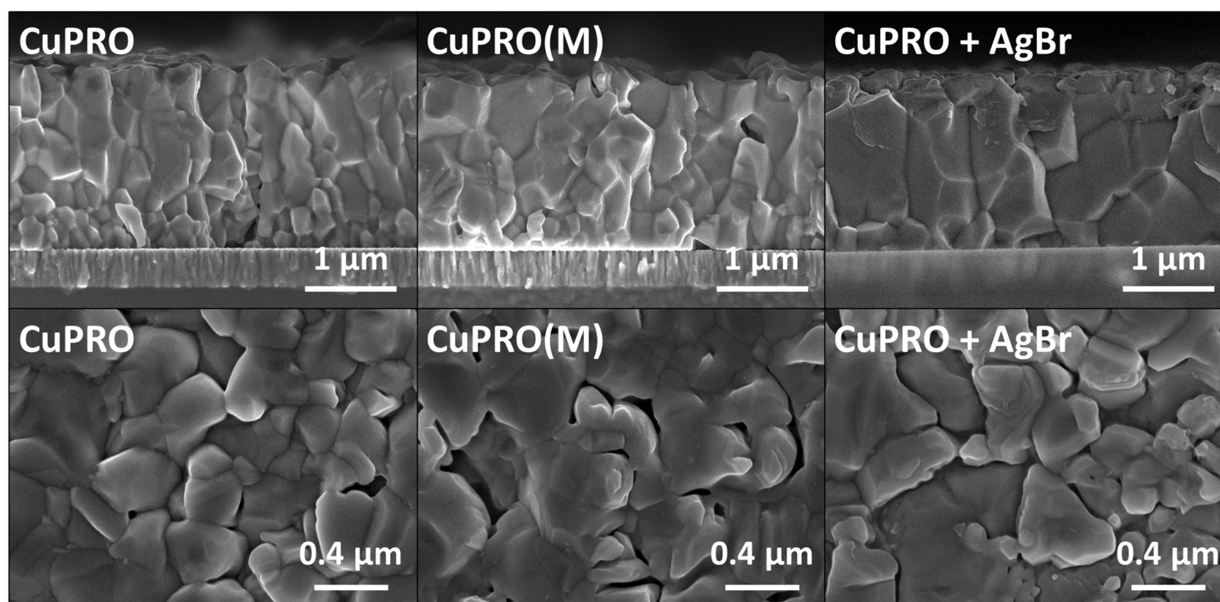

Figure 6.1 Cross-section and top-view SEM images of CGS films deposited by CuPRO, CuPRO(M), and CuPRO+AgBr processes.

Cross-section and top-view SEM images of the CGS films deposited by the CuPRO, CuPRO(M), and CuPRO+AgBr treatments are shown in Figure 6.1. The CuPRO film shows a layer of small grains (∼0.2 µm diameter) on the molybdenum, indicative of the Cu-poor first stage and larger grains (∼0.5 µm)

throughout the rest of the film. However, the surface morphology suggests smaller grains ∼0.3 µm in diameter. The film deposited by the CuPRO(M) process similarly resulted in a distribution of smaller grains toward the molybdenum and larger grains through the rest of the film. The surface morphology is consistent with grains at least ∼0.5 µm in diameter. The CGS film deposited by CuPRO with AgBr treatment resulted in very large, densely packed grains throughout the whole film. It is notable that the grains in the CuPRO+AgBr film appear to span the entire film thickness from the Mo to the surface while the larger grains in the other two samples span only the top half of the film. Despite this, the surface morphology of the CuPRO+AgBr is similar to the other samples.

6.3.2 TOF-SIMS

TOF-SIMS was used to compare the elemental distribution through the CGS films deposited by CuPRO, CuPRO(M), and CuPRO+AgBr (Figure 6.2). The intensity of each element was normalized to the total ion yield to account for minor drift in the analyzer beam intensity. The Cu, Ga, and Se signals in all samples are mostly constant through the depth of the film, showing the depositions resulted in compositional homogeneity. Trace amounts of Br were detected in the CGS film after the AgBr treatment as determined by a negative ion TOF-SIMS scan (not shown).

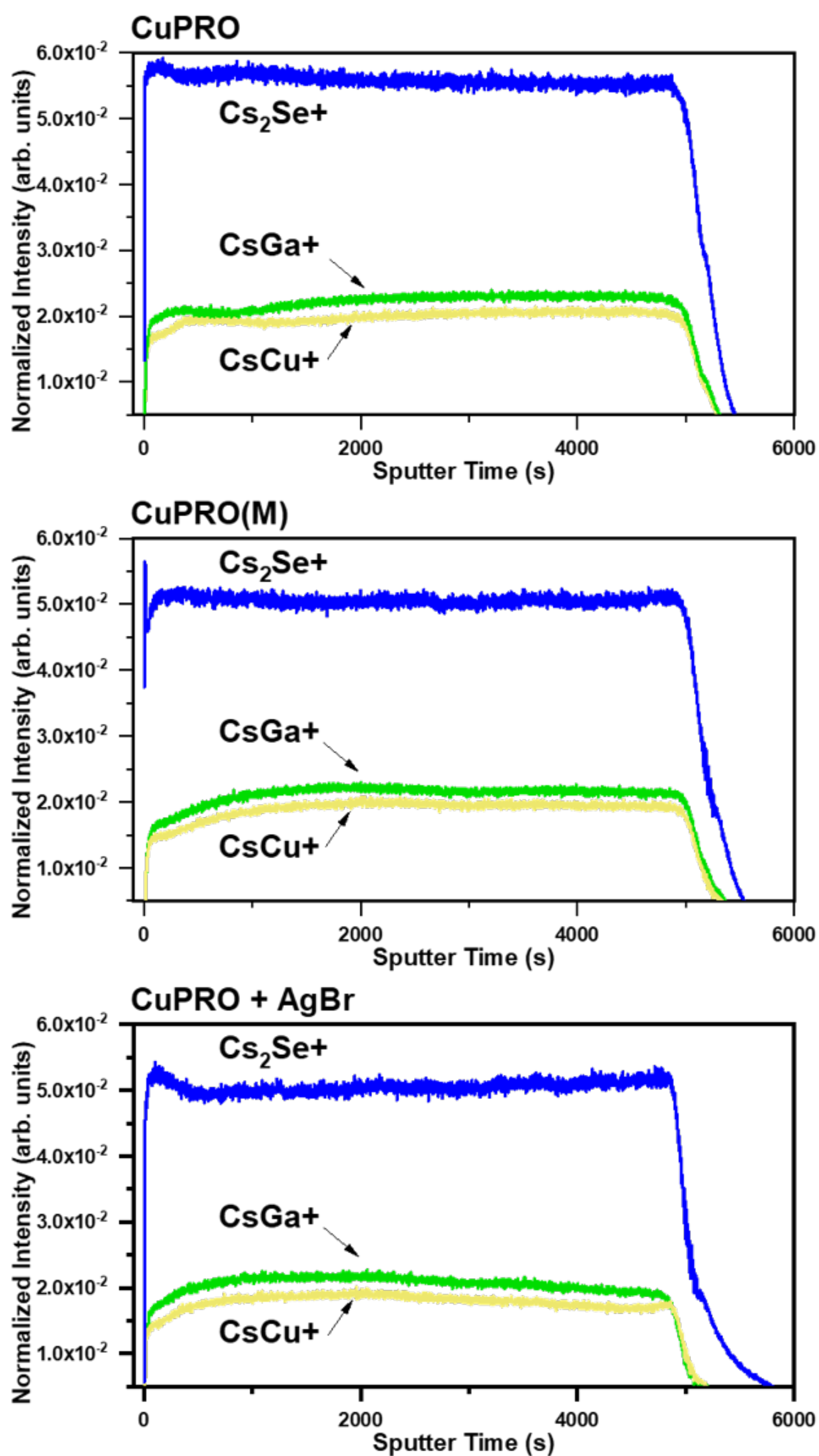

Figure 6.2 Positive ion TOF-SIMS scans collected for the CuPRO, CuPRO(M), and CuPRO+AgBr samples. The Cu signal is plotted in yellow, the Ga in green, and Se in blue.

6.3.3 X-Ray Diffraction

Figure 6.3 shows XRD patterns of the CGS films deposited by CuPRO, CuPRO(M), and CuPRO+AgBr plotted on logarithmic scales. For better interpretation select peaks were measured over smaller 2θ ranges for CuPRO (black), CuPRO(M) (red), and CuPRO+AgBr (blue). Extracted peak characteristics and intensity ratios are summarized in Table 6.1. All patterns have phases identified as chalcopyrite $CuGaSe_2$ (ICDD Ref. 03-065-2735) and Mo (ICDD Ref. 01-089-5156). The characteristic CGS peak positions and FWHM values show little to no differences among the samples. I(112)/I(220+204) varies between samples and I(220)/I(204) is higher for the CuPRO sample. Preferred orientation can change based on the growth recipe used or small variations in composition. The CuPRO sample also shows a secondary phase (2θ $\sim$27.1° and $\sim$44.9°) attributed to a $Cu_{\delta}Se$ phase where δ represents composition and ranges from 1 to 2. This is attributed to a possible Cu-Se segregation within the film which is observed for CGS [4], [5]. The two modified processes, CuPRO(M) and CuPRO+AgBr, both avoid the formation of this secondary phase.

Table 6.1 Extracted XRD pattern parameters for CuPRO, CuPRO(M), and CuPRO+AgBr. Intensity ratios were calculated for peaks representing characteristic CGS orientations.

	CuPRO		CuPRO(M)		CuPRO + AgBr	
Characteristic CGS Peak	Position (2θ)	FWHM (°)	Position (2θ)	FWHM (°)	Position (2θ)	FWHM (°)
(112)	27.4	0.07	27.73	0.071	27.74	0.067
(220)	45.67	0.11	45.67	0.11	45.68	0.11
(204)	46.18	0.11	46.18	0.108	46.18	0.106
(312)	54.24	0.14	54.24	0.13	54.25	0.12
(116)	55.13	0.14	55.13	0.14	55.14	0.13
Intensity Ratio	CuPRO		CuPRO(M)		CuPRO + AgBr	
I(112)/I(220+204)	2.29		4.59		3.12	
I(220)/I(204)	1.00		0.61		0.65	
I(312)/I(116)	2.25		2.20		2.67	

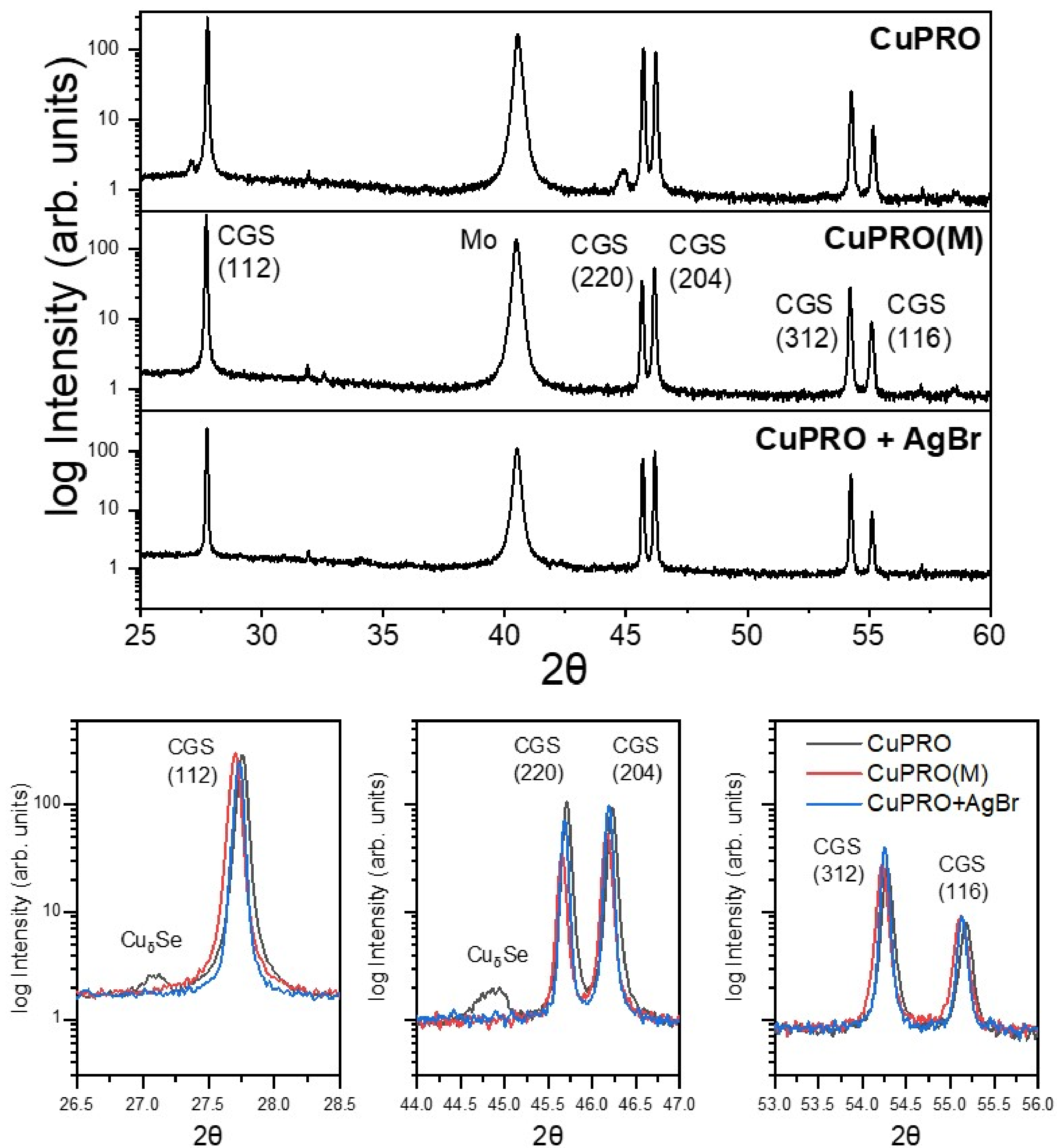

Figure 6.3 XRD spectra of the CGS films deposited by CuPRO, CuPRO(M), and CuPRO+AgBr treatment. Peaks representing characteristic (112), (220)/(204), and (312)/(116) orientations were plotted over smaller 2θ ranges for interpretation.

6.3.4 Device Characterization

Devices were fabricated using CGS deposited by CuPRO, CuPRO(M), and CuPRO+AgBr processes. Device parameters are shown in Figure 6.4 for the five highest efficiency devices made by each deposition

procedure. Fill factor (FF) and V_{oc} were measured by J-V and J_{sc} by EQE per device. Efficiency values were calculated using these values. All exhibit similar low FF values, typical of CGS devices [21], [4]. The AgBr treatment resulted in devices with notably high and consistent V_{oc} values. The J_{sc} of all samples show similar values, though there is a small gain with AgBr treatment and larger gain with CuPRO(M) compared to CuPRO. The devices prepared with CuPRO+AgBr have the highest efficiencies compared to those prepared by CuPRO and CuPRO(M) due to V_{oc} and FF.

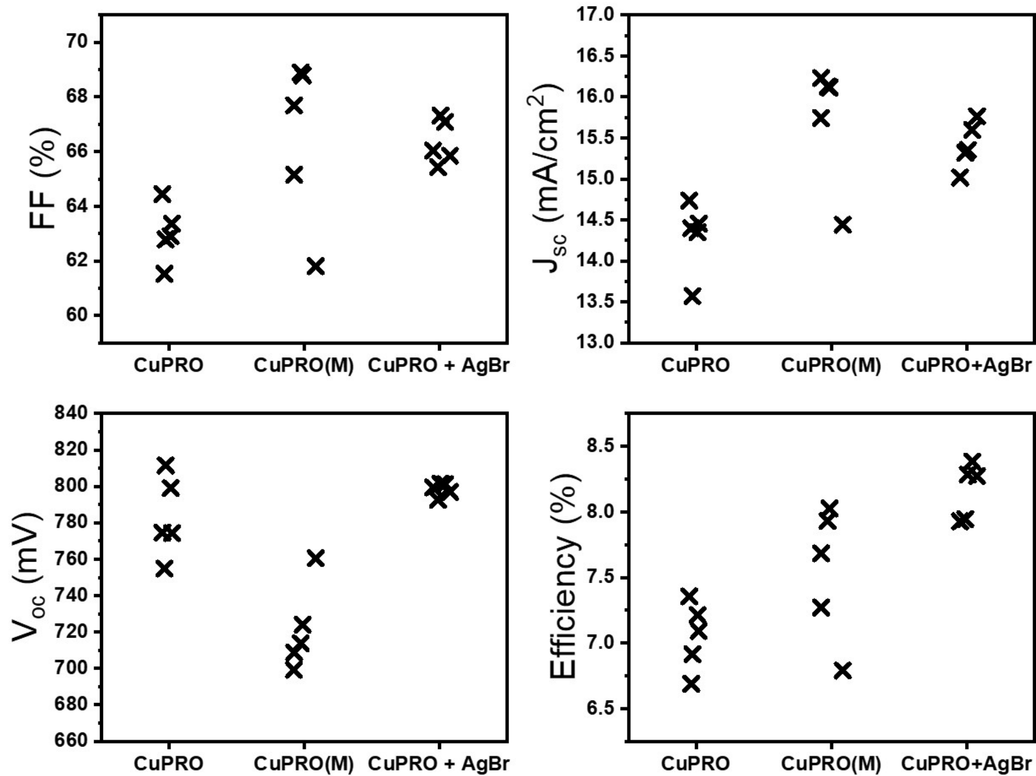

Figure 6.4 Device parameters for the five highest efficiency (%) devices per deposition procedure. The fill factor (FF) (%) and V_{oc} (mV) were extracted from current density-voltage measurements and J_{sc} (mA/cm^2) values extracted from external quantum efficiency measurements.

EQE measurements were conducted on the CuPRO, CuPRO(M), and CuPRO+AgBr samples and representative curves are shown in Figure 6.5. The absorption edge of the CuPRO(M) and CuPRO+AgBr samples extend to slightly longer wavelengths and appear to have smaller band gaps compared to the CuPRO. For CuPRO, the absorption edge has small steps likely due to small variations in composition or phase through the layer. Note that the small differences in the short wavelength region are attributed to differences in the ZnO/ZnO:Al layer, which is beyond the scope of this work.

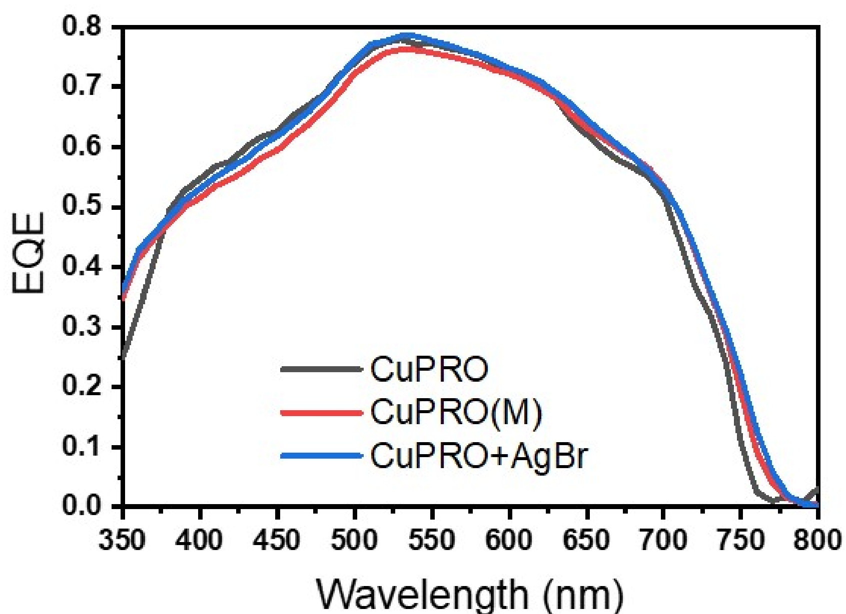

Figure 6.5 External quantum efficiency (EQE) curves for CGS devices prepared by CuPRO, CuPRO(M), and CuPRO+AgBr.

6.4 Discussion

Depositing CGS by CuPRO with a AgBr treatment produces structurally and compositionally homogeneous films comparable to those deposited by CuPRO(M). The AgBr treatment reduces total deposition time by approximately 50%, with respect to CuPRO(M), and results in larger grains through the film depth and higher device efficiencies. Note that the devices studied could be further optimized by an anti-reflective coating. Although the elemental distribution was constant through the film depth for all samples (Figure 6.2), CuPRO+AgBr and CuPRO(M) do not form a Cu-rich phase (Figure 6.3) as does CuPRO alone. We note that similar $InCl_3$ treatments catalyze amorphous $CuInSe_2$ crystallization and suppress the formation of an intermediate $Cu_\delta Se$ phase [15]. This suggests that AgBr is catalyzing the nucleation, growth, and homogenization of the chalcopyrite CGS and possibly suppressing the formation of the $Cu_\delta Se$ phase or increasing the rate of its consumption.

We conclude that AgBr works as a transport agent to enhance CGS formation and atomic mobility through the film. After evaporation, the AgBr is expected to dissociate upon adsorbing on the CGS, introducing Br to react with the CGS species. Under the current process conditions, Br would be expected to form volatile intermediate compounds. This could drive increased species transport which is necessary for recrystallization and grain growth. For example, the vapor pressure of $GaBr_3$, a likely intermediate

phase, over its own solid is very high (~$6.4x10^9$ Pa at a substrate temperature of 575°C) [22]. If the $GaBr_3$ can also condense on the grains and redeposit Ga, this would produce rapid Ga redistribution and hence the observed uniform distribution of Ga through the film. Cu mobility is also enhanced by a similar mechanism but to a lesser extent compared to Ga. The vapor pressure of the expected intermediate phase CuBr at 575°C is approximately $4.5x10^2$ Pa [23]. We note that Cu is also typically a highly mobile species in these compounds so vapor phase transport may be less important. The introduction of a small amount of Ag by this treatment may also help improve material quality. The introduction of Ag decreases the melting temperature of CIGS [24] which may aid mobility. Ag alloying has also been shown to improve V_{oc}, reduce structural disorder, and possibly decrease defect densities [25]. In the current work, such small amounts of metal halide source are used and so little Ag is detected in the deposited films by SIMS that it is unclear how critical Ag alone is to the improved device performances.

6.5 Conclusion

In this work the long "relaxation" steps during CuPRO(M) necessary for the deposition of homogeneous CGS films were replaced by a short AgBr treatment. The AgBr treatment resulted in much larger grains on the scale of the film thickness. Both CuPRO(M) and CuPRO+AgBr showed single phase CGS, demonstrating the removal of a known Cu-rich phase formed during CuPRO deposition. Devices made with CuPRO+AgBr showed V_{oc} improvements and higher efficiencies. Device optimization with an anti-reflective coating and alkali halide post-deposition treatments requires further investigation.

6.6 Funding

This material makes use of the TOF-SIMS system at the Colorado School of Mines, which was supported by the National Science Foundation under Grant No.1726898. This material is based upon work supported by the U.S. Department of Energy's Office of Energy Efficiency and Renewable Energy (EERE) under Solar Energy Technologies Office (SETO) Award Number DE-EE0007551.

6.7 References

[1] A. Richter, M. Hermle, and S. Glunz, "Reassessment of the limiting efficiency for crystalline silicon solar cells", IEEE Journal of Photovoltaics, 3, 1184-1191, 2013. DOI: 10.1109/JPHOTOV.2013.2270351.

[2] W. Shockley and H. Queisser, "Detailed Balance Limit of Efficiency of p-n Junction Solar Cells", Journal of Applied Physics, 32, 510, 1961. DOI: 10.1063/1.1736034.

[3] S. Chichibu, T. Mizutani, K. Murakami, T. Shioda, T. Kurafuji, H. Niki, P.J. Fons, and A. Yamada, "Band gap energies of bulk, thin-film, and epitaxial layers of $CuInSe_2$ and $CuGaSe_2$", Journal of Applied Physics, 83, 1998. DOI: https://doi.org/10.1063/1.366588.

[4] P. Tsoulka, A. Rivalland, L. Arzel, and N. Barreau, “Improved $CuGaSe_2$ absorber properties through a modified co-evaporation process”, Thin Solid Films, 709, 2020. DOI: 10.1016/j.tsf.2020.138224.

[5] P. Tsoulka, N. Barreau, I. Braems, L. Arzel, and S. Harel, “Detrimental copper-selenide bulk precipitation in $CuIn_{1-x}Ga_xSe_2$ thin-film solar cells. A possible reason for the limited performance at large x?”, Thin Solid Films, 712, 2020. DOI: 10.1016/j.tsf.2020.138297.

[6] W.K. Kim, E.A. Payzant, S. Kim, S.A. Speakman, O.D. Crisalle, and T.J. Anderson, “Reaction kinetics of $CuGaSe_2$ formation from a GaSe/CuSe bilayer precursor film”, Journal of Crystal Growth, 310, 2987-2994, 2008. DOI: 10.1016/j.jcrysgro.2008.01.034.

[7] J.V. Li, S. Grover, M.A. Contreras, K. Ramanathan, D. Kuciauskas, and R. Noufi, “A recombination analysis of Cu(In,Ga)Se_2 solar cells with low and high Ga compositions”, Solar Energy Materials and Solar Cells, 124, 143-149, 2014. DOI: 10.1016/j.solmat.2014.01.047.

[8] M. Purwins, A. Weber, P. Berwian, G. Müller, F. Hergert, S. Jost, and R. Hock, “Kinetics of the reactive crystallization of $CuInSe_2$ and $CuGaSe_2$ chalcopyrite films for solar cell applications”, Journal of Crystal Growth, 287, 408-413, 2006. DOI: 10.1016/j.jcrysgro.2005.11.054.

[9] S. Kim, W.K. Kim, R.M. Kaczynski, R.D. Acher, S. Yoon, T.J. Anderson, and O.D. Crisalle, “Reaction kinetics of $CuInSe_2$ thin films grown from bilayer InSe/CuSe precursors”, Journal of Vacuum Science & Technology A: Vacuum, Surfaces, and Films, 23, 310-315, 2005. DOI: 10.1116/1.1861051.

[10] E. Palmiotti, S. Soltanmohammad, A. Rockett, G. Rajan, S. Karki, B. Belfore, and S. Marsillac, “Post-Deposition Recrystallization of Chloride Treated Cu(In,Ga)Se_2 Thin-Film Solar Cells”, 2018 IEEE 7th World Conference on Photovoltaic Energy Conversion (WCPEC) (A Joint Conference of 45th IEEE PVSC, 28th PVSEC & 34th EU PVSEC), 163-166, 2018, DOI: 10.1109/PVSC.2018.8547595.

[11] E. Palmiotti, S. Karki, B. Belfore, S. Soltanmohammad, G. Rajan, S. Marsillac, and A. Rockett, “Post-Deposition Recrystallization of Co-Evaporated Cu(In,Ga)Se_2 Films by Bromide Vapor Treatments”, 2019 IEEE 46th Photovoltaic Specialists Conference (PVSC), 1863-1866, 2019, DOI: 10.1109/PVSC40753.2019.8980803.

[12] D. Poudel, B. Belfore, T. Ashrafee, E. Palmiotti, S. Karki, G. Rajan, T. Lepetit, A. Rockett, and S. Marsillac, “In Situ Recrystallization of Co-Evaporated Cu(In,Ga)Se_2 Thin Films by Copper Chloride Vapor Treatment towards Solar Cell Applications”, Energies, 14, 3938, 2021, DOI: 10.3390/en14133938.

[13] D. Poudel, B. Belfore, T. Ashrafee, S. Karki, G. Rajan, A. Rockett, and S. Marsillac, “Analysis of Post-Deposition Recrystallization Processing via Indium Bromide of Cu(In,Ga)Se_2 Thin Films”, Materials, 14, 3596, DOI: 10.3390/ma14133596.

[14] B. Belfore, D. Poudel, S. Karki, S. Soltanmohammad, E. Palmiotti, T. Lepetit, A. Rockett, and S. Marsillac, “Recrystallization of Cu(In,Ga)Se_2 Semiconductor Thin Films via $InCl_3$ Treatment”, Thin Solid

Films, 735, 2021.

[15] E. Palmiotti, B. Belfore, D. Poudel, S. Marsillac, A. Rockett, "In-Situ Study of the Crystallization of Amorphous $CuInSe_2$ Thin Films and the Effect of $InCl_3$ Treatment", Thin Solid Films, (Unpublished results).

[16] J. Kessler, C. Chityuttakan, J. Lu, J. Schöldström, and L. Stolt, "Cu(In,Ga)Se_2 Thin Films Grown with a Cu-Poor/Rich/Poor Sequence: Growth Model and Structural Considerations", Progress in Photovoltaics: Research and Applications, 11, 319-331, 2003. DOI: 10.1002/pip.495.

[17] J. Lehmann, S. Lehmann, I. Lauermann, T. Rissom, C.A. Kaufmann, M.C. Lux-Steiner, M. Bär, S. Sadewasser, "Reliable wet-chemical cleaning of natively oxidized high-efficiency Cu(In,Ga)Se_2 thin-film solar cell absorbers", J. Appl. Phys., 116, 2014. DOI: 10.1063/1.4903976.

[18] L. Choubrac, G. Brammertz, N. Barreau, L. Arzel, S. Harel, M. Meuris, and B. Vermang, "7.6% CZGSe Solar Cells Thanks to Optimized CdS Chemical Bath Deposition", Physica Status Solidi (A) Applications and Materials Science, 215, 1-9, 2018. DOI: 10.1002/pssa.201800043.

[19] T. Kodalle, Léo Choubrac, L. Arzel, R. Schlatmann, N. Barreau, and C. A. Kaufmann, "Effects of KF and RbF post deposition treatments on the growth of the CdS buffer layer on CIGS thin films – a comparative study", Solar Energy Materials and Solar Cells, 200, 2019. DOI: 10.1016/j.solmat.2019.109997.

[20] S. Gates-Rector and T. Blanton. The Powder Diffraction File: A Quality Materials Characterization Database. Powder Diffr., (2019).

[21] S. Ishizuka, A. Yamada, P. Fons, H. Shibata, and S. Niki, "Structural tuning of wide-gap chalcopyrite $CuGaSe_2$ thin films and highly efficient solar cells: differences from narrow-gap Cu(In,Ga)Se_2", Progress in Photovoltaics, 22, 2014. DOI: 10.1002/pip.

[22] B. Brunetti, V. Piacente, and P. Scardala, "A Study on the Sublimation of Gallium Tribromide", Journal of Chemical and Engineering Data, 54, 2273-2276, 2009.

[23] A. Iizuka, E. Shibata, M. Sato, N. Onodera, and T. Nakamura, "Vapor pressure measurements of CuBr and $ZnBr_2$ by the Knudsen effusion method and their vapor species identification", Thermochimica Acta, 593, 1-6, 2014. DOI: 10.1016/j.tca.2014.08.003.

[24] J.L. Shay and J.H. Wernick. Ternary Chalcopyrite Semiconductors: Growth, Electronic Properties, and Applications. Pergamon Press, 1975.

[25] P.T. Erslev, J. Lee, G.M. Hanket, W.N. Shafarman, and J.D. Cohen, "The electronic structure of $Cu(In_{1-x}Ga_x)Se_2$ alloyed with silver", Thin Solid Films, 519, 7296-7299, 2011. DOI: 10.1016/j.tsf.2011.01.368.

6.8 Appendix A

Figure 6.6 shows qualitative schematics of the deposition fluxes in the procedures followed. Cu transitions were monitored by end-point-detection using the output power of the substrate temperature controller as described in [16].

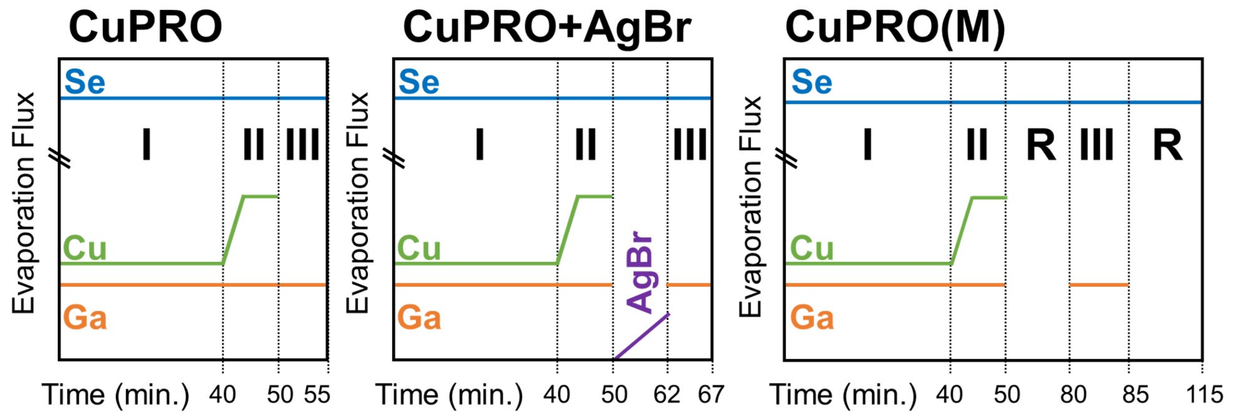

Figure 6.6 Schematics of the deposition recipes followed to deposit CGS films by CuPRO, CuPRO+AgBr, and CUPRO(M). Note that the evaporation fluxes are relative and times are approximate. The stages are respectively labeled as I, II, and III. The “relaxation” steps in CuPRO(M) are labeled as R.

6.9 Thesis Author Contributions

The thesis author was responsible for the following in this study: conceptualization, sample fabrication, data collection, formal analysis, and writing. Co-authors assisted with the conceptualization, methodology, and editing. This work was conducted by the thesis author at the Université de Nantes - Institut des Matériaux Jean Rouxel.

CHAPTER 7
CONCLUSION

7.1 Supporting Work

Additional work further supporting the results and conclusions in this thesis was conducted. Details about published complimentary work can be found in Appendices A and B.

Appendix A provides citation information and abstracts for the following ancillary publications: *Identification and analysis of partial shading breakdown sites in $CuIn_xGa_{(1-x)}Se_2$ modules*, *Post-Deposition Recrystallization of Chloride Treated Cu(In,Ga)Se_2 Thin-Film Solar Cells*, *Post-Deposition Recrystallization of Co-Evaporated Cu(In,Ga)Se_2 Films by Bromide Vapor Treatments*, and *$CuIn_{(1-x)}Ga_xSe_2$ Recrystallization by Metal Halide Treatments.*

Appendix B provides citation information and abstracts for the following relevant co-author publications: *Impact of Post-Deposition Recrystallization by Alkali Fluorides on Cu(In,Ga)Se_2 Thin-Film Materials and Solar Cells*, *In Situ Recrystallization of Co-Evaporated Cu(In,Ga)Se_2 Thin Films by Copper Chloride Vapor Treatment towards Solar Cell Applications*, and *Recrystallization of Cu(In,Ga)Se_2 Semiconductor Thin Films via $InCl_3$ Treatment.*

7.2 Discussion and Conclusions

In this thesis it has been demonstrated that metal halide vapor treatments enhance the grain size and structure of CIGS films and the kinetics of their crystallization and homogenization. Halides alone preferentially etch CIGS constituents. Alkali halide treatments result only in defect passivation but not grain growth. The use of a metal halide appears to be critical to induce both recrystallization and grain growth during short annealing treatments. In-situ metal halide treatments have been used to decrease CIGS deposition temperature and time, which are critical to reducing capital expenditures. Currently, the three-stage co-evaporation procedure takes approximately 1 hour to deposit at a substrate temperature of at least 550°C. To be cost-competitive with other photovoltaic technologies, module throughput should be reduced to 1-2 minutes [1]. It has been shown that these metal halide treatments can reduce the deposition time to $\sim$15 minutes with a maximum temperature of 400°C [2]. Further deposition time and temperature reductions are possible with optimization.

Chapter 4 provides a growth mechanism where the halide acts as a transport agent to enable atomic mobility. AgBr, CuCl, $CuCl_2$, CuBr, $InCl_3$, and $InBr_3$ have been shown to be effective metal halide sources, resulting in the recrystallization and grain size enhancement of low-temperature deposited CIGS

films. These results show that the typically high temperatures used for CIGS deposition can be drastically reduced. If films can be deposited at ~350°C then the material improved to device quality using a metal halide treatment manufacturing costs could be reduced. Moreover the rate of crystallization was shown to increase in the presence of a metal halide, more specifically $InCl_3$ (Chapter 5). This suggests that deposition time could be decreased, further reducing costs attributed to absorber layer deposition.

Further optimization of these treatments is necessary to address the resulting changes to composition. The greatest changes occur to Ga which is explained by the high vapor pressures and stability of Ga-halide compounds. Some, but notably less, changes to In content also occur. In a post-deposition treatment where a film is annealed in the presence of a metal halide source nearly all Ga is removed from the CIGS film. During an in-situ treatment where the metal halide is introduced after Stage 2 and the composition rectified during Stage 3, the expected Ga grading disappears due to increased mobility.

Combining the beneficial effects and enhanced Ga mobility, Chapter 6 demonstrates the application of a AgBr metal halide treatment to CGS. CGS is a promising wide-gap top cell candidate for Si-based tandem photovoltaics. However, CGS growth is limited by slow kinetics which causes phase separation, bimodal grain size distribution through the film thickness, and poor device performance. By interrupting growth after Stage 2 and introducing AgBr during a quick evaporation process, film quality is greatly improved. Large grains, phase homogenization, and photovoltaic properties are improved and deposition time is reduced by nearly half.

7.3 Future Applications

In-situ metal halide treatments offer a promising way to reduce the time and temperature, thus cost, of CIGS absorber layers. Metal halide dose should be optimized to the application (alloy composition, substrate size, distance from source to substrate, etc.). Treatments could be used to try and improve the quality of Single-Stage or Boeing-type deposited films, further reducing processing time.

Based on the success of improving CGS films using a metal halide treatment, the treatment could be used to attempt to improve other wide-gap CIGS alloys. Although CIGS performance is theoretically maximized at x~0.7, experimentally this value is x~0.3. The slower formation kinetics of CGS versus CIS could explain this; a metal halide treatment could provide a path towards this theoretical maximum.

7.4 References

[1] K. Horowitz, R. Fu, and M. Woodhouse, “An analysis of glass-glass CIGS manufacturing costs”, Solar Energy Materials and Solar Cells, 154, 1-10, 2016. DOI: 10.1016/j.solmat.2016.04.029.

[2] B. Belfore, D. Poudel, T. Lepetit, E. Palmiotti, T. Ashrafee, A. Rockett, N. Barreau, and S. Marsillac, "Low-temperature, high-rate deposition of $Cu(In,Ga)Se_2$ by recrystallization catalyzed by AgBr". (Unpublished results).

APPENDIX A

ADDITIONAL PUBLICATIONS

A.1 Identification and analysis of partial shading breakdown sites in $\mathbf{CuIn_xGa_{(1-x)}Se_2}$ modules

E. Palmiotti, S. Johnston, A. Gerber, H. Guthrey, A. Rockett, L. Mansfield, T. Silverman, and M. Al-Jassim, "Identification and analysis of partial shading breakdown sites in $CuIn_xGa_{(1-x)}Se_2$ modules", Solar Energy, 161, 2017. DOI: 10.1016/j.solener.2017.12.019.

Abstract: In this study, $CuIn_xGa_{(1-x)}Se_2$ (CIGS) mini-modules are stressed under reverse bias, resembling partial shading conditions, to predict and characterize where failures occur. Partial shading can cause permanent damage in the form of 'wormlike' defects on thin-film modules due to thermal runaway. This results in module-scale power losses. We have used dark lock-in thermography (DLIT) to spatially observe localized heating when reverse-bias breakdown occurs on various CIGS mini-modules. For better understanding of how and where these defects originated and propagated, we have developed techniques where the current is limited during reverse-bias stressing. This allows for DLIT-based detection and detailed studying of the region where breakdown is initiated before thermal runaway leads to permanent damage. Statistics of breakdown sites using current-limited con- ditions has allowed for reasonable identification of the as-grown defects where permanent breakdown will likely originate. Scanning electron microscope results and wormlike defect analysis show that breakdown originates in defects such as small pits, craters, or cracks in the CIGS layer, and the wormlike defects propagate near the top CIGS interface.

A.2 Post-Deposition Recrystallization of Chloride Treated $\mathbf{Cu(In,Ga)Se_2}$ Thin-Film Solar Cells

E. Palmiotti, S. Soltanmohammad, A. Rockett, G. Rajan, S. Karki, B. Belfore, and S. Marsillac, "Post-Deposition Recrystallization of Chloride Treated $Cu(In,Ga)Se_2$ Thin-Film Solar Cells", 2018 IEEE 7th World Conference on Photovoltaic Energy Conversion (WCPEC) (A Joint Conference of 45th IEEE PVSC, 28th PVSEC & 34th EU PVSEC), 163-166, 2018, DOI: 10.1109/PVSC.2018.8547595.

Abstract: Conditions promoting the recrystallization of $CuIn_xGa_{(1-x)}Se_2$ (CIGS) deposited by co-evaporation at 350°C were studied. Cu-rich and Cu-poor CIGS samples were annealed at 400°C and 550°C for 1 hour in the presence of alkali halide, In(III)Cl, Cu(II)Cl, Se(IV)Cl, and Se vapors. Increases in

grain size of greater than 10x were observed with In(III)Cl with Se, Cu(II)Cl with and without Se, and Se(IV)Cl at 550°C. Smaller magnitude grain size increases resulted at 400°C. Film composition was influenced by the vapors present with In(III)Cl enhancing the In content and Cu(II)Cl enhancing the Cu content. Based on XRD analysis, the In(III)Cl+Se treatment best preserves the CIGS structure while resulting in a large amount of grain growth.

A.3 Post-Deposition Recrystallization of Co-Evaporated Cu(In,Ga)Se_2 Films by Bromide Vapor Treatments

E. Palmiotti, S. Karki, B. Belfore, S. Soltanmohammad, G. Rajan, S. Marsillac, and A. Rockett, "Post-Deposition Recrystallization of Co-Evaporated Cu(In,Ga)Se_2 Films by Bromide Vapor Treatments", 2019 IEEE 46th Photovoltaic Specialists Conference (PVSC), 1863-1866, 2019, DOI: 10.1109/PVSC40753.2019.8980803.

Abstract: CIGS films deposited at 400°C onto molybdenum- coated soda-lime glass substrates by co-evaporation were annealed in $InBr_3$ vapors or CuBr with Se vapors. The treatments were conducted at 400°C, 450°C, or 500°C for one hour. The $InBr_3$ treatments above 400°C and CuBr with Se treatments at 500°C resulted in increased grain size, improved crystallinity, and a decrease in Cu_2Se phase. Annealed samples also exhibited large surface facets. CIGS films deposited at 350°C were also investigated in $InBr_3$ and CuBr with Se vapors at 450°C for one hour. These treatments resulted in increased grain size and less deviations from the as-deposited composition.

A.4 $CuIn_{(1-x)}Ga_xSe_2$ Recrystallization by Metal Halide Treatments

E. Palmiotti, B. Belfore, D. Poudel, S. Marsillac, and A. Rockett, "$CuIn_{(1-x)}Ga_xSe_2$ Recrystallization by Metal Halide Treatments", 2021 IEEE 48th Photovoltaic Specialists Conference (PVSC), 0669-0671, 2021. DOI: 10.1109/PVSC43889.2021.9518793.

Abstract: $CuIn_{(1-x)}Ga_xSe_2$ (CIGS) photovoltaics have limited market success due to high capital costs largely attributed to a slow, high-temperature deposition procedure. To reduce such costs we show that a high-rate, low-temperature approach including a short recrystallization step using metal halides can dramatically increase grain size in CIGS. We have demonstrated this both with high-rate evaporated films and amorphous films sputtered at room temperature. Both approaches can greatly increase throughput and reduce the costs of CIGS deposition. We review previous results for a number of metal halides and specifically focus on $InCl_3$ and AgBr as the most promising. We show that using high-temperature x-ray

diffraction that crystallization begins at 270°C and ends at 380°C and is greatly accelerated by the metal halides, resulting in much larger grains over the same temperature range.

APPENDIX B

RELEVANT CO-AUTHORED PUBLICATIONS

B.1 Impact of Post-Deposition Recrystallization by Alkali Fluorides on $Cu(In,Ga)Se_2$ Thin-Film Materials and Solar Cells

G. Rajan, B. Belfore, S. Karki, D. Poudel, H. Kahoui, N. Lanham, E. Palmiotti, S. Soltanmohammad, A. Rockett, and S. Marsillac, "Impact of Post-Deposition Recrystallization by Alkali Fluorides on $Cu(In,Ga)Se_2$ Thin-Film Materials and Solar Cells", Thin Solid Films, 690, 2019. DOI: 10.1016/j.tsf.2019.137526.

Abstract: Using thermal evaporation, $Cu(In,Ga)Se_2$ (CIGS) layers were deposited at low temperature (350°C) and high rate (10 μm/h) using a single stage process. They were then recrystallized using a variety of alkali fluorides: NaF, KF, RbF and CsF. To ensure that the substrate would not influence the study (via alkali diffusion), the samples were deposited on silicon wafers. The chemical, physical and electrical properties of the films were then characterized, demonstrating that all alkali fluorides behave as fluxing agents to enhance recrystallization and conductivity, and induce a (112) preferential orientation. Secondary ion mass spectrometry analysis showed that no modification of the elements' distribution occurs because of recrystallization. Solar cells were also fabricated and characterized, indicating that NaF can double the efficiency of solar cells compared to the as-deposited layers. This enhancement is accompanied by the disappearance of a rollover, voltage dependent current collection and shunt from the current density-voltage curves. However, even for the best recrystallization, the current is still limited to 28 mA/cm^2, indicating that only a portion (0.75 μm) of the full device (2 μm) is activated.

B.2 In Situ Recrystallization of Co-Evaporated $Cu(In,Ga)Se_2$ Thin Films by Copper Chloride Vapor Treatment towards Solar Cell Applications

D. Poudel, B. Belfore, T. Ashrafee, E. Palmiotti, S. Karki, G. Rajan, T. Lepetit, A. Rockett, and S. Marsillac, "In Situ Recrystallization of Co-Evaporated $Cu(In,Ga)Se_2$ Thin Films by Copper Chloride Vapor Treatment towards Solar Cell Applications", Energies, 14, 3938, 2021, DOI: 10.3390/en14133938.

Abstract: $Cu(In,Ga)Se_2$ (or CIGS) thin films and devices were fabricated using a modified three-stage process. Using high deposition rates and a low temperature during the process, a copper chloride vapor treatment was introduced in between the second and third stages to enhance the films properties.

X-ray diffraction and scanning electron microscopy demonstrate that drastic changes occur after this recrystallization process, yielding films with much larger grains. Secondary ion mass spectrometry shows that the depth profile of many elements is not modified (such as Cu, In and Se) while others change dramatically (such as Ga and Na). Because of the competing effects of these changes, not all parameters of the solar cells are enhanced, yielding an increase of 15% in the device efficiency at the most.

B.3 Recrystallization of Cu(In,Ga)Se_2 Semiconductor Thin Films via $InCl_3$ Treatment

B. Belfore, D. Poudel, S. Karki, S. Soltanmohammad, E. Palmiotti, T. Lepetit, A. Rockett, and S. Marsillac, "Recrystallization of Cu(In,Ga)Se_2 Semiconductor Thin Films via $InCl_3$ Treatment", Thin Solid Films, 735, 2021. DOI: 10.1016/j.tsf.2021.138897.

Abstract: One of the key challenges to promote the economic viability of Cu(In,Ga)Se2 (CIGS) solar cells is the multi-stage co-evaporation process required to make a high quality absorber layer. One phenomenon of interest is dynamic recrystallization using a fluxing agent. While these techniques have significantly improved material systems like CdTe, their impact on other nonmetallic systems are relatively unexplored. In this paper, we demonstrate that InCl3 can be used effectively to recrystallize CIGS for temperature as low as 450 ˚C, but that it also induces a modification of the surface composition. Analyses, notably via glancing incidence X-ray diffraction and secondary ion mass spectrometry, show an indium enriched surface as well as a modified alkali profile.

APPENDIX C
COPYRIGHT PERMISSIONS

In this Appendix, the relevant copyright permissions for figures and submitted articles are provided.

C.1 IRENA 2020 Figure Copyright

The report which Figure 1.1 is from states the following with respect to copyright and reproduction:

©IRENA 2020 Unless otherwise stated, material in this publication may be freely used, shared, copied, reproduced, printed and/or stored, provided that appropriate acknowledgement is given of IRENA as the source and copyright holder. Material in this publication that is attributed to third parties may be subject to separate terms of use and restrictions, and appropriate permissions from these third parties may need to be secured before any use of such material.

IRENA (2020), Global Renewables Outlook: Energy transformation 2050 (Edition: 2020), International Renewable Energy Agency, Abu Dhabi. ISBN 978-92-9260-238-3

Available for download: www.irena.org/publications For further information or to provide feedback: info@irena.org

C.2 ISE Photovoltaics Report Figure Copyright

The primary author approved the use of this figure in this thesis. Proof can be provided upon request. The following e-mail was sent to the primary author of the "Photovoltaics Report" which Figure 1.2 is sourced from:

Dear Dr. Philipps,

I am a PhD candidate working for Dr. Angus Rockett at the Colorado School of Mines. I am seeking permission to reproduce a figure from your "Photovoltaics Report" for use in my PhD thesis. I would like to use the figure showing the market share distribution of CdTe, a-Si, and CIGS thin film technologies. My thesis covers my work on metal halide induced recrystallization treatments of CIGS films to reduce deposition temperature and time to make CIGS more cost competitive. This figure would be useful in my introduction to demonstrate how currently CIGS technologies are not commercially competitive. I will, of course, fully cite the figure and data sources with its use.

Thank you,

Elizabeth Palmiotti

C.3 Chapter 4 Permission

Permission was requested and given from the co-authors of the submitted article *A Thermodynamic Evaluation of Metal Halides for the Recrystallization of Cu(In,Ga)*Se_2, which has not yet been accepted/rejected from Progress in Photovoltaics: Research and Applications. Proof of approval can be provided upon request. The following e-mail was sent:

Dear Dr. Marsillac and Dr. Rockett,

I would like to include our article, "A Thermodynamic Evaluation of Metal Halides for the Recrystallization of Cu(In,Ga)Se2" in my PhD thesis. The article was submitted to Progress in Photovoltaics: Research and Applications and has not yet been accepted or rejected for publication.

If you give permission for the article to be used in my thesis, please reply "I agree" to this e-mail.

Thank you,

Elizabeth Palmiotti

C.4 Chapter 5 Permission

Permission was requested and granted from the co-authors of the submitted article *In-Situ Study of the Recrystallization of Amorphous* $CuInSe_2$ *Thin Films*, which has not yet been accepted/rejected from Thin Solid Films. Proof of permission can be provided upon request. The following e-mail was sent:

Dear Co-Authors,

I would like to use our article, "In-Situ Study of the Recrystallization of Amorphous $CuInSe_2$ Thin Films", which was submitted to Thin Solid Films and has not yet been accepted or rejected for publication, in my PhD thesis.

If you give permission for this article to be used in my thesis, please reply "I agree" to this e-mail.

Thank you,

Elizabeth Palmiotti